DIGITAL IMAGING SYSTEM TESTING AND DESIGN USING PHYSICAL SENSOR CHARACTERISTICS

by

Brent McCleary

A Dissertation Presented to the
FACULTY OF THE GRADUATE SCHOOL
UNIVERSITY OF SOUTHERN CALIFORNIA
In Partial Fulfillment of the
Requirements for the Degree
DOCTOR OF PHILOSOPHY
(ELECTRICAL ENGINEERING)

December 2009

Dedication

To my family and in memory of my father.

Acknowledgements

I would like to express my sincere gratitude to my advisor, Prof. Antonio Ortega, for his guidance and patience during my long journey in pursuit of my Ph.D. degree at the University of Southern California. The support and encouragement I received from Prof. Ortega were invaluable. I would like to thank Prof. Richard Leahy and Prof. Aiichiro Nakano for serving as members in my dissertation committee. The time that Prof. Leahy spent in providing advice on my work is greatly appreciated. I would also like to thank Prof. Alexander A. Sawchuk and Prof. C.-C. Jay Kuo for being members of my qualifying exam committee. It was a great privilege to receive their valuable guidance on my work.

In addition, I would like to thank the many people who provided helpful advice, valuable information, and feedback on my work. In particular, I thank In Suk Chong, Quanzheng Li, and Jim Janesick. I also thank Diane Demetras for all of the help that she has provided to me over the years.

I wish to express my deepest gratitude to my lovely wife Leigh. I would be lost without her support and love. I thank my sons, Xanden and Xealen, for their optimism. I thank my late father, George, my mother, Marigold, and my sister, Maxene, for their unconditional love.

Table of Contents

List of Tables

List of Figures

Abstract

Image sensor testing and image quality enhancement methods that are geared towards commercial CMOS image sensors are developed in this thesis. The methods utilize sensor characterization data and camera system image processing information in order to improve their performance.

Photo Response Non-Uniformity

An image sensor system-level pixel-to-pixel photo-response non-uniformity (PRNU) error tolerance method is presented in Chapter 2. A novel scheme is developed to determine sensor PRNU acceptability and corresponding sensor application categorization. Excessive variation in the sensitivity of pixels is a significant cause of the screening rejection for low-cost CMOS image sensors. The proposed testing methods use the concept of acceptable degradation applied to the camera system processed and decoded images. The analysis techniques developed give an estimation of the impact of the sensor's PRNU on image quality. This provides the ability to classify the sensors for different applications based upon their PRNU distortion and error rates.

Perceptual criteria are used in the determination of acceptable sensor PRNU limits. These PRNU thresholds are a function of the camera system's image processing and sensor noise sources. We use a Monte Carlo simulation solution and a probability model-based simulation solution along with the sensor models to determine PRNU error

rates and significances for a range of sensor operating conditions. We develop correlations between conventional industry PRNU measurements and final processed and decoded image quality thresholds. The results show that the proposed PRNU testing method can reduce the rejection rate of CMOS sensors.

Cross-Talk Correction

A simple multi-channel imager restoration method utilizing *a priori* sensor characterization information is presented in Chapter 3. A novel method is developed to correct the channel dependent cross-talk of a Bayer color filter array sensor with signal-dependent additive noise. We develop separate cost functions (weakened optimization) for each color channel component-to-color channel component. Regularization is applied to each color channel component-to-color channel component, instead of the standard per color channel basis (giving us four optimal regularization parameters per color channel). This separation of color components allows us to calculate regularization parameters that take advantage of the differing magnitudes of each color channel component-to-color channel component cross-talk blurring, resulting in an improved trade-off between inverse filtering and noise smoothing.

The restoration solution has its regularization parameters determined by maximizing the developed local pixel SNR estimations. The restoration method is developed with the goal of viable implementation into the on-chip digital logic of a low-cost CMOS sensor. The separate color channel component-to-color channel component approach simplifies the problem by allowing a set of four independent color channel component optimizations per pixel. Local pixel adaptivity can also be easily applied. Performance data of the proposed correction method is presented using color images captured from low cost embedded imaging CMOS sensors.

Chapter 1

Introduction

Trends in embedded imaging show that CMOS image sensors will continue to be reduced in size and have an increased number of smaller pixels [33]. This causes the delivery of sensors that produce good quality images to be more challenging. For CMOS image sensors, more digital functionality and self-calibration will continue to be integrated into the sensors in order to cope with image quality issues. It is very important to have accurate and meaningful testing of these sensors, as the yield rate directly affects profitability. The main idea developed in this thesis is the use of the performance characteristics of CMOS image sensors and their camera systems to guide and optimize the screening of the sensors and the processing of the sensor image data. A testing method is developed in Chapter 2 to determine sensor pixel-to-pixel photo-response non-uniformity (PRNU) acceptability and corresponding sensor application categorization. In Chapter 3, a restoration method that can be implemented in on-chip logic is developed to correct the color channel dependent cross-talk of a Bayer color filter array sensor. Detailed information on CMOS image sensor characterization required to develop these image quality testing and optimization approaches is presented in the Appendices.

1.1 Pixel Response Non-Uniformity

Normally when sensor PRNU testing is performed, the temporal noise is removed by multiple frame averaging [8], [17]. When this is done, most of the photon shot noise, read noise, dark current shot noise, and other temporal noise sources are eliminated. Only fixed pattern noise due to pixel offset (mean dark current, pixel voltage offset) variation and pixel gain variation (PRNU) remain. The pixel offset variation can be removed by black frame subtraction. The standard testing method does not consider that the visibility of the PRNU can be reduced or hidden by these temporal noise sources. The effects of the image processing performed (color correction, cross-talk correction, etc.) along with the JPEG quantization on the visibility of PRNU are also not considered. In practice, a heuristic PRNU threshold is frequently determined by finding a visually acceptable level of PRNU for a worst-case operational condition [17]. Many different factors will determine the image processing that will be performed, such as designed camera application, transmission characteristics of the pixel color filters and the infra-red filter, and so forth. The approach taken in Chapter 2 is to consider the complete camera system, including its operating conditions (light levels, exposure times, ISO number, image compression requirements, etc.), when evaluating acceptable PRNU levels. Acceptable distortion values due to PRNU are determined based on camera system characterization parameters and human visual system sensitivities to errors in the DCT space.

Once these acceptable PRNU levels are determined for a particular sensor design for use in a particular application, we can screen individual sensors for PRNU using standard industry methods with the derived thresholds. The PRNU thresholds can be determined for multiple applications. Thus sensors that fail PRNU screening for one

application, may be shown to acceptable for use in another application. For example, for many consumer applications, low-light performance and color accuracy are important. For industrial applications, frame rate may be more important. Different applications may be concerned with different aspects of the pixel's performance, such as sensitivity, dynamic range, or noise [33].

Different sensors will have different signal to noise behavior, composed of differing relative amounts of read, shot, and PRNU noise. Additionally, the different applications will call for the sensor to be operated in different manners (exposure times, gain settings) with different amounts of compression (controlled by desired data rates). Further, each camera system will have different image processing, including color processing tied to specific color filter arrays, and so forth. All of these factors will result in a complex system, with many different parameters, which will affect the allowable PRNU of the sensor. For this reason, it is advantageous to have sensor and camera system models that can be run through a set of defined analyses which can determine PRNU screening values that can be applied in simple standard sensor tests. Two different sensor PRNU testing methodologies are developed in this thesis: a Monte Carlo simulation solution and a probability model-based simulation solution. Both of these methodologies allow for the screening of sensors for different applications.

1.2 Bayer Cross-Talk Problem

In Chapter 3, we derive a multi-channel, Bayer color filter array (CFA), adaptive pixel-wise, direct regularized correction solution that optimizes the local low-frequency component signal-to-noise ratio (SNR) of each corrected pixel. Our solution is geared towards application in a simple, low cost camera system (e.g., camera phone). This

application requirement results in a trade-off between accuracy of the solution and algorithm complexity (affecting the ability to implement the solution) [5]. In order to accomplish our restoration goal, we develop a method to estimate the local mean SNR value of the reconstructed local pixel signal using a deterministic reconstruction approach (developed in section 3.3). The use of local estimations avoids an indirect, iterative process. A method is derived to estimate the constrained least-squares (CLS) regularization reconstructed bias and variance errors. In order to have a simple, closed form solution, the multi-channel problem is reduced to a set of independent color channel component to color channel component equations (developed in section 3.3.1).

An important property of the separation of color channel components is that it allows the separate optimization of each color channel component. This results in each color channel component being corrected based on the ill-conditioned-ness (stability) of its blurring filters and its local signal to noise ratio. Since within color channel components are typically more stable, their correction will be closer to the ideal, non-regularized solution than that of the cross color channel components, which are less stable. This is an improvement over existing multi-channel restoration methods, which usually use a single regularization parameter per color channel (not per color channel component) [27], [44]. Separating the color channel component also allows the optimal regularization parameters for each color channel component to be solved offline and used to create look up tables for pre-calculated parameters as a function of local SNR values. Complete sets of convolution filter coefficients as a function of color channel local SNR values can also be stored. This permits a simple, real time application of the restoration.

Determining the regularization parameters using the local pixel SNR of each color channel component, instead of using MSE, noise and signal energy bounding, or other criteria, improves our correction by adhering to the sensitivity of HVS to the local SNR and low-frequency color error [7], [56], [64], [73], [75], [76]. Local pixel SNR optimization combined with the separation of color channel components, and the typically greater stability of the with-in channel cross-talk blurring filters, results in the presented restoration method giving priority to color white balance for all camera-operating conditions. However, the amount of color saturation correction (cross-channel de-blurring) will be dependent upon the sensor SNR levels. This behavior is consistent with the heuristic methods used in low-cost camera systems, but it will be more adaptive both spatially and dynamically.

1.3 Contributions of the Research

In this thesis, we present novel image sensor testing and correction methods which are applied to CMOS imagers. These algorithms use sensor characterization information, and are designed to be implementable in commercial, real-world applications. These methods utilize original approaches, as outlined in the following subsections.

1.3.1 Contributions of Pixel Response Non-Uniformity Testing Method

We have developed a novel CMOS imager PRNU testing method which uses information from the complete camera system. The key novelties in our approach are:

- Our PRNU testing method is innovative in using the concept of acceptable degradation applied to the complete camera system. The developed analysis techniques give an estimation of the impact of the sensor's PRNU on image quality. The human perceptual criteria are used in the determination of acceptable sensor PRNU limits. Our solution

determines the effect of the complex camera system, with many different parameters, on the allowable PRNU of the sensor. This is a unique application of the concept of error tolerance. Sensor operating conditions, sensor noise performance, image processing and compression are all considered in the threshold and rate determinations. Typically, fixed heuristic or empirical PRNU thresholds are used in testing.

- Our solution allows for the industry standard testing method to still be used. Using our modeled thresholds for multiple sensor applications, one test can be used to categorize each sensor for one or more of a set of possible sensor applications. This provides the ability to classify the sensors for different applications based upon their PRNU distortion and error rates. Thus, we allow for simultaneous testing for a set of sensor applications. Typically, sensor retesting would be performed for each sensor application.

1.3.2 Contributions of Bayer Cross-Talk Solution

We proposed a new solution for the Bayer CMOS imager cross-talk problem which is simple, non-iterative, non-recursive and can be implemented in the on-chip digital logic of an imaging sensor. The scheme takes into account the requirements and constraints of a typical low-cost commercial embedded camera system. Our solution is unique in combining the following method approaches and features:

- We separate each color channel into a sum of color channel components and apply a separate regularization of each color channel component. We refer to this as our separate color channel component constrained least squares (SCLS) regularization. Regularization is usually done per image or color channel [27], [44], [62]. The color channel component regularization approach is novel. We exploit the differing degrees of color channel component blurring filter ill-condition-ness and take advantage of

differing color component filter stabilities. The variation of local color channel component SNR is also exploited. We also use color channel component separation to simplify calculations, which allows for a practical camera system implementation.

- We utilize *a priori* sensor data obtained from characterization. This results in a coupling of the image sensor and the correction algorithms. Simple signal magnitude dependent noise models obtained from sensor characterization are used to define pixel SNR behavior. We obtain stationary blurring models and independent Gaussian noise models. Direction-dependent, asymmetrical and wavelength dependent cross-talk models are also used to create pixel neighborhood directional filters.

- We address the human visual system (HVS) sensitivities in the solution, including the sensitivity to local signal to noise contrast (SNR) and low spatial frequency color accuracy sensitivity [7], [56], [64], [73], [75], [76]. Our developed solution also conforms to industry standard testing methods (e.g., ISO12232-1998E). Our use of SNR constraints results in a simplification of the calculations, and makes the implementation in a low-cost camera system possible.

- We use the local pixel SNR to calculate the regularization parameter. We have not seen this approach proposed among the published correction methods. Other solution metrics do not match HVS's sensitivity to local SNR and low-frequency color error [3], [26], [48]. Our solution is adaptive to global operating conditions and local image SNR conditions. Spatially adaptive corrections are used in our solution, which are coupled with the color component separation. The correction method results in a pixel scalar solution form. Additionally, using the local mean estimate for local SNR values improves the accuracy of our estimate through noise smoothing. The local mean value also matches the HVS's color error and SNR sensitivities.

Chapter 2

Photo-Response Non-Uniformity Error Testing Methodology for CMOS Imager Systems

2.1 Introduction

In this chapter, we develop methods to determine acceptable pixel response non-uniformity (PRNU) levels which take into account the complete camera system. We evaluate the effect of image sensor PRNU defects at the output of the camera system. Camera system characterization parameters and human visual system sensitivities to errors are used to find acceptable PRNU distortion values. These calculations are done off-line for a particular sensor and camera design, allowing the standard industry PRNU testing to still be used. Our general approach of correlating conventional testing method PRNU measurements to a set of application specific error rates is shown in Figure 2.1. Conventional PRNU testing is used to measure PRNU error metrics for a set of sensors. As shown in the figure, these measured PRNU errors are then used to determine the error rates for each sensor for a set of different applications.

CMOS PRNU defects are discussed in Section 2.2, including typical screening methods and values of PRNU. Image sensor models are developed in Section 2.3. In Section 2.4, a model of the camera system is developed. The PRNU screening thresholds, involving both the human visual system and the system noise, are analyzed in Section 2.5. The camera system level PRNU distortion metric and error rate are determined in Section 2.6. The PRNU distortion metric is developed for the camera system. A Monte Carlo simulation solution and a probability model-based simulation solution are developed to determine the PRNU error rate. The PRNU distortion testing methodology is discussed. Finally, performance data and conclusions are presented in Section 2.7.

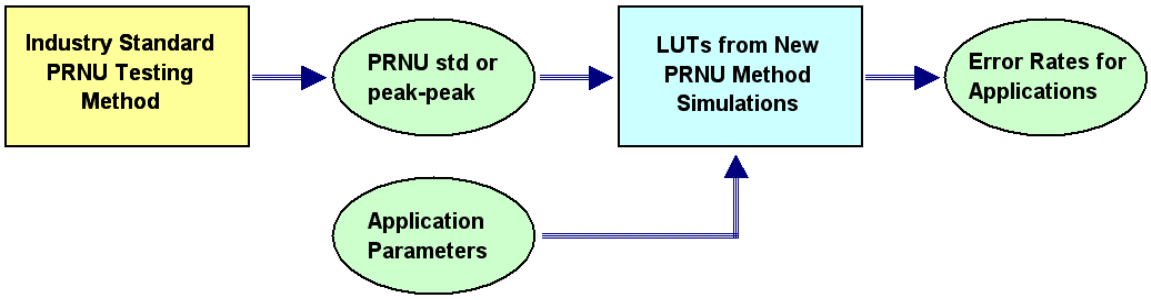

Figure 2.1: PRNU values correlated to failure rates for particular applications.

2.2 Background on CMOS PRNU Defects

2.2.1 Image Sensor Pixel Defects

We are interested in sensor defects due to excessive PRNU, a particular type of photosensor pixel defect. The different types of photosensor pixel defects are classified in Table 2.1. The pixels of a CMOS photosensor cannot be fabricated to have identical properties, such as light sensitivity. One type of pixel defect is caused by pixel-to-pixel gain mismatch. This is known as photo response non-uniformity (PRNU) [30], which will be directly proportional to the input signal strength. Thus, PRNU is signal dependent and multiplicative in nature [38]. In the literature, the effects of PRNU are sometimes

considered to be one component of fixed pattern noise (FPN) [9]. However, in this thesis, we use the more common definition which considers FPN to consist of signal-independent time-invariant noise, while PRNU is considered as a signal-dependent time-invariant noise [11], [20].

Table 2.1: Pixel defect types.

Pixel Defect Type	**Cause**
Hot Pixel	Fabrication imperfection: Pixel stuck high
Cold Pixel	Fabrication imperfection: Dead pixel, pixel stuck low
PRNU	Fabrication imperfections, Poor pixel design: Photodiode size variation Photodiode capacitance variation Source follower transistor gain variation Coating variation
High Dark Current	Fabrication imperfection: Pixel dark current variation

2.2.1.1 Causes of PRNU

The photodiode area of pixels in CCD and CMOS sensors can vary, resulting in variable gain from pixel-to-pixel. The main causes of variable pixel gain are photodiode capacitance variation and deviations in the surface area of the photodiodes [42]. The pixel conversion gain is proportional to the inverse of the photodiode capacitance (pixel gain $\propto$ q/C). Photodiode capacitance deviations are due to variations in the properties of the substrate and diode material (manufacturing doping issues). Variations in

photodiode surface area lead to differences in the number of photons being captured by a pixel. Another cause of pixel gain differences is the deviation in the thickness of color filter array (CFA) coatings, which result in different pixel photon transmission values. Pixel gain variations of 1 to 5 percent (rms) are common [39]. For APS CMOS pixels, the source-follower transistors can have variations in both gain and offset. Variations in pixel gain are complicated and expensive to correct in a camera system. For low cost camera systems, pixel gain variation is usually not corrected. The PRNU defective pixels are usually randomly distributed across the sensor array. These defects are depicted in the pixel schematic shown in Figure 2.2.

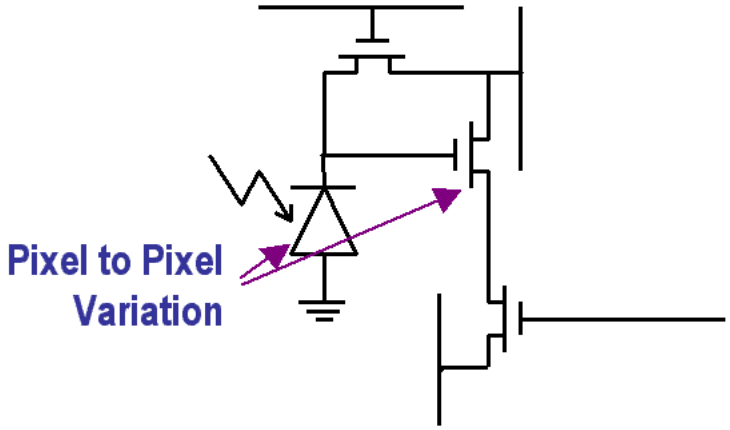

Figure 2.2: Pixel to pixel variations of photodiode and source follower transistor.

One of the major disadvantages of CMOS sensors compared to CCD sensors is the lower yield of the former due to excessive PRNU [32]. CMOS sensors usually have moderate or low pixel response uniformity [20]. However, CMOS sensors offer many advantages over CCD sensors. CMOS sensors can be manufactured at a lower cost, can integrate digital logic on the chip (e.g., ADC, JPEG logic, 'camera-on-a-chip'), consume less power, and be more compact in area (through integration of components on chip) [51].

2.2.1.2 Hot and Cold Pixel Defects

Due to fabrication errors, as the number of pixels in a photosensor increases, the likelihood of the sensor having stuck hot and cold pixels defective pixels is high. These defects occur at pixels whose output values are either stuck high (Vdd) or low (Gnd). Pixels with very high levels of PRNU can be interpreted as hot or cold pixels. Hot and cold pixel defects can be corrected during camera operation using simple spatial filtering algorithms [6], [81]. The shot noise time variation of dark current appears as temporal noise. Pixels with extremely high dark current (refer to Appendix A) are often treated as hot pixel defects.

2.2.2 Reasons for Studying PRNU Defect Testing

We will consider only PRNU defects in this analysis. The reasons for this decision are:

1) Hot and cold pixels are usually identified during wafer or device testing and are marked for correction (pixel value replacement) using neighboring pixel values. In contrast, PRNU defective pixels are usually not corrected by the imaging system, unless the PRNU values are so high as to appear as a hot or cold pixel.

2) Variation in the pixel response is unavoidable. Pixels with PRNU values which exceed standard testing thresholds, and are thus rejected, are often more likely to occur than hot or cold pixels. As discussed, excessive PRNU is a major cause of yield loss for CMOS sensors [32].

3) Image sensors that have large numbers of hot or cold pixels (especially clusters of these pixels) are usually regarded as unusable, and cannot be salvaged.

For these reasons, we wish to study the PRNU defect in order to improve photosensor yield through increasing the acceptable defect rate and allowable threshold. We will also

be able to classify sensors for particular applications based on the developed PRNU screening method. PRNU is a problem with a continuous range of characteristics, i.e., differing degrees of response non-uniformity. Our goal is to increase the fault tolerance for this type of pixel defect by considering the complete image processing chain, full sensor noise model, and sensor application operating parameters.

2.2.3 PRNU Characterization

Sensor characterization data is used to create a typical probability density function (pdf) for a CMOS sensor's pixel gain. In Figure 2.3, we show the local area pixel gain variation (pdf) for a CMOS sensor obtained from a typical sensor lot [17], [18]. The data was generated using a large set of pixel gain measurements. The measurements were taken over local pixel areas (in this case 8x8 pixel areas). The pixel gain plot has been normalized using the mean pixel gain (μ_{gain}) to give a mean gain of unity. The results shown are the mean distribution values of the collected local pixel areas. The parameter X shown in the plot on the X-axis is the standard deviation of the normalized pixel gain distribution ($\sigma_{Pixel\_Gain}=\sigma_{gain}/\mu_{gain}=PRNU_{rms}$). For a particular sensor design, the standard deviation of the pixel gain distribution will vary from sensor to sensor. This change in gain distribution is due to pixel design and manufacturing process (or wafer lot to lot variation), as discussed previously. For a particular sensor design, the shape of the distribution has been found to stay the same, with only the variance or gain variation parameter changing from chip to chip [17]. Thus, one can obtain through sensor characterization the basic shape and values of the PRNU distribution. Then the distribution can be scaled to represent different magnitudes of PRNU. For what might be considered good quality low-cost consumer sensors, the value of the standard deviation of the pixel gain distribution has been found to be around 1%. This is the value

of σ_{gain}/μ_{gain} ($PRNU_{rms}$) for the sensor family characterized in Figure 2.3 [18]. This $PRNU_{rms}$ value is a fairly typical value for CMOS sensors [40]. The upper range of the value of the gain variation parameter for some of the sensors within this design (and other design families) may extend to 4.0 or more ($\sigma_{gain}/\mu_{gain} > 4$).

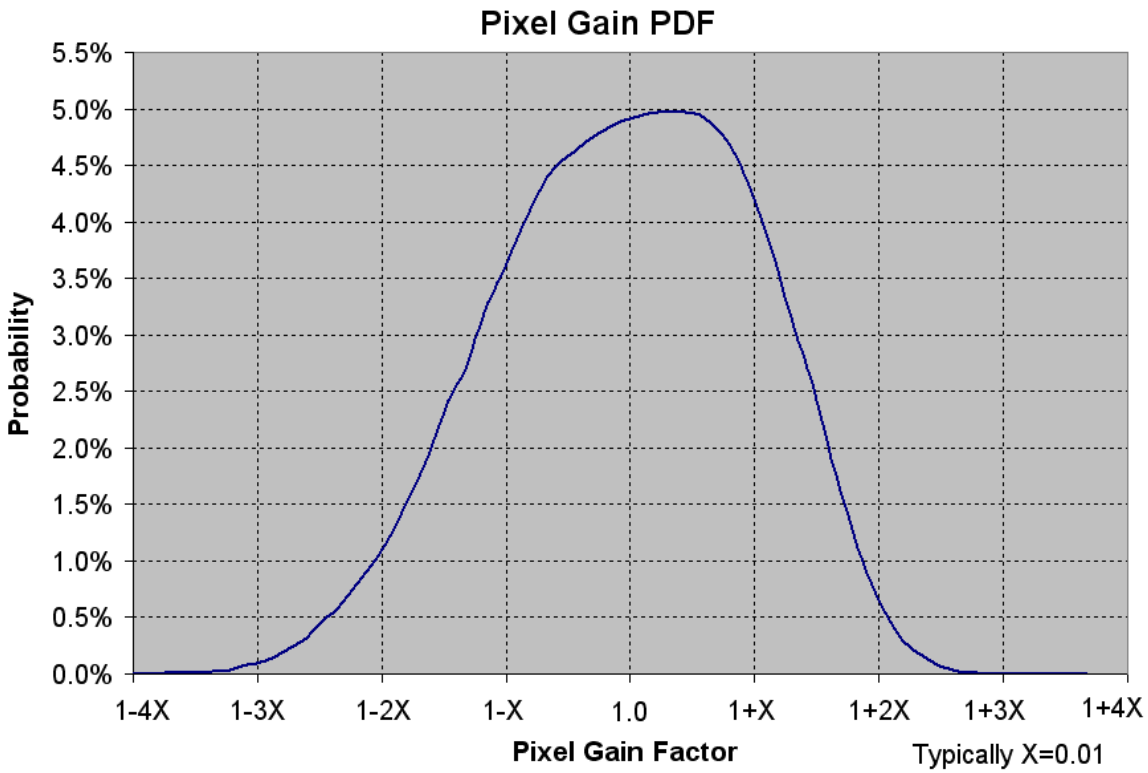

Figure 2.3: Pixel to pixel gain pdf, normalized by mean value. Characterization data from Conexant 20490 DVGA sensor. The X parameter is the standard deviation of the normalized pixel gain distribution ($\sigma_{Pixel\_Gain}=\sigma_{gain}/\mu_{gain}$), which varies from sensor to sensor.

2.2.4 Industry Standard PRNU Screening

The industry standard PRNU screening method is typically applied to monochrome sensors still on the wafer (prior to dicing) and before the color filter array has been deposited [17]. The PRNU screening is sometimes done after device packaging, with each color tested separately. PRNU can be segmented into local PRNU and global

PRNU [10]. We will concentrate on local PRNU, since it causes the greatest failure rates [9], [17]. Also, local measurement of PRNU matches well with the HVS's sensitivity to defects correlated within a small spatial area [7], [19], [73]. The HVS is less sensitive to global variation of pixel gain (brightness). The standard screening method consists of dividing the sensor's image area into non-overlapping segments, often of size 8x8 or 10x10 pixels, under a normal exposure time condition [8], [17], [52]. Typically, the response level of the pixels is set to be from 50% to 75% of full range [11] by applying uniform illumination. PRNU is linear with signal, so we wish to create large values to measure. PRNU is usually quantified in terms of the peak-to-peak pixel value divided by the mean value (μ_{gain}) for each block ($PRNU_{P-P}$) [17], [18]. Another popular metric is an rms pixel value (σ_{gain}) divided by the mean value (μ_{gain}) for each block ($PRNU_{rms}$). The block with the largest value is often taken as the PRNU value for the chip, instead of using a mean chip value. We will use the peak-to-peak method ($PRNU_{P-P}$), as it seems to be more commonly used. The peak-to-peak PRNU test is also considered better, as it finds worst case pixels that will stand-out to the observer, whereas the PRNU rms test can smooth-out one or more pixels within a block that are outliers. The peak-to-peak PRNU test is also generally faster to calculate on a wafer or chip tester.

For both the peak-to-peak and rms PRNU measurement methods, temporal noise is removed to leave only fixed pattern noise (FPN) [17]. This is done through multiple frame averaging, where 16 or more frames may be used in the mean frame calculation. When the FPN dark level offset is removed, we are left with essentially the PRNU. Testing of the pixels can be done in the analog domain, by having the voltage values of the pixels output. Often this is done by utilizing a test mode on the chip to by-pass the on-chip ADC and output voltage levels to a pin, usually when the chips are still on the

wafer [17]. For each segment (e.g., 8x8 or 10x10 area of the sensor), the average analog output voltage (Vout) is found for the mean frame. The maximum and minimum pixel voltage values of each segment's mean frame are also calculated, given by Vmax and Vmin, respectively. The peak-to-peak PRNU is then defined as:

$$PRNU_{P\text{-}P} = (Vmax - Vmin) / Vout \quad (2.1)$$

We can also perform this operation in the digital domain using digitized pixel values from the on-chip ADC. This is often done on the chip level, after the wafer has been diced. The sensor can be in the camera system, or simply in its package. When performed in the digital domain, the methodology will be the same. The only difference is that the variables Vmax, Vmin, and Vout will be digital numbers read directly from the sensor output, instead of voltage levels. During this testing, the pixels previously identified as being hot or cold pixels should not be used in the calculations. The assumption made is that these pixels will be corrected, usually using values taken from their neighbors. Sensors that have too many hot or cold pixels will have been rejected prior to the PRNU screening test.

The measured PRNU value is compared with a threshold value. The PRNU threshold value used will often be determined for a particular type of camera application. Consumer applications have PRNU peak-to-peak thresholds that vary from 10% for mid to low-end applications [16] to 5% for more stringent applications. The PRNU block error rate will be equal to the number of blocks that fail the PRNU test divided by the total number of pixel blocks on the sensor array. Using data from many sensors, it represents the probability that a sensor will have a block that fails the PRNU test. Some

applications may call for zero defective PRNU blocks, while others allow for one or more blocks failing.

2.2.5 PRNU Screening Metric Behavior

In Figure 2.4, we show expected PRNU metric values as a function of the standard deviation of the normalized pixel gain distribution (σ_{gain}/μ_{gain}=$PRNU_{rms}$) for the sensor with the pixel gain distribution shown in Figure 2.3.

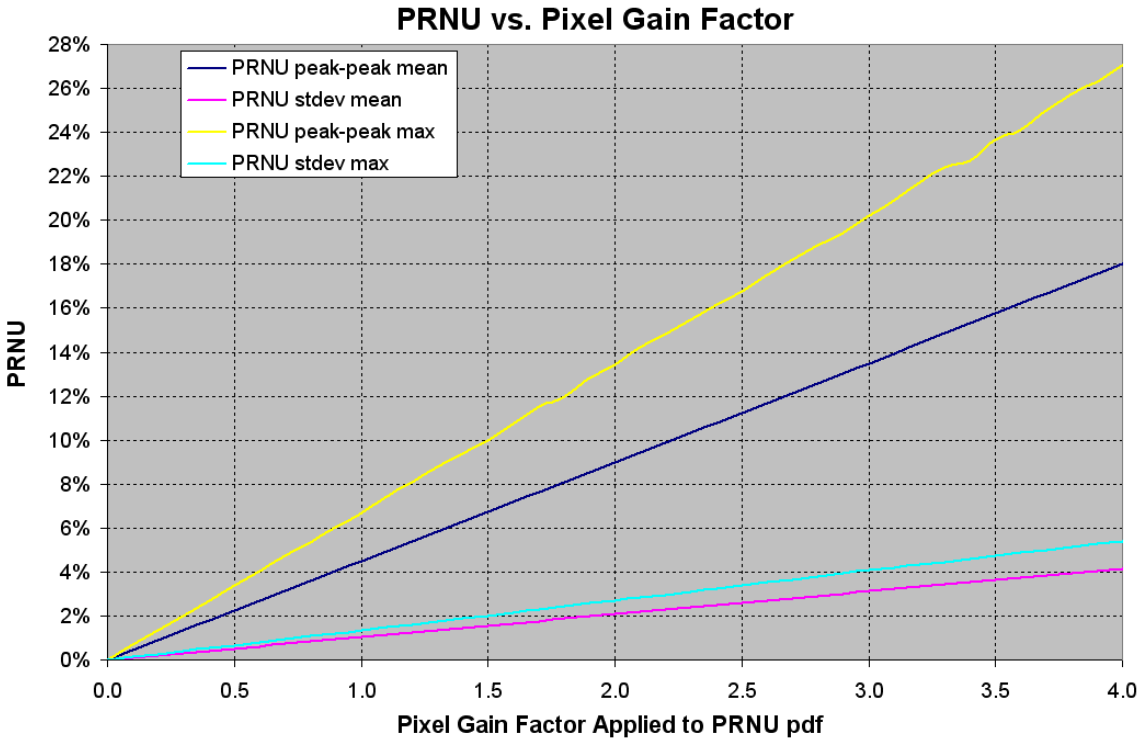

Figure 2.4: Expected PRNU metric values as a function of $PRNU_{rms}$, the standard deviation of the normalized pixel gain distribution (σ_{gain}/μ_{gain}), for Conexant DVGA resolution sensor, 4μm x 4μm pixel, with 5084 8x8 blocks. 'max' is maximum value from all of the 5048 blocks. The mean block $PRNU_{P-P}$ is appox. 4.5% when the mean block $PRNU_{rms}$ is 1%. The expected maximum PRNU values are 6.7% for $PRNU_{P-P}$ and 1.4% $PRNU_{rms}$ when $PRNU_{rms}$ is 1%. For sensors with $PRNU_{rms}$=1.5%, we expect the mean $PRNU_{P-P}$ to be 6.8%. For a DVGA resolution sensor, this corresponds to a maximum $PRNU_{P-P}$ value of 10% (and max $PRNU_{rms}$ of 2%), which is a commonly used value for the testing PRNU threshold.

The data was generated using measured pixel gain pdfs from a set of sensors. The pixel gain pdfs were scaled in order to get a realistic range of sensor PRNU performance. This scaling was applied to the standard deviation value of the pixel gain pdf. The sensor pixel data was then used to calculate the different PRNU metric values. The plot shows the anticipated linear relationship between different PRNU metrics and the standard deviation of the normalized pixel gain distribution (σ_{gain}/μ_{gain}). The expected maximum PRNU values for a sensor will be a function of the number of pixel blocks that make up the array. As the size of the sensor array increases, the probability of at least one pixel block failing the PRNU test increases. For a sensor with this pixel gain distribution and many 8x8 blocks, there can be a fairly high probability of the sensor having at least one defective PRNU block. Many commercial imager designs have less than a 1% sensor rejection rate due to PRNU [15]. However, yield losses of up to 4.5% have been seen in CMOS image sensor manufacturing [17].

Finally, we discuss the advantage of using a peak-to-peak metric for measuring PRNU instead of a rms metric. In Figure 2.5 we show two different sensor block PRNU responses. The distributions of the pixel responses are shown in the histograms of Figure 2.6. One of the 8x8 pixel blocks has a Gaussian pixel gain distribution, while the other one has uniform pixel gain with two impulse-like pixel gain outliers. The measured mean, standard deviation, and $PRNU_{rms}$ of each block are all the same. However, the $PRNU_{P\text{-}P}$ value of the image on the right is much greater. This is due to the image on the right having a zero PRNU value for all pixels except for two pixels that are extreme outliers. Since the image on the left has a Gaussian distribution of PRNU, its greatest PRNU outliers are not as extreme as the image on the right. Due to the HVS's sensitivity to brightness contrast [7], the PRNU of the image on the right is more visible.

If we were to use the $PRNU_{rms}$ metric, we would not have been able to distinguish between these two relatively low and high PRNU visibility cases (left and right images, respectively). Thus, we can see that the $PRNU_{P-P}$ method of calculating a PRNU metric is more in-line with the way the HVS functions. Our developed PRNU screening metric must be sensitive to peak-to-peak differences within blocks As we shall see in Section 2.5 when we develop our distortion metric, we will use a 'Peak Contrast' model of Minkowski pooling, as opposed to linear summation. This approach adheres to the conventional $PRNU_{P-P}$ testing method of looking at pixel PRNU outliers.

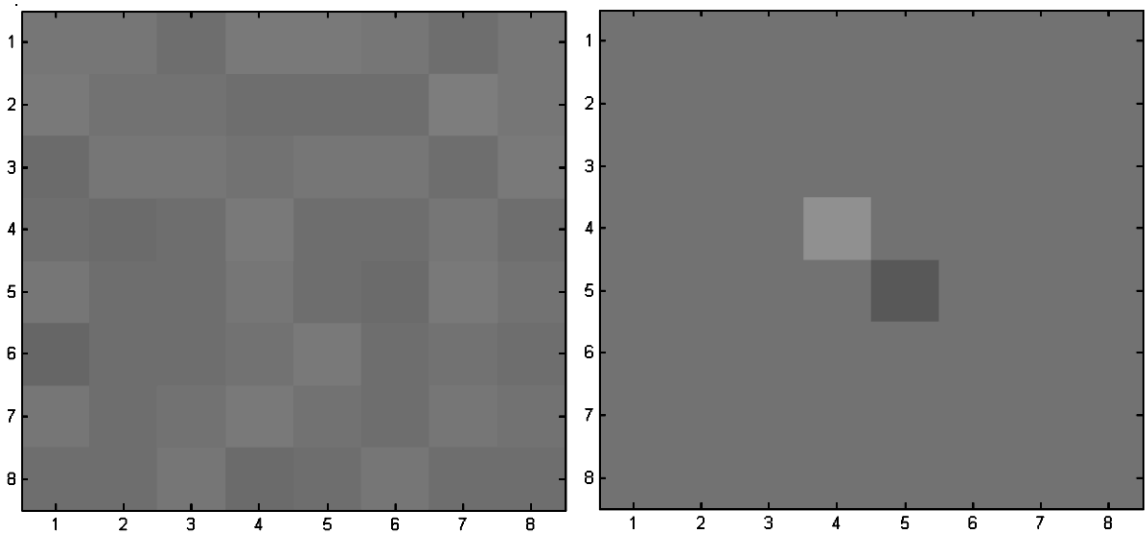

Figure 2.5: PRNU peak to peak and rms values for two different pixel PRNU distributions. The left block has a Gaussian PRNU distribution ($PRNU_{P-P}$=4%, $PRNU_{rms}$=0.87%). The right block has impulse noise for two outliers, with the remainder of the pixels having no PRNU ($PRNU_{P-P}$=10%, $PRNU_{rms}$=0.87%). The contrast has been exaggerated to enhance PRNU visibility.

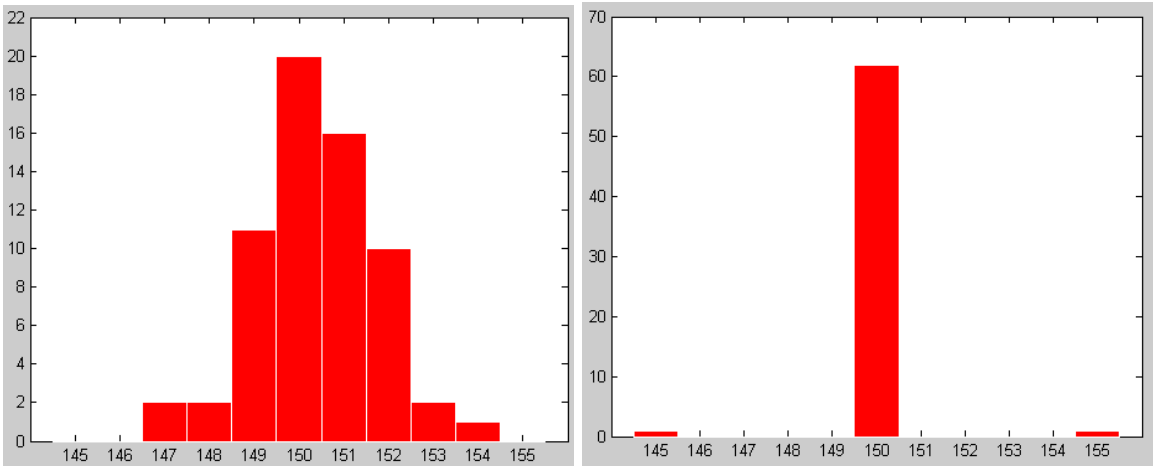

Figure 2.6: Distributions for the two 8x8 blocks shown in Figure 2.5 (left block has a Gaussian-like PRNU distribution, right block has impulse).

2.2.6 Typical Sensor Values of PRNU

We have seen that the performance of CMOS sensors is traditionally often limited by PRNU [9]. PRNU measurement values are reported in Table 2.2 for numerous sensors.

Table 2.2: Typical PRNU measurements for CMOS sensors.

Sensor Ref	**PRNU**	**Sensor Information**
[1]	2% rms	High performance VGA resolution sensor
[21]	5% rms	Commercial CMOS sensor
[51]	1.9% rms	APS CMOS sensor, 0.35 μm technology
[51]	6.5% rms	APS CMOS sensor, 0.18 μm technology
[69]	1% peak-to-peak	Very large pixel size of 11.6 μm by 11.6 μm and low resolution. Pixel is impractical for mobile imaging.

In sensor documentations, PRNU rms values for CMOS sensors in the range of 1 to 5% have been measured [39]. In making the rms measurements, the pixel mean response is removed (unbiased estimator), giving the standard deviation, which is normalized

using the mean response (μ/σ). PRNU usually increases as the pixel size is decreased. The particular CMOS technology used also affects PRNU. In cell phone applications, pixel sizes are usually less than 3 μm by 3 μm [33].

2.3 Pixel Noise and Defect Characterization and Modeling

2.3.1 Image Sensor Noise Model

In this section, we will develop noise models for our CMOS image sensors. We will define a simplified camera system noise model that can be used in creating acceptable threshold values for image distortion (see Section 2.5). As we will discuss later, the presence of other noise sources can mask the effects of PRNU noise. Detailed information on CMOS image sensor noise is presented in Appendix A.

CMOS image sensors experience noise from numerous noise sources. The resulting noise has both time-invariant (fixed-pattern) and time-variant (temporal) behavior. The use of the term fixed-pattern noise refers to any spatial pattern that does not change significantly from frame to frame. In contrast, temporal noise changes from image frame to frame. A noise transfer diagram is shown in Figure 2.7 for a typical CMOS imager [35].

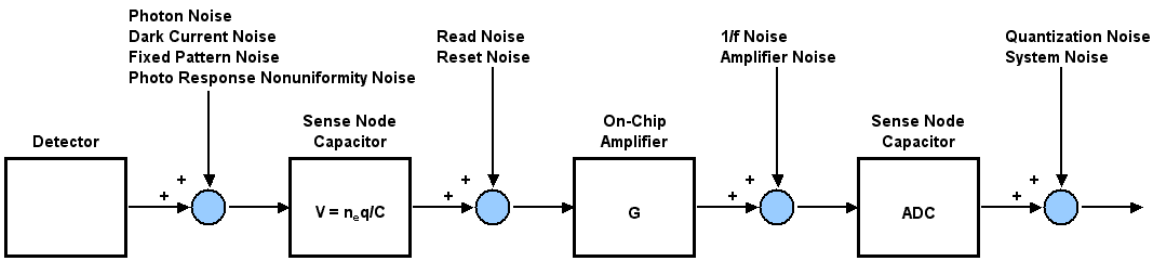

Figure 2.7: Noise transfer diagram.

The temporal (time variant) noise that CMOS sensors encounter includes [92]: photon shot noise, capacitive reset (kTC) noise, dark current time-varying noise, Johnson (thermal or white) noise, and 1/f noise (frequency-dependent). Additionally, CMOS imagers can suffer temporal noise from electrical ground-bounce and coupling noise problems generated by on-chip logic and ADC circuitry. Fixed pattern noise (FPN) is generated in CMOS imagers by pixel variations in dark current and sensitivity, as well as pixel fixed offset. It is common practice to express the values of the noise sources in root mean square (RMS) electron values.

2.3.1.1 Noise Model Simplifications and Assumptions

For many camera systems, an adequate noise model can be constructed using only shot noise, read noise, dark current noise (both fixed pattern and temporal), and PRNU noise [35]. All of these noise sources can be considered to be uncorrelated from pixel-to-pixel [35], [42]. Some of the noise sources are functions of the signal levels [35]. In the development of our PRNU testing methodology, we will make the following commonly used assumptions [35], [42]:

1) All individual noise sources are independent and thus their powers (variances) can be added.
2) All noise components are white (in time and space for temporal noise, and in space for fixed pattern noise).
3) Image processing operations applied to the sensor data will be limited to linear functions.
4) A uniform image model [72] can be used to calculate the DCT-domain quantization error, where it is assumed that the quantization step sizes are reasonably small.

The assumption of linear image processing operations is a reasonable assumption for most of the camera functions [43], such as Bayer interpolation, cross-talk correction, color correction, color space conversion, and DCT transform (see Section 2.4). In order to simplify our model and our noise estimations, we will restrict our image processing modeling to only linear operations. Using the above simplifications, the total pixel noise can be written as:

$$\sigma_{pixel}^2 = \sigma_{shot}^2 + \sigma_{read}^2 + \sigma_{dark\ current}^2 + \sigma_{PRNU}^2 \qquad (2.2)$$

A noise model for a CMOS image sensor can be developed using characterization and sensor performance theory. The model will be a function of the sensor operating conditions, such as exposure time and input signal level.

When we incorporate the camera image processing, we will include quantization due to the JPEG compression (not due to the analog-to-digital converter, ADC) into the pixel noise equation. As listed above, we will use the simplifying assumption of a uniform image model [72] to calculate the DCT-domain quantization error. We will also consider noise amplification due to image processing operations. The effects of the image processing will be taken care of in the camera system model (see Section 2.4).

2.3.2 Noise Models and Photon Transfer Curves

We now look at how the amount of PRNU affects the total noise of the sensor. This relationship will help determine our visibility thresholds for PRNU, as shown in Section 2.5. As we have discussed, we can construct a simplified pixel noise model using Equation (2.2) [35], [42]. In Figure 2.8 we show a typical base gain (lowest internal gain setting of the sensor) noise plot. The sensor used for the noise model is a DVGA

resolution CMOS sensor with 3 transistor (3T) 4μm x 4μm APS pixel architecture. The conversion gain (k) ratio of a sensor is defined as the amount of output generated (in digital number values, DN) per unit charge (e-) created in the pixel [68], and has units of e-/DN. This sensor has a base gain conversion factor of k=28 e-/DN, read noise of 28e-, full well (usable pixel signal range) of 21,000 e-, pixel non-uniformity of 1.0% rms, dark current rate of 1e-/ms, and was operated for a 30ms exposure time. These sensor parameter values were taken from actual measurements of a CMOS sensor [17]. In the plot, shot noise, read noise, dark current (FPN and TN), PRNU noise, and total noise are shown. From the Figure 2.8, we can see that PRNU is the dominant noise source for the majority of the pixel's output signal range. When a sensor is operated at a higher internal gain setting, the output range in the pixel in electrons is reduced. This can be seen in Figure 2.9, where we show the noise plot for an internal gain setting of 4x (k=7 e-/DN). When the sensor is operated at this gain setting, the output signal range over which the PRNU is the dominant noise source is reduced to the point that it is eliminated. The upper output range of the pixel is now limited by the ADC, and is clipped at the maximum output (7168 electrons in this case). The sensor would be set to a larger gain when the amount of light reaching the sensor is lower (high ISO conditions). This can occur for lower lighting conditions, shorter sensor exposure times, or the use of higher f-number lens.

We show the signal-to-noise ratio (SNR) for the sensor in Figure 2.10. The SNR is computed in the usual manner using mean output signal (e-) divided by total noise (e-). We also show the situation when PRNU is removed from the total noise (gain variation set to zero), when only signal shot noise is considered (shot noise limited case), and when only PRNU noise is considered in the SNR calculation. Since PRNU noise is

proportional to signal, the SNR due to PRNU remains constant and independent of sensor output magnitude. It is obvious from the plot that as the output signal approaches the full well capacity of the pixel, the PRNU noise becomes the dominant noise and limits SNR. The point of intersection of the total noise without PRNU SNR curve with the only PRNU SNR curve shows the signal magnitude value when PRNU begins to dominate. The signal value at which PRNU begins to dominate is approximately 10,900 electrons.

In Figure 2.11 we show how variable amounts of PRNU affect the total noise of the sensor. The plot shows that PRNU noise is not perceptible until the PRNU variable gain percentage reaches an amount that causes a 'knee' in the total noise curve [35]. This 'knee' is defined to occur when the total noise without PRNU is equal to the PRNU noise. This occurs when the total noise increases by a factor of $\sqrt{2}$ from its zero PRNU value. We see from the plot that when the pixel is closer to full well, the perceptible PRNU percentage threshold decreases. This is the same as saying that as the pixel gain setting (user selected gain factor that is applied to the pixel data) is increased, the perceptible PRNU percentage threshold increases.

The complete noise performance of an imaging sensor can be determined using the photon transfer curve (PTC) technique [41]. The PTC method is discussed in greater detail in Appendix B. In the method, the rms noise is plotted as a function of the signal level, in unit of electrons. The method can be used to estimate the conversion gain (k) of an imager [68]. The PTC method can be used to calculate a sensor's read noise, full well, linearity, dynamic range, and sensitivity [40]. A PTC is shown Figure 2.12 for our test image sensor. At low input signal levels (low photon fluxes), the noise floor of the

sensor will dominate. This will determine the read noise. As the input signal increases, the photon shot noise will increase. For most well-designed sensors, the sensor will be 'shot noise limited', i.e., the photon shot noise will be the dominant noise. As the charge held by the pixel photodiode approaches saturation, the noise behavior can enter a third region of behavior. This region is dominated by PRNU noise. Thus, the photon transfer curve gives us the following important information: the level at which PRNU will be visible, and the pixel region of operation when PRNU will not be a limiting factor on sensor performance. Sensors can have values of PRNU low enough that the pixel will not be dominated by PRNU noise. But in the case of low cost CMOS sensors, there is usually a PRNU noise dominated noise region. As the input signal increases, the noise will reach a maximum value and then abruptly drop [35]. This defines the saturation point, where electrons will overflow from the pixel into neighboring pixels.

In the PTC, which is plotted on a log-log scale, a read noise region will have a noise-to-signal slope close to zero, a shot noise limited region will have a slope of ½ (noise variance equal to mean signal), and a PRNU limited region will have a slope of unity (noise standard deviation proportional to mean signal). From the PTC shown in Figure 2.12, we can see the three noise regions. For low ISO sensor operation, which has higher signal and SNR, typically pixels be operating in the PRNU region. This is due to a greater range of the pixel's response being exercised. For high ISO sensor operation, which has lower signal and SNR, the PRNU will be less dominant. This is due to a lower range of the pixel's response being exercised. The upper response of the pixel (as it fills up with electrons) will be clipped by the large gain applied (lower value of k).

In the full camera system analysis, we will use the image processing pipeline model as well as the sensor noise model to determine the noise visibility threshold for PRNU. This

will be done in the DCT domain. Quantization noise from the JPEG compression process will also be included in the system noise calculations. The noise values will be a function of the DCT frequency components. The camera system model is presented in Section 2.4.

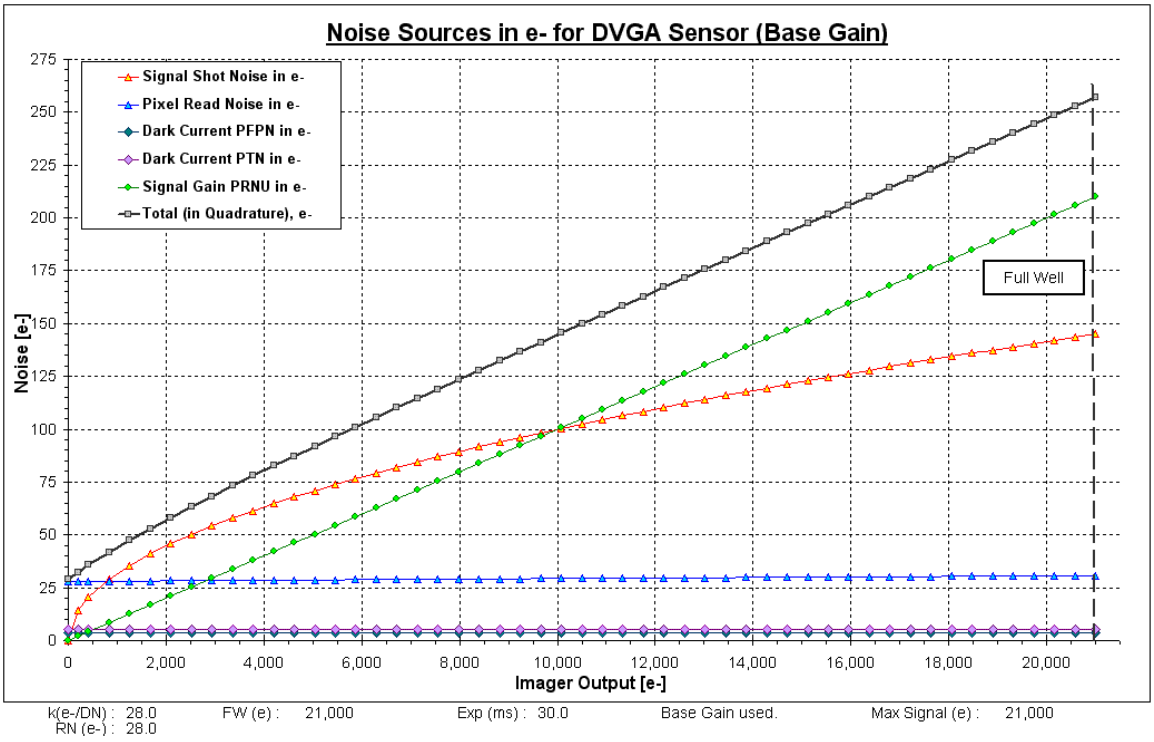

Figure 2.8: Noise versus sensor output for noise sources. DVGA sensor operated at base gain setting (1x). Simulation results based upon measurement values of conversion gain, read noise, dark current noise, and full well for a CMOS sensor [17]. Noise model is constructed using these parameter values.

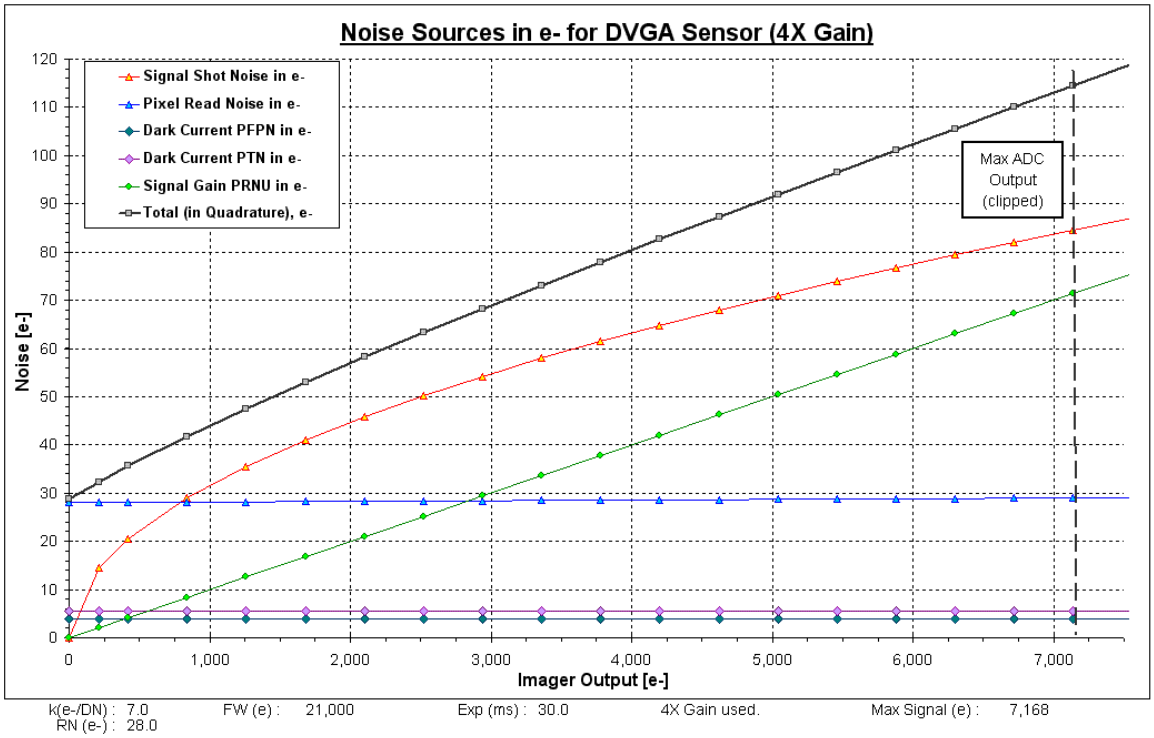

Figure 2.9: Noise versus sensor output for noise sources. DVGA sensor operated at gain setting 4x. Simulation results based upon measurement values of conversion gain, read noise, dark current noise, and full well for a CMOS sensor [17]. Noise model is constructed using these parameter values.

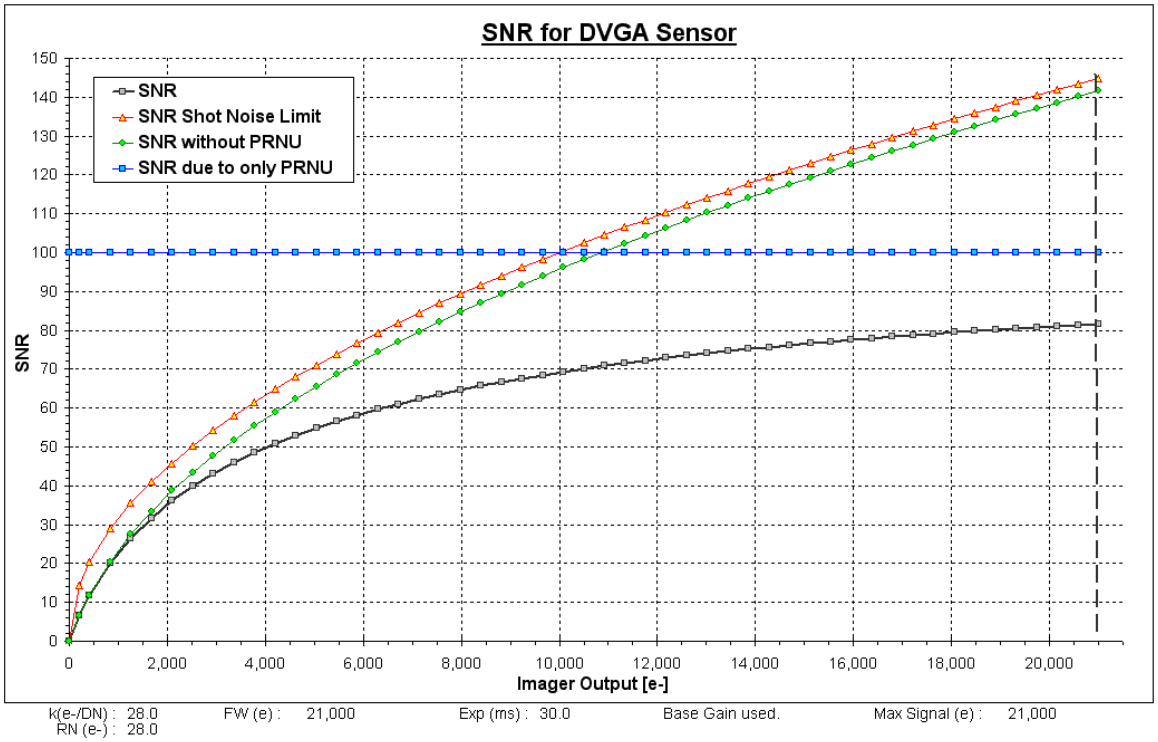

Figure 2.10: Pixel SNR versus sensor output for total noise, shot noise, and total noise with zero PRNU. DVGA sensor operated at base gain setting (1x). Simulation results based upon measurement values of conversion gain, read noise, dark current noise, and full well for a CMOS sensor [17]. Noise model is constructed using these parameter values.

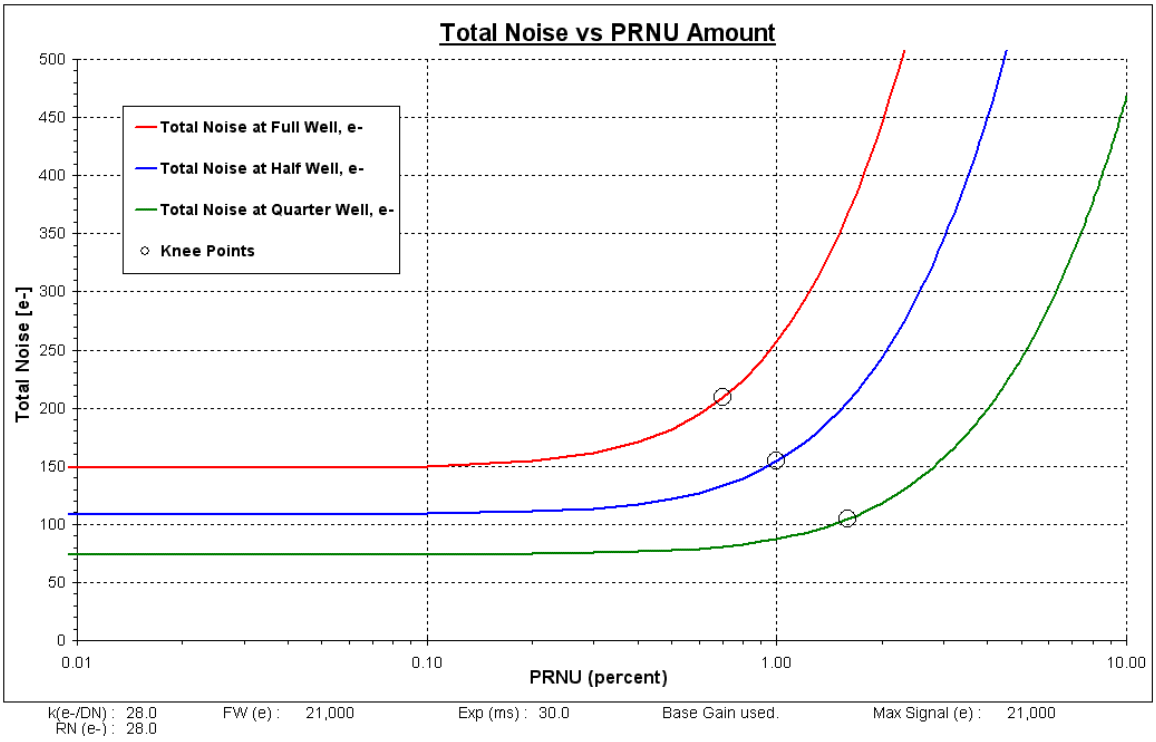

Figure 2.11: Total noise versus PRNU noise factor. DVGA sensor operated at base gain setting (1x). Knee locations indicate that non-PRNU noise and PRNU noise are of equal magnitude. Simulation results based upon measurement values of conversion gain, read noise, dark current noise, and full well for a CMOS sensor [17]. Noise model is constructed using these parameter values.

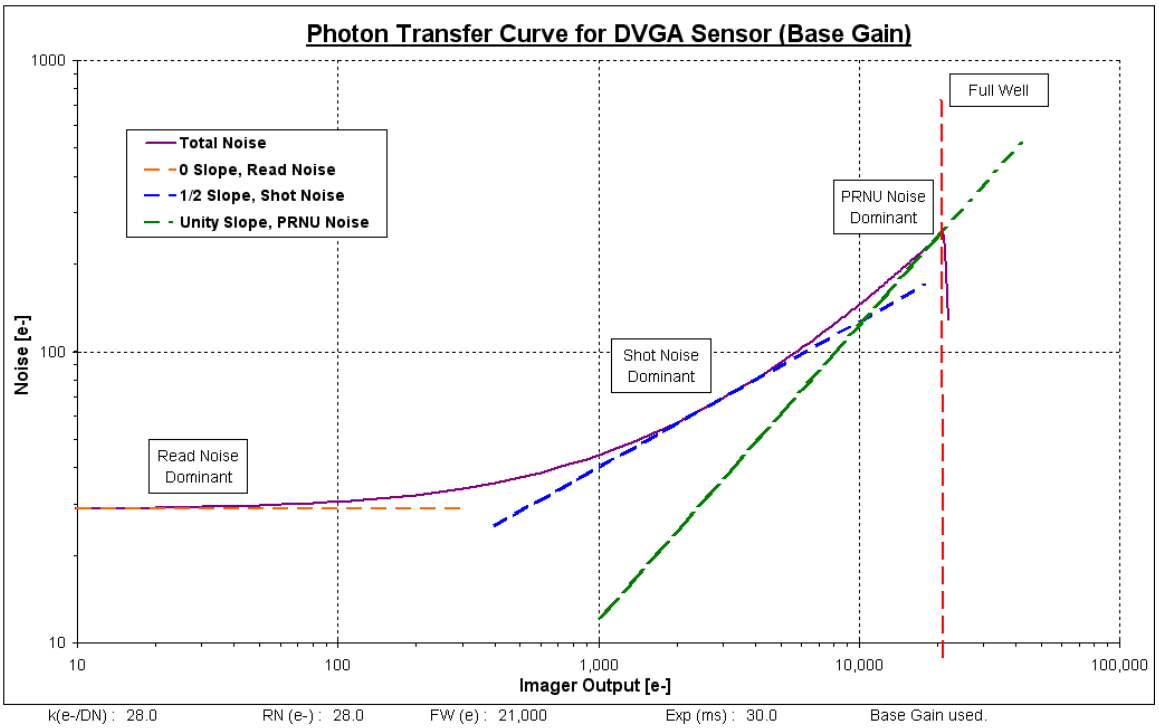

Figure 2.12: Photon Transfer Curve for a DVGA sensor operated at base gain setting. Simulation results based upon measurement values of conversion gain, read noise, dark current noise, and full well for a CMOS sensor [17]. Noise model is constructed using these parameter values.

2.4 Imager System Model

We desire to analyze how input sensor PRNU error leads to final processed error in a camera system after typical image processing of realistic image data (complete with typical noise). We will seek to estimate the distortion between sensor systems that have no PRNU noise and those that have varying degrees of PRNU. We propose to use known or typical probability models for the input image (and noise) data, or alternatively a Monte Carlo approach, where we use a set of images that will cover our input image space. To accomplish this, we need to use an accurate camera system model, which should include an accurate sensor noise model. A diagram used for the system level error tolerance of a camera system is shown in Figure 2.13. The sensor pixels are

subject to noise, including photon shot noise, read noise (including dark current noise), and PRNU. We will use the simplified, but realistic noise model that was developed in Section 2.3. The diagram of Figure 2.13 includes the image-processing pipeline for a typical low-cost consumer camera (including embedded imaging applications). The ideal image input data **F** is first blurred by the camera optics of the system and subsampled by the Bayer color filter array (CFA) pattern of the sensor, producing the image signal **G**. Then signal magnitude dependent photon shot noise ($\mathbf{E}_{SN}$) is modeled as being added to the signal when it reaches the pixel photodiode. Additional blurring of the image data occurs due to signal exchange between local neighborhood pixels (cross-talk effects) [60]. This multi-channel blurring is a multi-color signal convolution, which can be written in the matrix multiplication form: $\hat{\mathbf{Y}} = \mathbf{H}\hat{\mathbf{G}}$. This pixel signal color cross-talk blurring effect will have to be corrected as part of the color correction of the image processing, resulting in some noise amplification [60]. Color cross-talk blurring is discussed in detail in Section 3.1 and Appendix C. We then model the read noise ($\mathbf{E}_{RN}$) as being added to the signal at this point, which produces the distorted image signal $\mathbf{G}_{noise}$. We define the read noise as being the additive noise floor, which includes pixel reset noise, dark current noise (temporal and fixed pattern), and so on.

The PRNU error is represented as the additive term $\mathbf{E}_{PRNU}$. Using our noise and signal models, we can calculate the additive term $\mathbf{E}_{PRNU}$. The value of the multiplicative factor used for the noise is taken from the probability density function of PRNU multiplicative factors. The average PRNU distribution is taken from sensor characterization. Variation in PRNU distributions is modeled as a multiplicative widening of the distribution, which matches well with characterization data (refer to Section 2.3). After the addition of the PRNU errors, the signal $\mathbf{G}_{noise+PRNU}$ is scalar quantized by the on-chip ADC, producing

the output $\mathbf{Y}_{noise+PRNU}$. We represent the output signal from the ADC without the PRNU pixel error effect, but with the other sources of error, as $\mathbf{Y}_{noise}$. The ideal digitized raw pixel data, with no noise sources or cross-talk corruption, is represented as $\mathbf{Y}_{clean}$. Since the pixel ADC quantization step size is small compared to all of the additive noise terms, the quantization noise from the on-chip ADC can be ignored. Typically, the ADC is 10-bit, producing a very fine resolution. We can then write:

$$
\begin{aligned}
&\boldsymbol{G}_{noise} = \boldsymbol{H}(\boldsymbol{G} + \boldsymbol{E}_{SN}) + \boldsymbol{E}_{RN} \ , \\
&\boldsymbol{G}_{noise+PRNU} = \boldsymbol{G}_{noise} + \boldsymbol{E}_{PRNU} \ , \\
&\boldsymbol{Y}_{clean} \approx \boldsymbol{G} \ , \\
&\boldsymbol{Y}_{noise} \approx \boldsymbol{G}_{noise} \ , \textit{ and} \\
&\boldsymbol{Y}_{noise+PRNU} \approx \boldsymbol{G}_{noise+PRNU} \approx \boldsymbol{Y}_{noise} + \boldsymbol{E}_{PRNU}
\end{aligned}
\tag{2.3}
$$

The functional blocks within the dashed rectangle in Figure 2.13 represent the image processing (usually done by the on-chip digital logic) prior to the JPEG quantization. The image processing chain is represented by a function denoted K(). This processing includes the RGB triplet formation from the Bayer data, which can incorporate a separate cross-talk correction [43]. Color correction, involving white balancing and saturation correction follows. This color correction essentially converts the image data from the sensor space to the display space [43]. Often a color space transform is performed here to convert to the YUV or YC_RC_B color space. A noise removal step, such as a median filtering, may be performed, along with edge detection and sharpening. Finally, the DCT linear transform is performed to provide frequency signal information to be used in the JPEG quantization step that follows. The Bayer interpolation, cross-talk correction, color correction, color space conversion, and DCT transform are usually linear operations [43]. We will not consider the possibly non-linear

operations of noise removal and edge enhancement in order to simplify our model and our noise estimations. The output of the image processing chain, which is fed into the quantization block, is denoted as $\mathbf{W}_{clean}$ when the no-noise source and non-cross-talk corrupted input signal $\mathbf{Y}_{clean}$ is used. The output $\mathbf{W}_{noise}$ denotes that input $\mathbf{Y}_{noise}$, which has no PRNU pixel errors but has the other error sources, is used. Finally, $\mathbf{W}_{noise+PRNU}$ represents the output signal for an input containing all of our sources of error, $\mathbf{Y}_{noise+PRNU}$:

$$\begin{aligned} \boldsymbol{W}_{clean} &= K(\boldsymbol{Y}_{clean}) , \\ \boldsymbol{W}_{noise} &= K(\boldsymbol{Y}_{noise}) , \text{ and} \\ \boldsymbol{W}_{noise+PRNU} &= K(\boldsymbol{Y}_{noise+PRNU}) \approx K(\boldsymbol{Y}_{noise} + \boldsymbol{E}_{PRNU}) \end{aligned} \tag{2.4}$$

The quantization performed on the signal W as part of the JPEG compression process is modeled as a function Q(). The noise component values after image processing are denoted by the prime variables $\mathbf{E'}_{SN}$, $\mathbf{E'}_{RN}$, $\mathbf{E'}_{PRNU}$ in Figure 2.13. The variation in noise levels and analog gain factors for image sensors can be modeled by varying the conversion factor for the sensor. This corresponds to varying the electron to digital number conversion (k) parameter.

The amount of cross-talk corruption is determined by the coefficients of the cross-channel matrices used. A general discussion on cross-talk and its modeling can be found in Section 3.1 and Appendix C. As with the noise model, a cross-talk model can be obtained from sensor characterization. Using this complete camera system model, which includes the noise, cross-talk, and image processing pipeline models, we can determine the effects of PRNU corruption for a particular sensor operating under defined conditions (gain setting, exposure time, compression amount, color correction applied, etc).

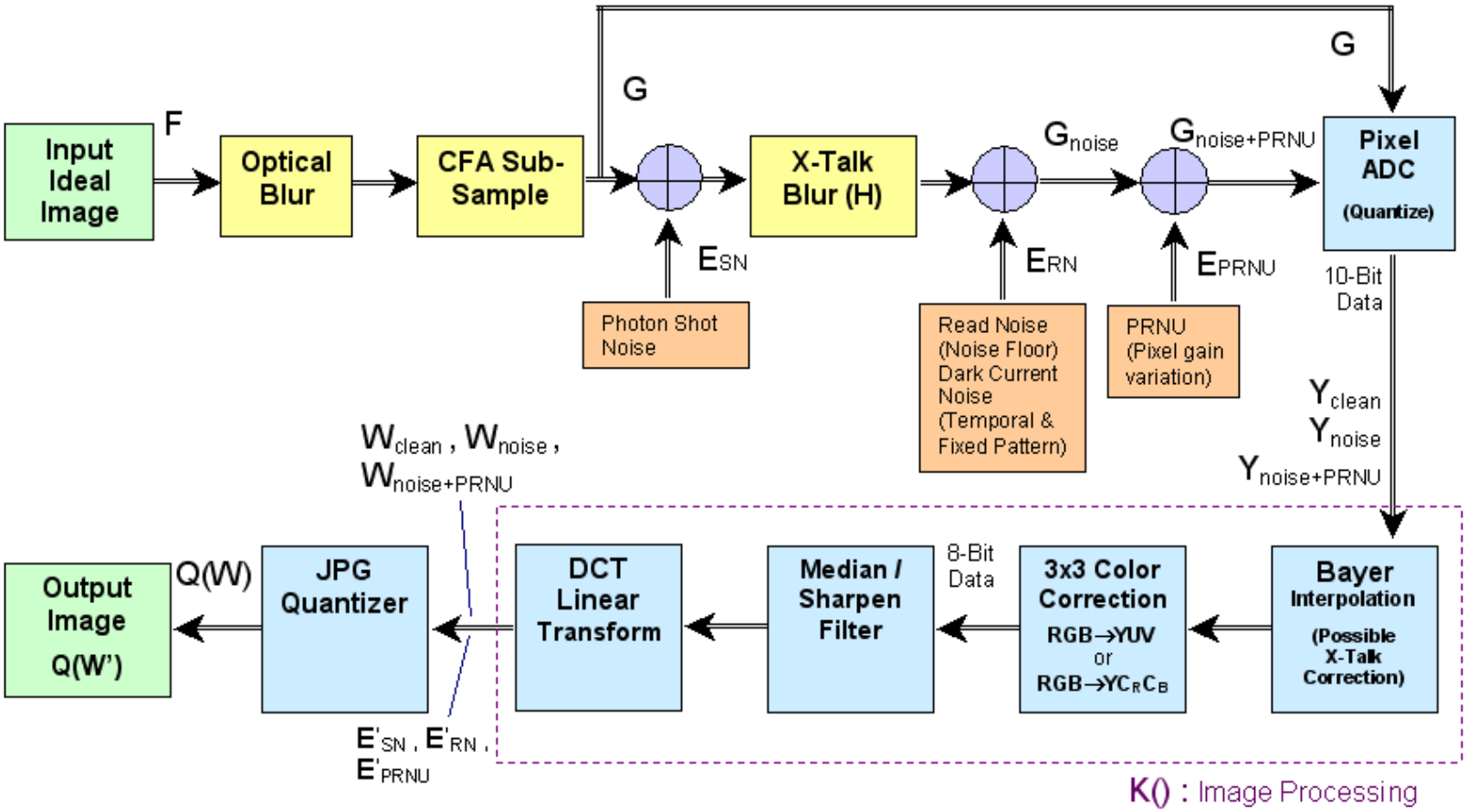

Figure 2.13: System level error tolerance model.
$\mathbf{Y}_{clean}$ ideally has no noise or cross-talk
$\mathbf{Y}_{noise}$ & $\mathbf{Y}_{noise+PRNU}$ both have temporal noise ($\mathbf{E}_{TN}$) & cross-talk,
$\mathbf{Y}_{noise+PRNU}$ is $\mathbf{Y}_{noise}$ with PRNU errors $\mathbf{E}_{PRNU}$

2.5 PRNU Screening Thresholds

In this section, we propose an analytical approach to set the acceptable PRNU error threshold. Error significance is a metric that quantifies the difference between two images (an original one and one affected by error). The derived PRNU error threshold is compared with the measured error significance. The error rate is then defined as the probability that the error significance will exceed our PRNU threshold.

PRNU is screened (error significance) locally by segmenting the image into blocks, and testing each block separately. This approach is justified by the HVS's sensitivity to local signal to noise contrast [7]. Defective pixels are visible against the pixels in the local area. We will determine the visibility of PRNU in the presence of other noise sources, including the quantization of the JPEG DCT coefficients. Thus, we will be measuring the image distortion in the DCT domain. This also allows us to use error detection models that closely match the HVS. The contrast sensitivity of the HVS is a function of the spatial frequency of the image information [7]. This justifies the choice of measuring distortion in the DCT domain.

We use the DCT coefficient error visibility thresholds developed in [88] to define acceptable distortion limits. Although this is a relatively old model, it provides a conservative visibility threshold, which will be sufficient for our use. The visibility thresholds are defined for luminance and chrominance errors in the DCT domain using detection models. In that paper, models that predict HVS detectability of quantization error in color space are developed. For each DCT frequency component (u,v), an error threshold ($E_{th}(u,v)$) is determined based on the perceptual threshold of the HVS. These

DCT perceptual error thresholds can be used as a measure of distortion. The DCT perceptual error thresholds are listed in Table 2.3 [88].

Table 2.3: DCT frequency component (*u*,*v*) perceptual error thresholds, used as measures of distortion.

Y quantization matrix =

14	10	11	14	19	25	34	45
10	11	11	12	15	20	26	33
11	11	15	18	21	25	31	38
14	12	18	24	28	33	39	47
19	15	21	28	36	43	51	59
25	20	25	33	43	54	64	74
34	26	31	39	51	64	77	91
45	33	38	47	59	74	91	108

C_r quantization matrix =

20	34	39	52	70	95	127	168
34	43	40	45	57	74	96	125
39	40	58	67	77	93	115	144
52	45	67	89	107	125	147	177
70	57	77	107	136	163	191	223
95	74	93	125	163	202	240	280
127	96	115	47	191	240	291	342
168	125	144	177	223	280	342	408

C_b quantization matrix =

29	49	101	132	179	243	325	428
49	110	101	114	144	188	245	319
101	101	148	170	197	237	294	367
132	114	170	227	272	318	376	451
179	144	197	272	347	415	486	569
243	188	237	318	415	514	611	713
325	245	294	376	486	611	741	873
428	319	367	451	569	713	873	1040

The HVS perceptual thresholds can be adjusted to take into account the masking effects of the presence of other noise sources. The PRNU noise will not be detectable until its energy exceeds that of the system's total random, uncorrelated, non-structured noise

[35]. As shown in Section 2.3.1.1, it is reasonable to assume that the sensor's non-fixed pattern noise sources are random, uncorrelated, and non-structured. The system noise variance, following image processing, can be simplified as:

$$\sigma_{sys}^2(u,v) = \sigma'^2_{shot}(u,v) + \sigma'^2_{read}(u,v) + \sigma'^2_{dark\ current}(u,v) + \sigma'^2_{PRNU}(u,v) + \sigma_{quant}^2(u,v)\ , \quad (2.5)$$

where σ_{quant} is due to the JPEG quantization, not the ADC quantization. The prime on the noise terms signifies that values are found after the image processing (which is assumed to be linear and are prior to JPEG quantization), as denoted by the $\mathbf{E}'_{SN}$, $\mathbf{E}'_{RN}$, $\mathbf{E}'_{PRNU}$ terms in Figure 2.13. We also observe that the noise terms are in the frequency domain (u,v). Thus, the noise terms (as well as the image signal) have been operated on by the image processing pipeline, K(), shown in Figure 2.13. The differences between this system noise equation and Equation (2.2) of Section 2.3.1.1 are that the system noise has been operated on by the image processing pipeline (which includes a transformation to the DCT frequency domain) and has had the affects of JPEG quantization added. The signal independence and linearity assumptions of Section 2.3.1.1 still apply.

From the system noise equation, we see that for conditions that result in greater total system noise, the PRNU component becomes less significant. The total system noise can increase when we apply greater compression (σ_{quant} increases) or have greater exposure times (dark current noise can increase). For low signal situations (e.g., low light or short exposure time), the camera system will usually apply greater sensor gain. This magnifies the total noise, but will usually not affect the overall SNR (signal/σ_{noise_floor}), since both noise and signal are being amplified. However, the PRNU

noise will be low compared to the noise floor for low signal situations. Thus, the amount of PRNU that will be acceptable will be dependent upon the operating conditions of the sensor. Similar to what was done in Section 2.3, we consider the PRNU noise (in the DCT domain) to be masked (imperceptible) when the following relationship holds:

$$\sigma'^{2}_{PRNU}(u,v) < \sigma^{2}_{sys\text{-}PRNU}(u,v) = \sigma'^{2}_{shot}(u,v) + \sigma'^{2}_{read}(u,v) + \sigma'^{2}_{dark\_current}(u,v) + \sigma^{2}_{quant}(u,v) \quad (2.6)$$

The PRNU limit is set as the noise variance of PRNU that is equal to the sum of the noise variances of the remaining noise sources that make up the total system noise ($\sigma^2_{sys\text{-}PRNU}$). We are allowing for different noise levels for different DCT coefficients (u,v). The individual noise terms may be white, but we leave the computations open to the possibility of frequency dependency. The acceptable PRNU level will depend upon the image processing applied to the sensor raw data (K{ }). For example, high amounts of color correction (saturation enhancement or pixel cross-talk correction) will amplify noise terms (refer to Figure 2.13 and to Appendix C).

The noise comparison approach of Equation (2.6) is similar to that presented in [35], where after applying simplifying assumptions, it was determined that PRNU will not be detectable (i.e., will be masked) when the following condition holds true:

$$\sigma_{PRNU} < \sigma_{shot\_noise} \quad (2.7)$$

Since there is a cost associated with reducing PRNU in a sensor, the optimal PRNU value was defined in [35] to be:

$$\sigma_{PRNU\_optimal} = \sigma_{shot\_noise} \quad (2.8)$$

For a pixel with a full well capacity of n_{pe} photo-electrons, Equation (2.8) gives us the simplified optimal PRNU factor (U) value:

$$U = \{n_{pe}\}^{-1/2} , \tag{2.9}$$

where $\sigma_{PRNU} = Un_{pe}$.

In Equation (2.7) approximation used in [35], all other noise sources are ignored. This general idea is related to the approach used in this thesis. However, we provide a more detailed noise model, as well as using a model of the camera system image processing.

As discussed in Section 2.3.2, the photon transfer curve method characterizes the pixel's photon shot noise, noise floor (read noise and dark current noise), and PRNU. The photon transfer curve shows the region of pixel response where PRNU will be significant. In this region, PRNU noise will become visible and will limit the pixel's SNR. A plot of the noise components and total system noise versus pixel response can also be used to determine the PRNU perceptual threshold. We will use the pixel noise and camera system models to determine the PRNU perceptual distortion threshold using the equation:

$$Th(u,v) = max\{ E_{th}(u,v) , \sigma_{sys\text{-}PRNU}(u,v) \} \tag{2.10}$$

The PRNU threshold (Th) is in the DCT frequency component domain (u,v), thus the total system noise without PRNU ($\sigma_{sys\text{-}PRNU}$) is also computed in that domain. This can be done by using our known models for pixel noise and image processing. The above equation for the PRNU perceptual distortion threshold defines the visibility of PRNU noise in the DCT frequency component domain.

In the equation for the perceptual distortion threshold, we are using the typically valid assumptions for the noise sources that were listed in Section 2.3.1.1 (assumed to be ideally independent noise sources which are white). For this situation, noise sources cannot be visibly distinguished in the image [35]. We are not considering 'structured noise', such as column fixed pattern noise (CFPN) or row temporal noise (RTN). The SNR will not be appreciably affected by PRNU until $\sigma_{PRNU}^2 > \sigma_{sys\text{-}PRNU}^2$. This behavior is shown in Figures 2.10, 2.11 and 2.12.

The quantization noise variance in the spatial domain can be written as a function of the variance in the DCT-domain:

$$\sigma_{quant}(m,n)^2 = \sum_{u=0}^{N-1} \sum_{v=0}^{N-1} \boldsymbol{H}(v,m)^2 \boldsymbol{H}(u,n)^2 \sigma_{quant}(u,v)^2 , \qquad (2.11)$$

where $\mathbf{H}(m,n)$ are the elements of the DCT real unitary transform matrix, and $\sigma_{quant}(u,v)^2$ is the variance in the DCT-domain as a function of the frequency components (u,v). As was done in [72], we can use the simplifying assumption of a uniform input image model, which says that there is no prior knowledge of the frequency components values and their values are uniformly distributed within the quantization interval. This gives us the DCT-domain quantization error as:

$$\sigma_{quant}(u,v)^2 = \{ \Delta q(u,v)_i \}^2/12 ,$$
$$\Delta q(u,v)_i = q(u,v)_{i+1} - q(u,v)_i \qquad (2.12)$$

In the above equation, $\Delta q(u,v)_i$ is the quantization step size for a given DCT frequency component (u,v). If we were to use the same assumption of a uniform input image, the values of σ_{shot}^2, σ_{read}^2, and $\sigma_{dark\_current}^2$ would be independent of frequency component

(u,v). This would be an assumption that the noise sources are white, and the same noise variances could be used for all frequency components, with the exception of the DCT-domain quantization noise. This assumption would allow us to develop a simple and easily calculated PRNU threshold. If desired, we could instead use a non-uniform distribution image model to develop noise frequency component values.

However, since we have noise and image processing models, we have the option to simply use the data from Monte Carlo simulations to calculate the noise frequency component values (see the $\mathbf{E}'_{SN}$, $\mathbf{E}'_{RN}$, $\mathbf{E}'_{PRNU}$ terms in Figure 2.13). These noise frequency component values, σ'_{shot}, σ'_{read}, and $\sigma'_{dark\_current}$, can then be used to calculate the total system noise without PRNU components ($\sigma_{sys\text{-}PRNU}(u,v)$) utilized in the threshold ($Th(u,v)$) calculation. In a Monte Carlo simulation approach, we can select a set of input images and camera operating conditions that will cover the particular camera application targeted. Sensor characterization noise models are used to create the noise component values. Once a robust Monte Carlo simulation has been performed, input raw sensor PRNU values can be related to error rates for the prescribed set of camera operating conditions. Multiple camera operating conditions can be used, so that categorizing of sensors can be applied. Sensors that fail to meet the PRNU error rate requirements of one application may meet the requirements of another.

The concept of the acceptable magnitude of a noise source being set by the total noise of system has been previously used. The methods of [65] and [57] address different problems by taking into consideration quantization noise. In [65], a class of non-linear filters called Occam filters was used to remove system noise by increasing quantization noise through compression. Random noise was removed from a signal by applying a

lossy data compression algorithm with the loss threshold set equal to the noise strength ($\varepsilon = \sigma_{Noise}^2$). In [57], a pixel scalar quantizer is developed that utilizes knowledge of a sensor's performance characteristics. The decision and reconstruction levels of a non-uniform quantizer are determined from the noise versus signal characteristics of the sensor. The quantization step sizes q_i are set proportional to the noise amplitude, as a function of sensor output signal level. Again, in this thesis, we instead compare PRNU noise with the magnitude of the other noise sources.

2.6 Camera System Level PRNU Distortion Metric and Error Rate

2.6.1 Distortion Metric

Having discussed the pixel noise and camera system models, we will now discuss how the PRNU distortion is calculated using these models. The difference between a reference image and a corrupted image is termed as distortion (*D*). In [88] and [90] a perceptual objective metric is developed that evaluates the distortion distance (*D*) between a reference and degraded image. We wish to quantify how the addition of PRNU corrupts (degrades) image quality. This degradation is our error significance. Thus, we need to look at image quality when the other sources of degradation are present (e.g., temporal noise, cross-talk, JPEG quantization), with and without the effects of PRNU.

2.6.1.1 PRNU Distortion Metric Extension from DCT Hardware

In the development of our PRNU distortion metric, we have extended the work published in [12] and [13], which developed error tolerances for DCT hardware faults. Our work extends and adapts the work of [12] and [13] in the following manner:

1) As was done in [13], we use an error significance metric that compares these two decoded (fully processed) images. However, our two images have the camera system image processing, including JPEG compression, applied to them. In [13], the processing was limited to the JPEG compression. In a method analogous to that used in [12] and [13], we compare these two images indirectly by computing their individual distortions relative to an ideal, non-corrupted image.

2) In [12], only errors introduced by DCT hardware faults (the errors under investigation) and compression are considered. In our work, in addition to the PRNU errors, we consider distortion due to JPEG quantization, non-PRNU system noise, and image processing noise amplification. This complicates our distortion calculations, and increases the number of possible distortion cases from than of [12]. A closed form solution of the error rate equation becomes more difficult.

3) We use the DCT basis for coefficient error visibility thresholds [88] for error tolerance, as was done in [12] and [13]. Additionally, we introduce the use of the masking effects of the camera system processed noise to determine the PRNU tolerance errors.

4) In [13], testing was performed on each block of DCT frequency components. We also test each DCT block and apply a Peak Contrast model, which marks a block as failing if any of its frequency components fails the threshold test. This strategy is consistent with the industry standard approach to measuring local PRNU.

2.6.1.2 PRNU Distortion Metric Definition

Our error significance metric will measure the distortion between images with and without PRNU. The metric will be compared with Watson's DCT basis for coefficient error visibility thresholds [88], as used in [12], [13]. As was discussed in Section 2.5 when we developed our threshold equations, we also compare this metric against the total system noise without the contribution of PRNU. Referring to the system model of Figure 2.13, we define three images to use in the calculation of the PRNU distortion metric. The first image, $\mathbf{W}_{clean}$, is the 'ideal' or 'clean' image that has been image

processed by the camera system (it is also written as simply **W**). This ideal image has not been operated on by the JPEG quantizer, and has no photon shot noise, read noise, or PRNU noise added. The second image, $\mathbf{Q}(\mathbf{W}_{noise})$, is the image with photon shot noise and read noise added, which has been quantized by the JPEG quantizer. The third image, $\mathbf{Q}(\mathbf{W}_{noise+PRNU})$, is the same as $\mathbf{Q}(\mathbf{W}_{noise})$ but with PRNU noise also added.

In our developed PRNU testing method, we measure block-by-block errors. This approach matches the way that PRNU errors are typically measured. The JPEG DCT block size of 8 by 8 pixels is within the industry standard range of block sizes used for PRNU testing. The blocks within the three images are denoted using a superscript bar as $\bar{\mathbf{W}}_{clean}$, $\mathbf{Q}(\bar{\mathbf{W}}_{noise})$, and $\mathbf{Q}(\bar{\mathbf{W}}_{noise+PRNU})$. Individual DCT frequency coefficients within a block are denoted as $W_{clean}(u,v)$, $Q(W_{noise}(u,v))$, and $Q(W_{noise+PRNU}(u,v))$, where (u,v) are the DCT frequency coefficients. As was done in [13], we look at the distortion metrics at the image, block, and DCT frequency component levels. These distortions are denoted D_I, D_B, and D_C, respectively.

Following the nomenclature used in [13], three different distortion metrics are defined by:

$$
\begin{aligned}
D^1 &= D(\mathbf{W}_{clean}, \mathbf{Q}(\mathbf{W}_{noise})) , \\
D^2 &= D(\mathbf{W}_{clean}, \mathbf{Q}(\mathbf{W}_{noise+PRNU})) , \\
D^3 &= D(\mathbf{Q}(\mathbf{W}_{noise}), \mathbf{Q}(\mathbf{W}_{noise+PRNU})) \qquad (2.13)
\end{aligned}
$$

In the above equations, D is the basic distortion distance metric, which can be applied to the entire image (I), an image block (B), or a block frequency component (C). D^1 is the distortion between the ideal image and one that has typical noise (read noise, shot noise) along with JPEG DCT frequency quantization (where we have a quantization bin size Δ). D^2 is the distortion between the ideal image and one that has typical noise (read

noise, shot noise), PRNU noise, and JPEG DCT frequency quantization (bin size Δ). Distortions D^1 and D^2 are shown in Figure 2.14. Finally, D^3 is the distortion between the ideal image corrupted with typical noise (read noise, shot noise) and DCT quantization, and one that has also had PRNU noise added (these images might be referred to as decoded images). All of the images have had the standard image processing operations applied to them (color correction, etc.), which can result in noise amplification. Similar to [12] and [13], we will be comparing $\mathbf{Q}(\mathbf{W}_{noise})$ and $\mathbf{Q}(\mathbf{W}_{noise+PRNU})$ indirectly by computing D^1 and D^2 and comparing these distortions. We will discuss later in this section why the difference between D^2 and D^1 is used as our metric instead of the difference between $\mathbf{Q}(\mathbf{W}_{noise+PRNU})$ and $\mathbf{Q}(\mathbf{W}_{noise})$ (D^3). If the difference between D^2 and D^1 is small enough, then we will conclude that the PRNU will be acceptable. Unlike [12], the addition of the error does not always result in $D^2 \geq D^1$, since we have multiple sources of distortion for D^1 and D^2. Due to the multiple random noise sources and the image processing applied to them, it is more difficult to determine a closed form equation for the error rate (P_O) than in the system model of [12].

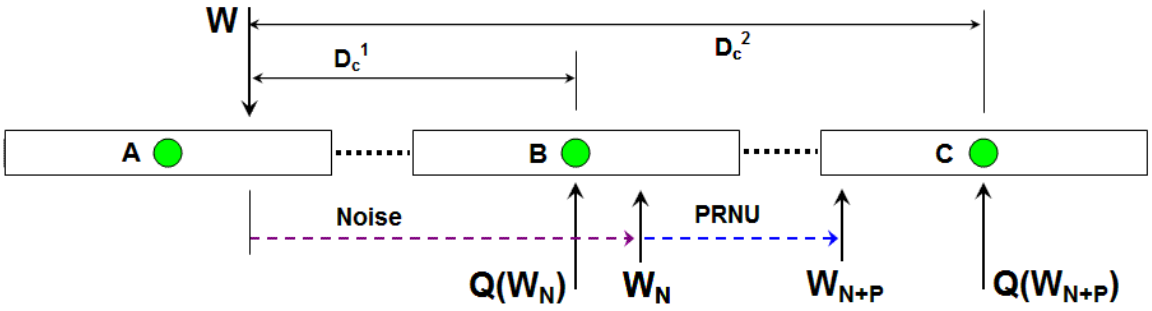

Figure 2.14: Relationship of distortions D^1 and D^2, along with $\mathbf{W}$, $\mathbf{W}_N$ and $\mathbf{W}_{N+P}$ and their quantized values. Photon shot noise and read noise combined with quantization distorts the input signal value $\mathbf{W}$ to $\mathbf{Q}(\mathbf{W}_N)$. The addition of the noise sources, including PRNU, combined with quantization distorts the input signal value $\mathbf{W}$ to $\mathbf{Q}(\mathbf{W}_{N+P})$. We are interested in the increase in distortion, from D^1 to D^2, due to PRNU.

As we have stated, using the block distortion as a metric (D_B) for PRNU screening follows the industry approach to testing and matches the sensitivity of the HVS to local noise [7]. Thus we will also measure block-by-block error (rather than applying a spatial pooling approach). Additionally, since we wish to have our distortion metric follow the sensitivities of the HVS, we use the DCT frequency component visibility thresholds ($Th(u,v)$) of [88], as was done in [12], [13]. The Minkowski metric is used to pool all of the transform coefficient errors ($D_C(u,v)$) of a block, and is given as:

$$D_k = \{ \sum_{u,v} D_k(u,v)^b \}^{1/b} \tag{2.14}$$

where D_k is the metric for block k (D_B), $D_k(u,v)$ are the threshold weighted absolute differences for the frequency components (u,v), and b is the pooling exponent. The error components (differences) for each frequency are weighted by the perceptual thresholds ($Th(u,v)$). For the Peak Contrast model, the pooling operation consists of choosing the pixel with the largest absolute value [87]. This corresponds to the Minkowski metric with the exponent b set to ∞. The Minkowski exponent controls the efficiency of the summation over the transform's coefficients. Linear summation occurs with b set to 1, while no summation (maximum selection) occurs with b set to ∞. We use Minkowski pooling for the block DCT frequencies using the Peak Contrast model ($b = \infty$), on a block-by-block basis. The distortion metric for a block is the largest absolute error of that block. This is the greatest $D_C(u,v)$ value of the block relative to (weighted by) the corresponding threshold. This is similar to the conventional PRNU testing method of using the maximum and minimum pixel values in each block for testing (peak-to-peak PRNU), and not considering the remaining pixels in a block. However, it is done in the

transform domain. Any block that has 1 or more DCT frequency components that exceed the allowable distortion threshold is therefore marked as a defective block. Thus the Peak Contrast model (Minkowski metric $b = \infty$) is in accordance with the PRNU peak-to-peak method, and fits in with our goal of improving PRNU screening for CMOS sensors. MSE does not measure PRNU well due to its value smoothing of outliers, while the PRNU measurement is mostly concerned with outliers. This was illustrated in Figure 2.5.

From the noise modeling assumptions of Section 2.3.1.1, the image **G** of Figure 2.13 is independent of the PRNU, read noise, and shot noise errors ($\mathbf{E}_{PRNU}$, $\mathbf{E}_{RN}$, and $\mathbf{E}_{RN}$). The individual DCT components of the noise terms ($E_{PRNU}(u,v)$, $E_{RN}(u,v)$, and $E_{SN}(u,v)$) are random additive error terms independent of the image DCT components ($G(u,v)$). Using sensor characterization data, we have models (and pdfs) for the $\mathbf{E}_{PRNU}$ and $\mathbf{E}_{RN}$ errors (refer to Section 2.3). The model (and pdf) for the shot noise error, $\mathbf{E}_{SN}$, is also known (from the nature of photon arrivals). Finally, the pdf of the image **G** can either come from a typical image, or a Monte Carlo approach can be used to ensure that we use an accurate and realistic distribution of images. In this thesis, we will use both a Monte Carlo approach and a probability model-based analysis. The spatial distribution of the PRNU within blocks will affect the errors of the DCT components (u,v).

In analyzing how the addition of PRNU ($\mathbf{E}_{PRNU}$) leads to additional error in the presence of standard sensor noise and standard image processing including scalar quantization (JPEG), we will use the absolute difference of the DCT coefficients as a distortion metric. This choice reduces the computational complexity. The distortions due to typical noise along with JPEG DCT frequency quantization (D_C^1), and due to typical noise plus PRNU

noise and JPEG DCT frequency quantization (D_C^2) are then given by the distortion distances (refer to Figure 2.14):

$$D_C^1 = | W_{clean} - Q(W_{noise}) | \text{, and}$$
$$D_C^2 = | W_{clean} - Q(W_{noise+PRNU}) | \qquad (2.15)$$

There will be cases where the $\mathbf{E}_{PRNU}$ error is masked by the quantization process (and perhaps by other operations in the image processing). Thus we may have:

$$W_{noise} \neq W_{noise+PRNU} \text{ (and also } G_{noise} \neq G_{noise+PRNU}),$$

but still have:

$$Q(W_{noise}) = Q(W_{noise+PRNU}).$$

This situation can be seen in Figure 2.15. As the JPEG quantization becomes greater (quantization bin size Δ increases), the likelihood of $Q(W_{noise})$ and $Q(W_{noise+PRNU})$ being different (mapped to different levels) decreases. $Q(W_{noise})$ and $Q(W_{noise+PRNU})$ are related by the integer number of quantization bins between them (K):

$$Q(W_{noise+PRNU}) = Q(W_{noise}) \pm K\Delta$$

What we are truly concerned about is how PRNU adds to the distortion of the decoded image $\mathbf{Q}(\mathbf{W}_{noise+PRNU})$ with respect to the ideal image $\mathbf{W}$. We show graphically in Figure 2.16 how the addition of PRNU can sometimes reduce this distortion. This happens when the PRNU error and the other noise source errors have opposite signs. This situation is different from that presented in [12], where the relationship $D_C^2 \geq D_C^1$ was always true. This provides further justification for the use of the following metric equation for the perceptual distance between $Q(W_{noise})$ and $Q(W_{noise+PRNU})$:

$$\Delta D_C = D_C^2 - D_C^1 \ , \quad \text{if } D_C^2 > D_C^1$$

$$\Delta D_C = 0 \ , \quad \text{else} \tag{2.16}$$

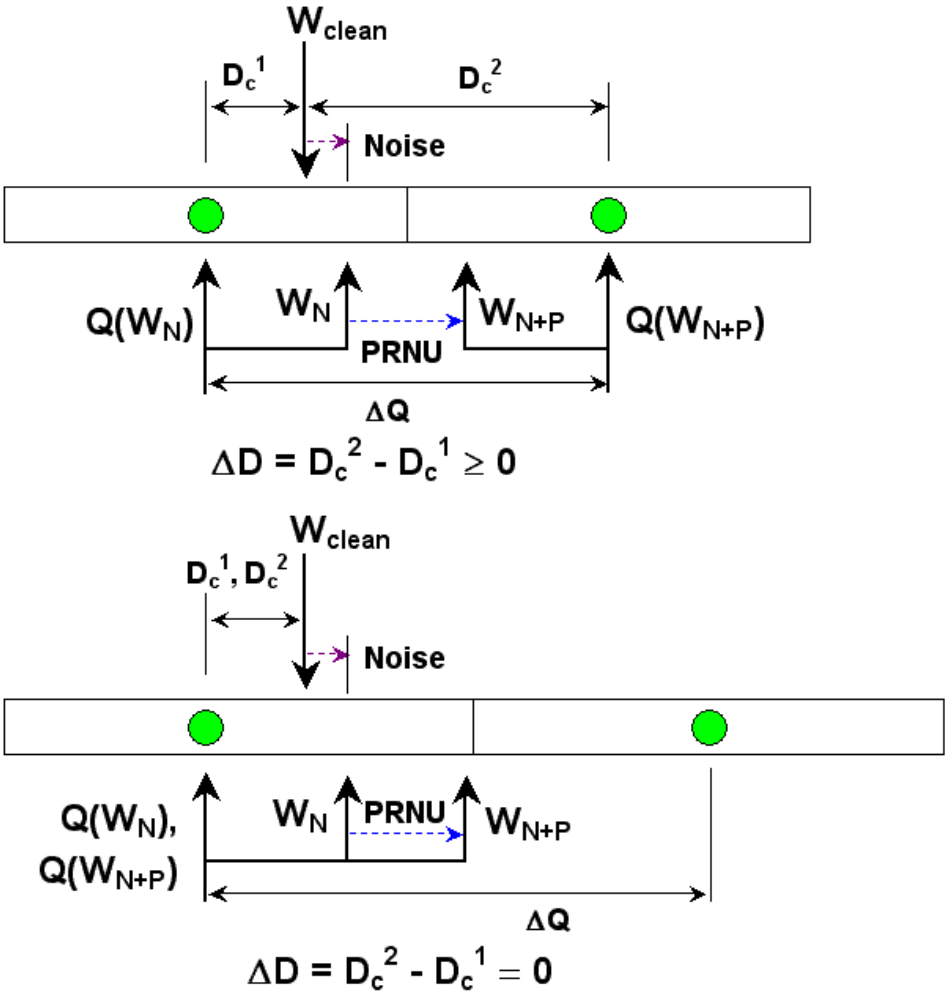

Figure 2.15: Example showing relationship of quantized signals and quantization bin size. The upper portion of the figure shows a smaller quantization bin size that results in $Q(\mathbf{W}_N)$ and $Q(\mathbf{W}_{N+P})$ being in different bins, while the lower portion shows the two quantized signals being in the same bin for a larger bin size. We see how the noise terms (PRNU and non-PRNU noise) affect the quantization of the input image data **W**. As the bin size shrinks, the corrupted signal $\mathbf{W}_{N+P}$ enters the adjacent bin.

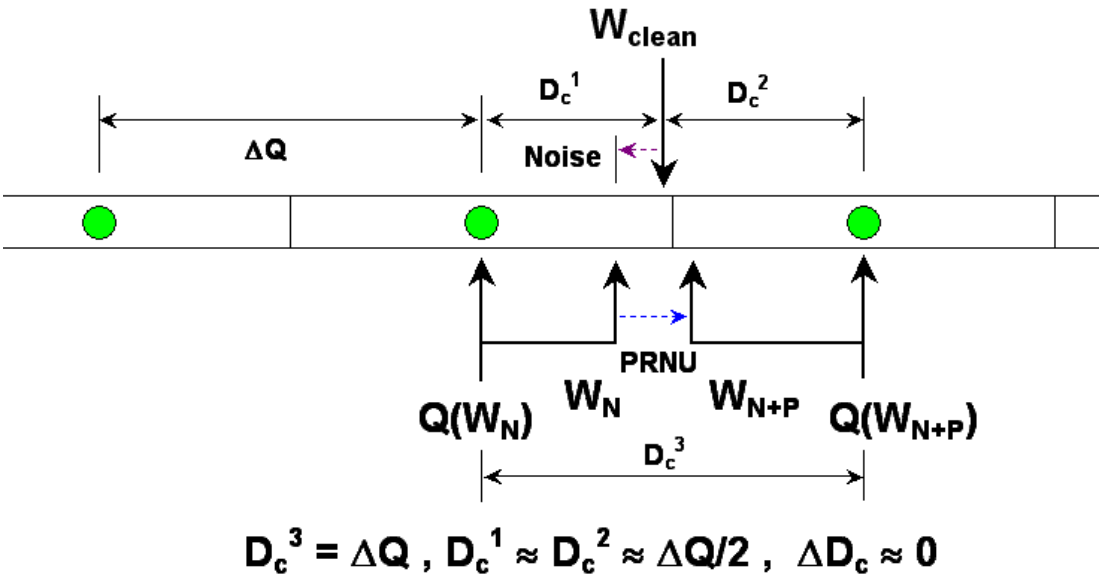

Figure 2.16: Example showing how distortion metric D_C^3 can be a poor metric for measuring PRNU distortion. Here, D_C^3 has a large value, however, the distortion with and without PRNU is the same (D_C^1=D_C^2). We also see that PRNU and non-PRNU noise can have opposite signs.

As was shown in [12], using the metric $D^3 = D[Q(W_{noise}), Q(W_{noise+PRNU})]$ can be a poor choice for a distortion metric. This can be seen when both W and W_{noise} are near the boundary of a quantization bin, and the addition of a small PRNU error, e_{PRNU}, results in $Q(W_{noise})$ and $Q(W_{noise+PRNU})$ being in adjacent bins. This would result in $D_C^3=\Delta$, and $D_C^2 \approx D_C^1 \approx \Delta/2$, for a quantization bin size of Δ. This situation is depicted in Figure 2.16. Obviously, this large distortion metric value of D_C^3 is not a good indication of the relatively small distortion due to the PRNU error. This supports our choice of the metric ΔD_C shown above as a measurement for distortion.

The permutations of the W, W_{noise}, $W_{noise+PRNU}$ along with the quantization bin size results in 5 different distortion cases that can be grouped into 2 different categories, as listed below. Some of these cases result in zero distortion.

1) Low noise case: W_{noise} is in the same bin as W, ($Q(W_{noise}) = Q(W)$). We have two subcases:

   a) $W_{noise+PRNU}$ is also in the same bin as W ($Q(W_{noise+PRNU}) = Q(W_{noise}) = Q(W)$), which results in zero distortion.

   b) $W_{noise+PRNU}$ is in a different bin than W ($Q(W_{noise+PRNU}) \neq Q(W_{noise}) = Q(W)$), which results in non-zero distortion as shown in Figures 2.17 and 2.18 (for $D_C^2 < \Delta Q$ and $D_C^2 > \Delta Q$).

2) High noise case: W_{noise} is in a different bin than W ($Q(W_{noise}) \neq Q(W)$). We have three subcases:

   a) W_{noise} and $W_{noise+PRNU}$ are both in the same bin, which is different than the bin for W ($Q(W_{noise}) = Q(W_{noise+PRNU}) \neq Q(W)$), which results in zero distortion as shown in Figure 2.19.

   b) $W_{noise+PRNU}$ is in a different than W_{noise} and W ($Q(W_{noise}) \neq Q(W_{noise+PRNU}) \neq Q(W)$), which results in non-zero distortion as shown in Figure 2.20.

   c) $W_{noise+PRNU}$ is in the same bin as W ($Q(W_{noise}) \neq Q(W_{noise+PRNU}) = Q(W)$), which results in zero distortion.

Cases 1a and 1b correspond to the A0 and A1 cases of [12], respectively. Case 1a has been shown to have $\Delta D=0$ ($D_C^1=D_C^2$). Similarly, cases 2a and 2c will result in $\Delta D=0$ (both these cases also have $D_C^1=D_C^2$). Thus, only cases 1b and 2b will have non-zero distortion measurements. The case information and distortion equations are summarized in Table 2.4, and shown graphically in Figures 2.17 through 2.20. The relative magnitudes of the noise terms E_{SN}, E_{RN}, E_{PRNU}, the quantization step size (Δ), the cross-talk (**H**) and the image processing (**K**{}) will determine the distortion measurement behavior.

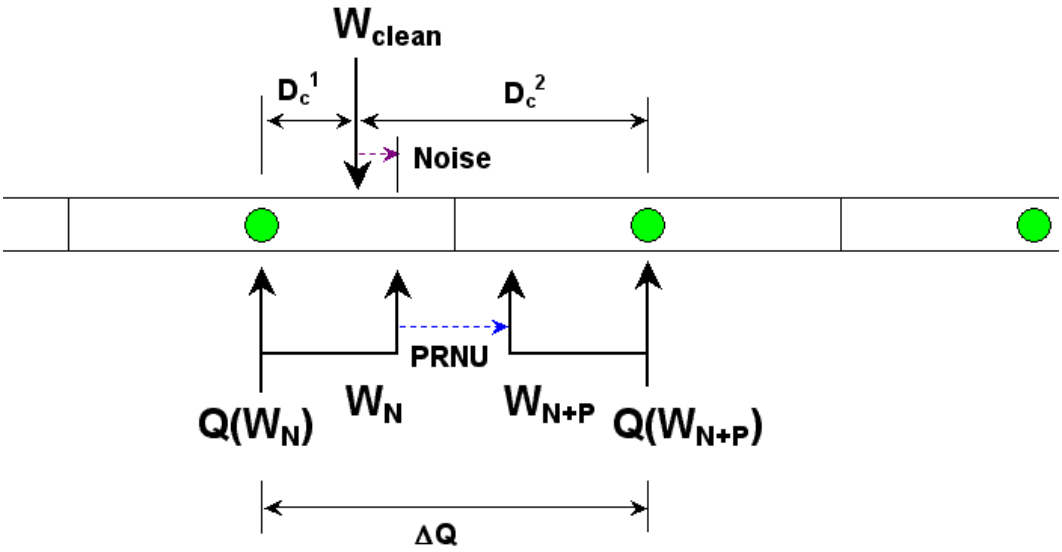

$$\Delta Q \geq \Delta D = D_c^2 - D_c^1 \geq 0 \;,\; D_c^2 \leq \Delta Q$$

Case 1b: W_{clean} & W_{noise} are in same bin, $W_{noise+PRNU}$ is in adjacent bin, and $D_c^2 \leq \Delta Q$

Figure 2.17: Case 1b, with $D_C^2 < \Delta Q$, PRNU forces quantized signal to next bin, but distortion is less than quantization step size.

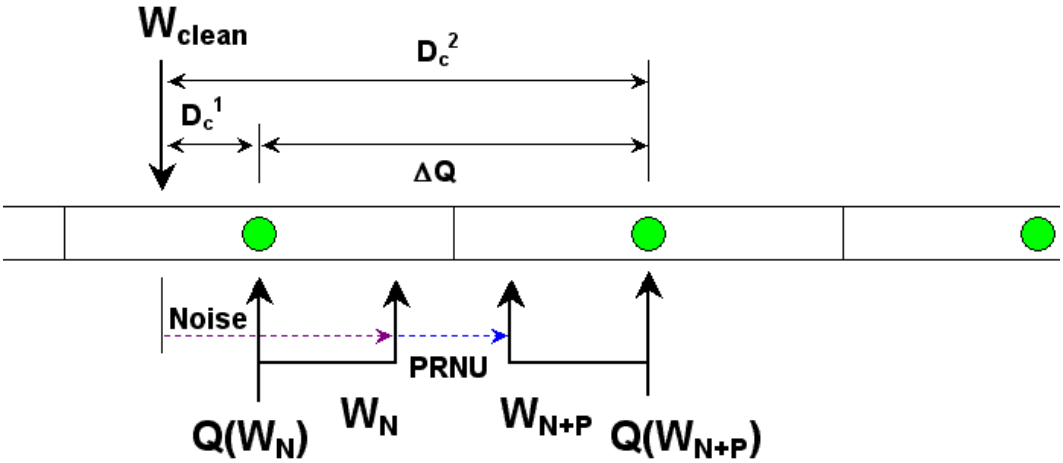

$$\Delta D = D_c^2 - D_c^1 = \Delta Q \;,\; D_c^2 > \Delta Q$$

Case 1b: W_{clean} & W_{noise} are in same bin, $W_{noise+PRNU}$ is in adjacent bin, and $D_c^2 \geq \Delta Q$

Figure 2.18: Case 1b, with $D_C^2 > \Delta Q$, PRNU forces quantized signal to next bin, and distortion is equal to quantization step size.

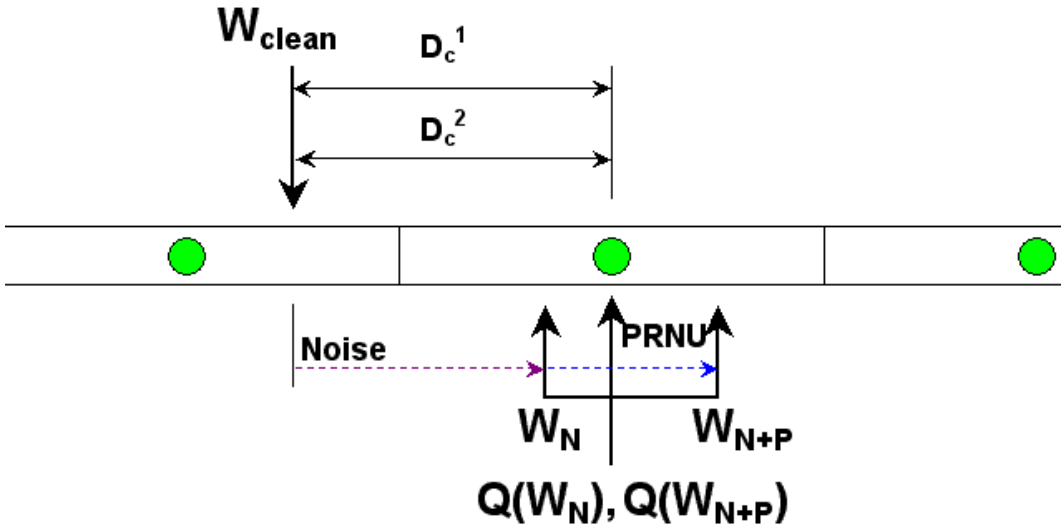

$$\Delta D = D_c^2 - D_c^1 = 0 \;,\; D_c^2 = D_c^1$$

Case 2a: W_{noise} & $W_{noise+PRNU}$ are in same bin, $D_c^1 = D_c^2$

Figure 2.19: Case 2a, $D_C^2 = D_C^1$, PRNU has no effect on quantized signal.

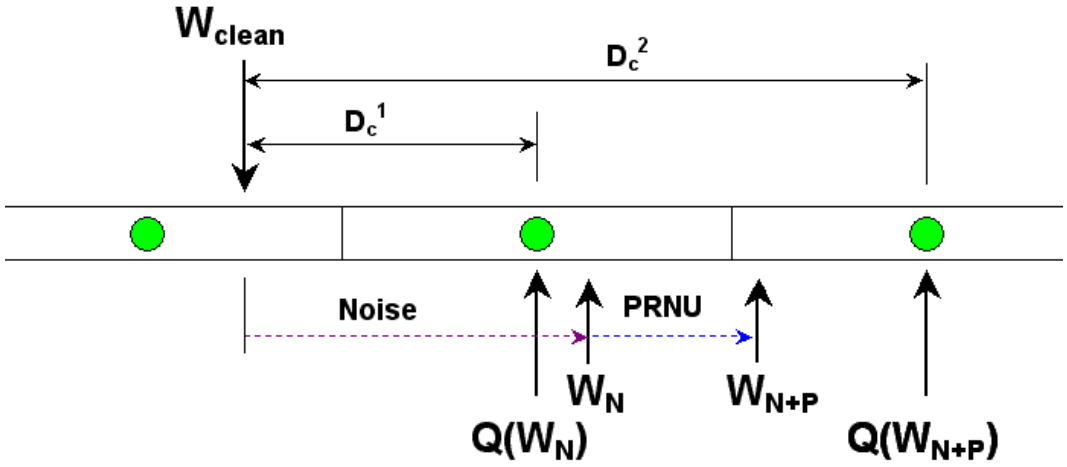

$$\Delta D = D_c^2 - D_c^1 = \Delta Q \;,\; D_c^2 = D_c^1 + \Delta Q$$

Case 2b: W_{clean} & W_{noise} & $W_{noise+PRNU}$ are all in different bins, and $D_c^2 = D_c^1 + \Delta Q$

Figure 2.20: Case 2b, $D_C^2 = D_C^1 + \Delta Q$, PRNU forces quantized signal to next bin.

Table 2.4: Distortion cases.

Bin						
Q(W)	$Q(W_{noise})$	$Q(W_{noise+PRNU})$	Case	Figure	Distortion (ΔD)	Description
A	A	A	1a	-	0	all in same bin
A	A	B	1b	2.17 2.18	$\lvert Q(W_{noise+PRNU}) - W\rvert - \lvert Q(W_{noise}) - W\rvert$	ideal with & without RN/SN/XT in one bin, PRNU in another bin
A	B	B	2a	2.19	0	ideal in one bin, both corruptions in another bin
A	B	C	2b	2.14 2.20	$\lvert Q(W_{noise+PRNU}) - W\rvert - \lvert Q(W_{noise}) - W\rvert$	all in different bins
A	B	A	2c	-	0	ideal and PRNU corruption in same bin, RN/SN/XT corruption in another bin

2.6.2 Error Rate

We determine the camera system's PRNU error rate (P_O), or probability of block error, using the D_C^1 and D_C^2 distortion measurements. These distortion measurements are functions of the PRNU probability density function, the sensor noise models, the DCT quantization matrices used, the camera system image processing model, and the sensor operating conditions (electrons per DN or ISO number). The error rate is the probability that a DCT block will have at least one coefficient distortion error that exceeds the defined threshold [12], [13]. Acceptability will then be defined as the percentage of blocks that have errors that can be tolerated. We note that global averaging metrics, such as MSE, are not suitable for measuring or detecting PRNU. The number of pixels per DCT block (or analysis block size) that have pixel PRNU values that exceed threshold allowable values can vary. Some blocks may have no defect PRNU pixels, while other blocks may have many. A global averaging metric would not provide meaningful results for this situation.

In deriving an equation for the error rate, P_O, we apply the applicable approximations and assumptions listed in Section 2.3.1.1 for the noise and image signals. As an example of how probabilities of error can be derived, consider case 1b of Table 2.4, where we can write our distortion metric (for a particular DCT frequency component of a DCT block) as:

$$\Delta D = | Q(W_{noise+PRNU}) - W | \; - \; | Q(W_{noise}) - W | \,,$$
$$\Delta D = | (l + 1)\,\Delta - W | \; - \; | l\,\Delta - W | \,, \qquad (2.17)$$

In Equation (2.17), $Q(W_{noise})$ and $Q(W_{noise+PRNU})$ are quantized to the centers of bins $l\,\Delta$ and $(l + 1)\,\Delta$, respectively (where l is the bin number). We shorten the notation W_{clean} (ideal image data) to W in Equation (2.17) and in the equations that follow. Case 1b is the situation where the addition of PRNU forces the quantized DCT coefficient to the next bin (see Figures 2.17 and 2.18).

In general, the error rate, P_O, can be defined as the probability of the distortion exceeding the threshold given a particular given PRNU pixel error and distribution (e_{PRNU} and $f_{e_{PRNU}}()$), integrated over the PRNU probability density function:

$$P_O(u,v) = \int_{e_{PRNU}} f_{e_{PRNU}}(e_{PRNU})\; P(\Delta D > Th \mid E_{PRNU} = e_{PRNU})\; de_{PRNU} \qquad (2.18)$$

The fixed value of e_{PRNU} in the above equation is the known PRNU metric, which can be determined from industry conventional measurements. Again, the above error rate equation is applied in the DCT frequency component domain, thus the value of P_O, pixel errors and distribution are all for a particular (u,v). We will not explicitly write the (u,v) term in the rate equations which are developed here, but instead assume that it is

implied. In order to find the error rate, P_O, we need to determine the conditional probability, $P(\Delta D > Th \mid E_{PRNU} = e_{PRNU})$, which can be written as:

$$P(\Delta D > Th \mid E_{PRNU} = e_{PRNU}) =$$
$$P(\mid Q[\, K\{H(G + E_{SN}) + E_{RN} + E_{PRNU}\}\,] - K'\{G\} \mid -$$
$$\mid Q[\, K\{H(G + E_{SN}) + E_{RN}\}\,] - K'\{G\} \mid > Th \mid E_{PRNU} = e_{PRNU}\,) \qquad (2.19)$$

Deriving a solution to the equation for error rate is complicated by the interaction of the raw input image (**G**) statistics, the multiple sources of noise (E_{SN}, E_{RN}, etc.), the cross talk blurring (H()), the system image processing (K{}), and the quantization (Q()). The raw input image signal **G** is shown in Figure 2.13. In Equation (2.19), K{} and K'{} are the nominal and linear system image processing operations with and without cross-talk correction, respectively. In our analysis, we restrict ourselves to the linear operations (see Section 2.3.1.1 for assumptions). The threshold, *Th*, will be a function of the system noise (E_{SN}, E_{RN}) and quantization levels (Q()), as well as the HVS factors (see Section 2.5). A Monte Carlo solution to the rate error problem is developed next (Section 2.6.2.1), along with a probability model-based simulation solution (Section 2.6.2.2).

2.6.2.1 Monte Carlo Simulation Solution

Monte Carlo methods are a class of computational algorithms that use repeated random sampling to compute results. In this method, we use characterization based pixel and camera system models. This method avoids having to use assumed or captured probability density functions (pdfs) for **W**, **G**, or **F** (image information) and the noise sources (which we will use in our probability model-based simulation solution). Instead, typical test images are used to create many 8x8 DCT blocks for use in the analysis. The

noise signals are determined based on the image signals and the noise and sensor models. We can select a set of images that will span a particular camera's application space. The images can be selected to have a range of pixel input signal magnitude, spatial frequency content, color saturation, critical color types (e.g., skin tones) and so forth. Performing the Monte Carlo simulations is simplified by our *a priori* knowledge of the noise and image-processing models. The range of sensor and camera parameters, such as sensor gain setting, exposure time, and compression rates, can then be easily exercised. We determine the error rate directly from the statistics of the output of our camera system model. This differs from the simulation solution of Section 2.6.2.2, since we do not use *a priori* noise and image signal probability distributions taken at the output of the camera system. Instead, we indirectly calculate these distributions by using our selected set of input images along with our models. We will develop a diagram representing the Monte Carlo testing methodology in Section 2.6.3.1.

2.6.2.2 Probability Model-Based Simulation Solution

We can use our sensor and system models to create DCT block-wise models to use in a probability model-based simulation method to solve the error rate problem. Probability density functions must be used for the input image (**G**) and noise sources ($\mathbf{E}_{SN}$, $\mathbf{E}_{RN}$, $\mathbf{E}_{PRNU}$). In general, the total error of a pixel DCT frequency component (u,v) can be written as [12]:

$$e = L\Delta + e', \tag{2.20}$$

where L is $\lfloor E/\Delta \rfloor$ a non-negative integer, $\Delta > e' \geq 0$, and E is the total noise value (e is a particular value of E). L defines the number of quantization bins (of size $\Delta = \Delta Q$) the

corrupted signal is from the ideal signal, and e' is the error distance within a quantization bin. This is depicted in Figure 2.21.

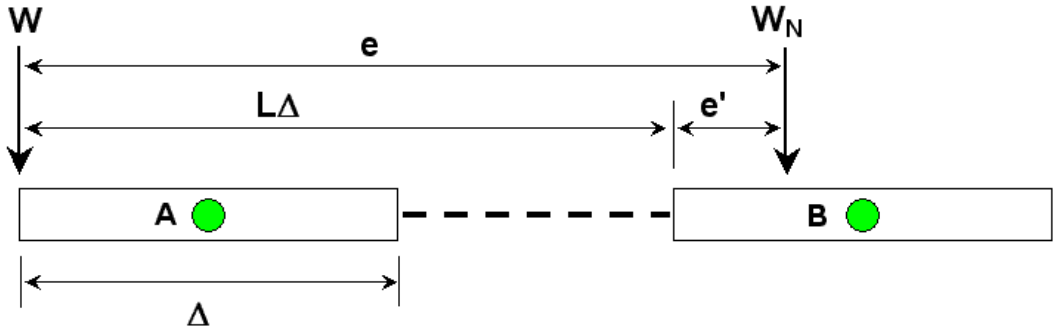

Figure 2.21: Depiction of the pixel error components: LΔ and e'.

Since we have multiple sources of error, we can write:

$$e = L'\Delta + e'_N + e'_{PRNU}, \tag{2.21}$$

where $L' = \lfloor (E_N + E_{PRNU})/\Delta \rfloor$ is due to all of the noise sources, with E_N and e'_N being all non-PRNU noise sources (shot noise, read noise, etc.). As was done in [12], we can first consider the case where L'=0, so that:

$$e = e'_N + e'_{PRNU}. \tag{2.22}$$

Here we note that e'_N and e'_{PRNU} are the errors from the ideal image signal component (G or W_{clean}) after the image processing (K{}), as well as the e'_{SN} component of e'_N including the cross-talk corruption noise (H()). Also, due to the transform within K{}, these errors are in the frequency domain (DCT), and represent a particular frequency component value (*u,v*). Again, from Section 2.3.1.1, K{} is a linear operation. Thus, using our known models for the cross-talk corruption and the image system processing, we define the following noise terms:

$$E'_N = K\{ H(E_{SN}) + E_{RN} \} \text{ , and}$$

$$E'_{PRNU} = K\{ E_{PRNU} \} . \quad (2.23)$$

We also define:

$$W = W_{clean} = K\{G\} \quad (2.24)$$

We then write the error rate for given PRNU and non-PRNU noise values (e_{PRNU} and e_N) as given by:

$$P(\Delta D(u,v) > Th(u,v) \mid E'_{PRNU} = e'_{PRNU,} E'_N = e'_N) =$$
$$P(\mid Q[W(u,v) + E'_N + E'_{PRNU}] - W(u,v) \mid -$$
$$\mid Q[W(u,v) + E'_N] - W(u,v) \mid > Th(u,v) \mid E'_{PRNU} = e'_{PRNU,} E'_N = e'_N) , \quad (2.25)$$

where, as stated previously, the e' and E' terms are frequency components (u,v). We can use our known system and noise models to determine the probability density functions for E'_N and E'_{PRNU}. We define an interval of $W(u,v)$ that results in a distortion exceeding the defined threshold as $\mathbf{B}_i$. The union of these sets, $U\mathbf{B}_i$, defines all of the values of $W(u,v)$ that have excessive distortion:

$$U\mathbf{B}_i = \{ \forall W(u,v) : \Delta D(u,v) > Th(u,v) \} \quad (2.26)$$

This set of intervals of $W(u,v)$ will be different for each of the cases of Table 2.4.

Using the equation for the conditional probability of failure (distortion greater than threshold) for particular PRNU error and non-PRNU error pdf values ($e'_{PRNU}=\sigma_{PRNU}$, $e'_N=\sigma_N$, for Gaussian behavior) above, and the determined set of intervals of W that will result in unacceptable distortion ($U\mathbf{B}_i$), we can write the error rate as:

$$P_O(u,v) = \int_{e_{PRNU}} \int_{e_N} \int_{UB_i} f_{e'_{PRNU}}(e'_{PRNU})\, f_{e'_N}(e'_N)\, f_W(W,u,v)\, dW\, de_N\, de_{PRNU} \quad (2.27)$$

The probability density functions for e'_N and e'_{PRNU} ($f_{e'_{PRNU}}(e'_{PRNU})$, $f_{e'_N}(e'_N)$), as has been stated, are determined from characterization data and system models. The probability density function of the input image ($f_W(W)$) can be determined from captured image statistical data for each DCT frequency component (u,v), and is written as $f_W(W,u,v)$ in Equation (2.27). The two noise probability density functions are dependent upon W, since they are functions of signal magnitude. However, the problem is deterministic, since we are using captured signal statistical data for $f_W(W)$ We will develop $f_{e'_{PRNU}}(e'_{PRNU})$ and $f_{e'_N}(e'_N)$, for each DCT frequency component (u,v), using the same underlying $f_W(W)$ data.

We must now determine the set of intervals $U\mathbf{B}_i$ to use in the error rate equation. As we have previously shown, only cases 1b and 2b of Table 2.4 will have non-zero distortion measurements. Case 1b can be broken into two sub-cases: $D_C^2 < \Delta Q$ (see Figure 2.17) and $D_C^2 > \Delta Q$ (see Figure 2.18). We will see that the magnitude of the noise term e'_N relative to half the DCT frequency component quantization step size, $\Delta Q/2$, will also have an effect on $\mathbf{B}_i$. We examine each of these situations in detail next. The intervals of values of W that result in unacceptable distortion are summarized in Table 2.5.

Table 2.5: Set of intervals of values of W that result in unacceptable distortion (UB_i) (case 2b is derived from case 1b with L changed from 0 to 1).

Case #	**Condition**	**UB_i**
1b – 1	$D_C^2<\Delta Q$	$W \mid i\Delta Q + \Delta Q/2 - (e'_N + e'_{PRNU}) \le W < i\Delta Q + \Delta Q/2 - Th/2$, for $0<Th\le 2(e'_N + e'_{PRNU}) \le \Delta Q$
1b – 2a	$D_C^2>\Delta Q$ & $e'_N < \Delta Q/2$	$W \mid i\Delta Q + \Delta Q/2 - (e'_N + e'_{PRNU}) \le W < i\Delta Q + \Delta Q/2 - Th/2$, for $0<Th\le \Delta Q$
1b – 2b	$D_C^2>\Delta Q$ & $e'_N > \Delta Q/2$	$W \mid i\Delta Q + \Delta Q/2 - (e'_N + e'_{PRNU}) \le W < i\Delta Q + \Delta Q/2 - e'_N$, for $0<Th\le \Delta Q$

2.6.2.2.1 B_i for case 1b with $D_C^2<\Delta Q$

In Figure 2.22 we show the relationship between the distortion ΔD and the ideal image signal data W (or K'{G}) for particular values of e'_N and e'_{PRNU} for case 1b with $D_C^2<\Delta Q$ (and L=0). As previously discussed, the noise probability density functions are deterministic. The values of e'_N and e'_{PRNU} are fixed based upon the value of W and the camera operational settings. The x-axis of the plot shows the value of the uncorrupted input signal W, along with quantization bins of size ΔQ. The y-axis shows the distortion metric value when the effects of e'_N and e'_{PRNU} and considered. A threshold value (*Th*) is shown on the y-axis, which is calculated from the methodology discussed in Section 2.5.

From Figure 2.22, we see that the maximum distortion (E_{max}) occurs when W has the value that corresponds to $W_{noise+PRNU}$ just entering the next quantization bin:

when: $W_{noise+PRNU} = W + e'_N + e'_{PRNU} = i\Delta Q + \Delta Q/2$, and

$W = i\Delta Q + \Delta Q/2 - (e'_N + e'_{PRNU})$,

we have:

$\Delta D = |Q(W_{noise+PRNU}) - W| - |Q(W_{noise}) - W)|$, so that

$\Delta D = (\Delta Q/2 + e'_N + e'_{PRNU}) - (\Delta Q/2 - e'_N - e'_{PRNU})$,

$\Delta D = 2\,(e'_N + e'_{PRNU}) = E_{max}$ (2.28)

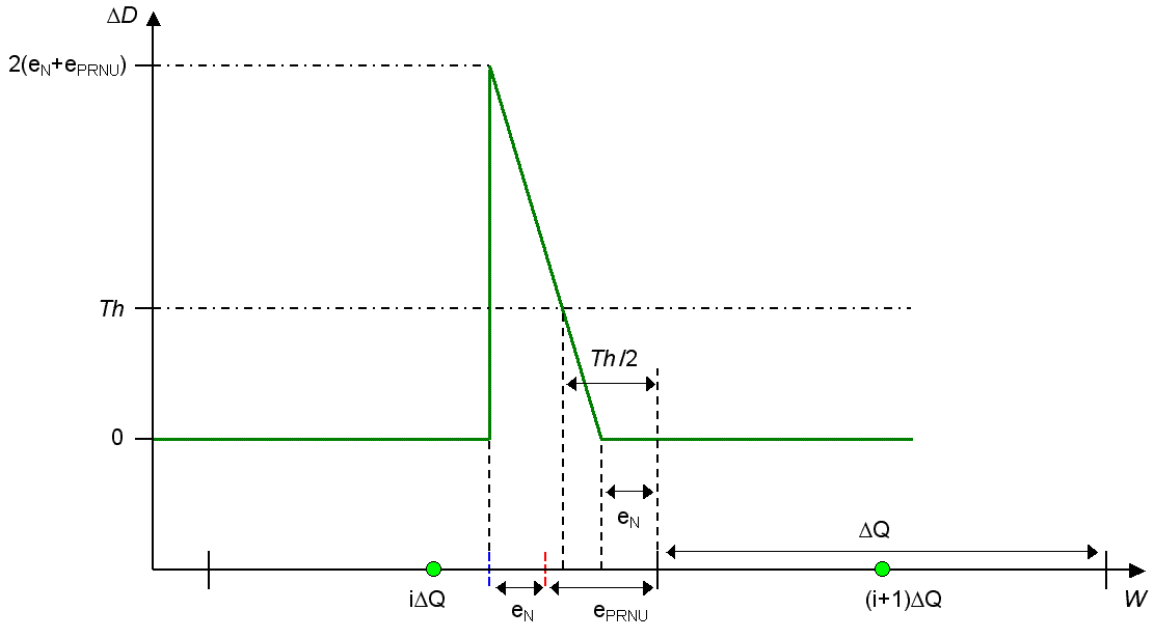

Case 1b with $D_c^2 \le \Delta Q$ (L=0) , $e_N + e_{PRNU} \le \Delta Q/2$

$B_i = \{ W \mid i\Delta Q + \Delta Q/2 - (e'_N + e'_{PRNU}) \le W < i\Delta Q + \Delta Q/2 - Th/2 \}$,
for $0 < Th \le 2(e'_N + e'_{PRNU}) \le \Delta Q$

Figure 2.22: Relationship between distortion, ΔD, and clean input image signal value, W, for Case 1b, with $D_C^2 < \Delta Q$, L=0. The region of the input signal values where the threshold is exceeded ($\Delta D > Th$) is defined by $\mathbf{B}_i$.

The maximum distortion value of $E_{max} = 2(e'_N + e'_{PRNU})$ will have a maximum value of ΔQ when $W = i\Delta Q + \Delta Q/2$ ($D_C^2 = \Delta Q$, $D_C^1 = 0$). The distortion then decreases with increasing W until it reaches zero when W_{noise} just enters the next quantization bin:

when: $W_{noise} = W + e'_N = i\Delta + \Delta Q/2$, and

$W = i\Delta Q + \Delta Q/2 - e'_N$,

we have:

$\Delta D = |Q(W_{noise+PRNU}) - W| - |Q(W_{noise}) - W)|$, so that

$\Delta D = (\Delta Q/2 + e'_N) - (\Delta Q/2 + e'_N)$,

$\Delta D = 0$ (2.29)

The distortion will have a value equaling the threshold, *Th*, when:

$$\Delta D = Th = |Q(W_{noise+PRNU}) - W_{Th}| - |Q(W_{noise}) - W_{Th})| ,$$
$$Th = (\Delta Q/2 + e'_N + x) - (\Delta Q/2 - e'_N - x), \text{ where } 0 < x < e'_{PRNU} ,$$
$$Th = 2\,(e'_N + x) , \text{ and then:}$$
$$W_{Th} = i\Delta Q + \Delta Q/2 - (e'_N + x) ,$$
$$W_{Th} = i\Delta Q + \Delta Q/2 - Th/2 \qquad (2.30)$$

The distortion will have a value equaling the threshold, *Th*, when:

$$\Delta D = Th = |Q(W_{noise+PRNU}) - W_{Th}| - |Q(W_{noise}) - W_{Th})| ,$$
$$Th = (\Delta Q/2 + e'_N + x) - (\Delta Q/2 - e'_N - x), \text{ where } 0 < x < e'_{PRNU} ,$$
$$Th = 2\,(e'_N + x) , \text{ and then}$$
$$W_{Th} = i\Delta Q + \Delta Q/2 - (e'_N + x) ,$$
$$W_{Th} = i\Delta Q + \Delta Q/2 - Th/2 \qquad (2.31)$$

A simple check of the distortion at $W=W_{Th}$ shows that this is correct:

$$\Delta D = (\Delta Q/2 + Th/2) - (\Delta Q/2 - Th/2) = Th$$

The range of W values in each quantization bin in which the distortion is unacceptable, where the input signal values produce distortions that exceed the threshold ($\Delta D > Th$), for case 1b with $D_C^2 < \Delta Q$ is then given by:

$$\boldsymbol{B}_i = \{\, W \mid i\Delta Q + \Delta Q/2 - (e'_N + e'_{PRNU}) \le W < i\Delta Q + \Delta Q/2 - Th/2 \,\},$$
$$\text{for } 0 < Th \le 2(e'_N + e'_{PRNU}) \le \Delta Q \qquad (2.32)$$

If $Th > 2(e'_N + e'_{PRNU})$, then $\mathbf{B}_i$ is empty for L=0 and $P_O = 0$. In this case if $Th > \Delta Q$, we calculate $\mathbf{B}_i$ for L=1 with $\Delta Q < Th \le 2\Delta Q$. If $Th > 2\Delta Q$, then we calculate $\mathbf{B}_i$ for L=2. If $Th > 3\Delta Q$, then we calculate $\mathbf{B}_i$ for L=3, and so forth for increasing *Th* and L values. When the value of the threshold *Th* does not exceed the minimum distortion value for a given L value:

$$\Delta D_{min} = L\Delta Q > Th\ , \qquad (2.33)$$

then the error rate is 100% (P_O = 1). For simplicity, we have omitted the frequency component terms (u,v) in the equations.

2.6.2.2.2 B_i for case 1b with $D_C^2 > \Delta Q$

In Figure 2.23 we show the relationship between the distortion ΔD and the ideal image signal data W for case 1b with $D_C^2 > \Delta Q$ (and L=0). In this case, W is on the opposite side of the quantization point (iΔQ) from W_{noise} and $W_{noise+PRNU}$.

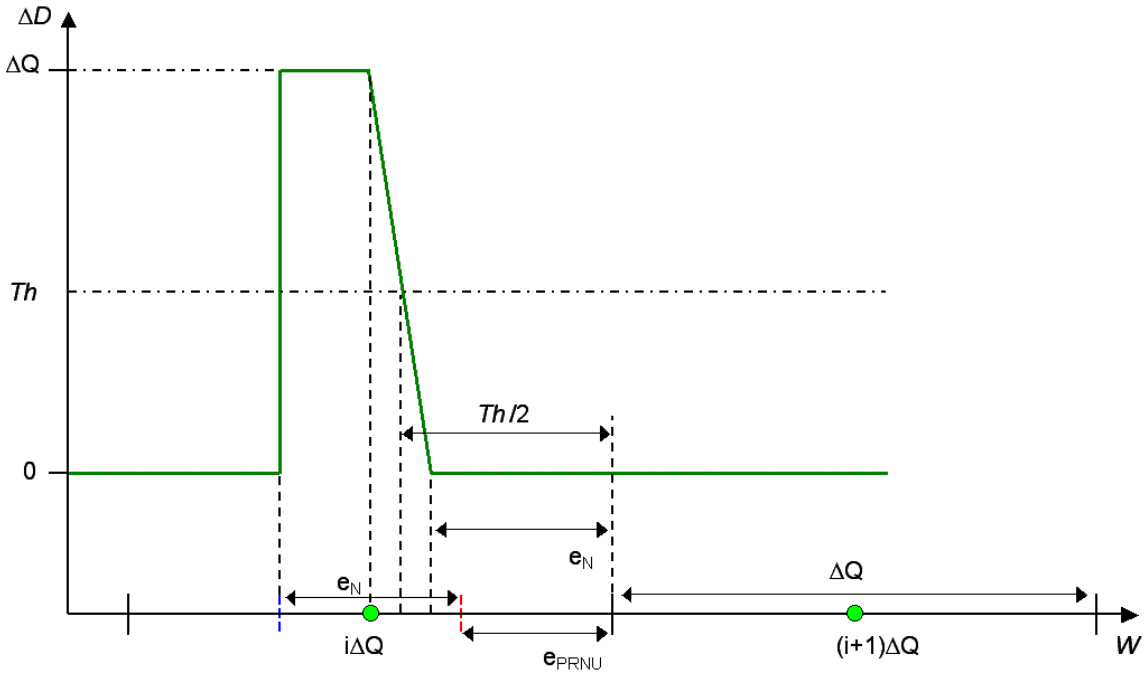

Case 1b with $D_c^2 > \Delta Q$ (L=0) , $\Delta Q/2 < e_N + e_{PRNU} \le \Delta Q$, $e_N < \Delta Q/2$

$B_i = \{ W \mid i\Delta Q + \Delta Q/2 - (e'_N + e'_{PRNU}) \le W < i\Delta Q + \Delta Q/2 - Th/2 \}$,
for $0 < Th \le \Delta Q$

Figure 2.23: Relationship between distortion, ΔD, and clean input image signal value, W, for Case 1b, with $D_C^2 > \Delta Q$ and $e'_N < \Delta Q/2$, L=0. The region of the input signal values where the threshold is exceeded ($\Delta D > Th$) is defined by $\mathbf{B}_i$.

From the figure, we see that the maximum distortion of $E_{max} = \Delta Q$ ($\Delta Q=2(e'_N+e'_{PRNU})$) occurs when W has the value that corresponds to $W_{noise+PRNU}$ just entering the next quantization bin (as with the previous case):

At $W_{noise+PRNU} = W + e'_N + e'_{PRNU} = i\Delta Q + \Delta Q/2$, and
$W = i\Delta Q + \Delta Q/2 - (e'_N + e'_{PRNU})$, and we have
$\Delta D = |Q(W_{noise+PRNU}) - W| - |Q(W_{noise}) - W)|$
$\Delta D = (\Delta Q/2 + e'_N + e'_{PRNU}) - (\Delta Q/2 - e'_N - e'_{PRNU})$
$\Delta D = 2\,(e'_N + e'_{PRNU}) = \Delta Q$ (2.34)

The range of W values in each quantization bin for which the distortion is unacceptable ($\Delta D > Th$) is dependent upon e'_N, and is examined next.

2.6.2.2.2.1 B_i for case 1b with $D_C^2 > \Delta Q$ and $e'_N < \Delta Q/2$

If e'_N is less than $\Delta Q/2$, the distortion remains constant at ΔQ as W increases until it reaches the quantization mid-point location ($i\Delta Q + \Delta Q/2$). The distortion then decreases to a value of zero at a W value corresponding to W_{noise} just entering the next quantization bin (as was true for $D_C^2 < \Delta Q$):

$W = i\Delta Q + \Delta Q/2 - e'_N$, and $e'_N < \Delta Q/2$, we have
$\Delta D = 0$ (2.35)

The point at which the distortion matches the threshold value is the same as in the $D_C^2 < \Delta Q$ case:

$\Delta D = Th = |Q(W_{noise+PRNU}) - W_{Th}| - |Q(W_{noise}) - W_{Th})|$, and $e'_N < \Delta Q/2$, for
$W_{Th} = i\Delta Q + \Delta Q/2 - Th/2$ (case 1b, $D_C^2 > \Delta Q$ and $e'_N < \Delta Q/2$) (2.36)

This gives us the same range of W values in each quantization bin for which distortion is unacceptable, where input signal values produce distortions that exceed the threshold ($\Delta D > Th$), for case 1b with $D_C^2 > \Delta Q$ and $e'_N < \Delta Q/2$ as for the case 1b with $D_C^2 < \Delta Q$:

$$\boldsymbol{B}_i = \{ W \mid i\Delta Q + \Delta Q/2 - (e'_N + e'_{PRNU}) \le W < i\Delta Q + \Delta Q/2 - Th/2 \},$$
for $0 < Th \le \Delta Q$ (which is different from the previous case). (2.37)

If $Th > \Delta Q$, then $\mathbf{B}_i$ is empty for L=0. In this case we calculate $\mathbf{B}_i$ for L=1. If $Th > 2\Delta Q$, then we calculate $\mathbf{B}_i$ for L=2, and so forth.

2.6.2.2.2.2 B_i for case 1b with $D_C^2 > \Delta Q$ and $e'_N > \Delta Q/2$

If e'_N is greater than $\Delta Q/2$, as shown in Figure 2.24, the distortion remains constant at ΔQ as W increases (from the value of $i\Delta Q + \Delta Q/2 - (e'_N + e'_{PRNU})$ shown in Section 2.6.2.2.2) until it reaches the value of $i\Delta Q + \Delta Q/2 - e'_N$. At which point W_{noise} just enters the next quantization bin, and the distortion becomes instantaneously zero:

$W = i\Delta Q + \Delta Q/2 - e'_N$ *and* $e'_N > \Delta Q/2$, we have
$\Delta D = 0$ (2.38)

This gives us a different range of W values in each quantization bin which the distortion is unacceptable, where the input signal values produce distortions that exceed the threshold ($\Delta D > Th$), for case 1b with $D_C^2 > \Delta Q$ and $e'_N > \Delta Q/2$:

$$\boldsymbol{B}_i = \{ W \mid i\Delta Q + \Delta Q/2 - (e'_N + e'_{PRNU}) \le W < i\Delta Q + \Delta Q/2 - e'_N \},$$
for $0 < Th \le \Delta Q$ (2.39)

Again, if *Th*>ΔQ, then $\mathbf{B}_i$ is empty for L=0. In this case we calculate $\mathbf{B}_i$ for L=1. If *Th*>2ΔQ, then we calculate $\mathbf{B}_i$ for L=2, and so forth.

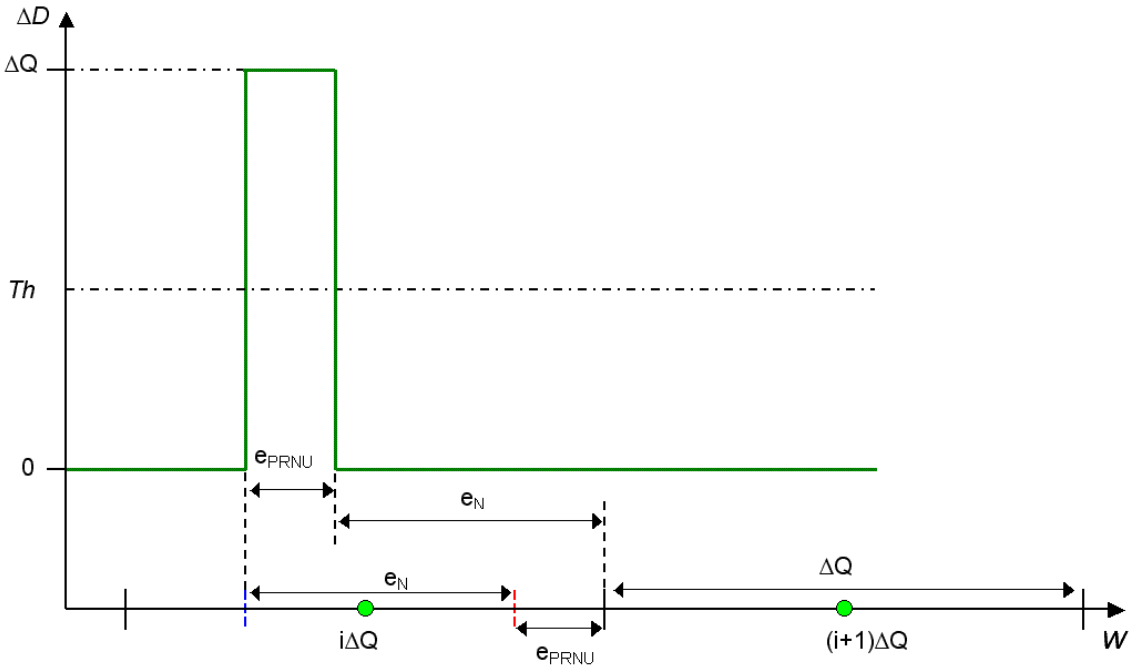

Case 1b with $D_c^2 > \Delta Q$ (L=0) , $\Delta Q/2 < e_N + e_{PRNU} \leq \Delta Q$, $e_N > \Delta Q/2$

$B_i = \{ W \mid i\Delta Q + \Delta Q/2 - (e'_N + e'_{PRNU}) \leq W < i\Delta Q + \Delta Q/2 - e'_N \}$,
for $0 < Th \leq \Delta Q$

Figure 2.24: Relationship between distortion, ΔD, and clean input image signal value, W, for Case 1b, with D_C^2>ΔQ and e'_N>ΔQ/2, L=0. The region of the input signal values where the threshold is exceeded (ΔD>*Th*) is defined by $\mathbf{B}_i$.

2.6.2.2.3 B_i for case 2b

The case 2b situation will be similar to the case 1b situation with L=1 and 0<*Th*≤2ΔQ. We will have the same three situations of distortion variation with W as we saw with case 2b, depending on the position of W relative to the mid-bin point when $W_{noise+PRNU}$ just enters a bin. For case 2b, $W_{noise+PRNU}$ is two bins removed from W, and W_{noise} is one bin removed (giving us L=1). In Figure 2.25 we show the part of the distortion plot for case 2b with D_C^2>ΔQ when L=0 and 0<*Th*≤ΔQ.

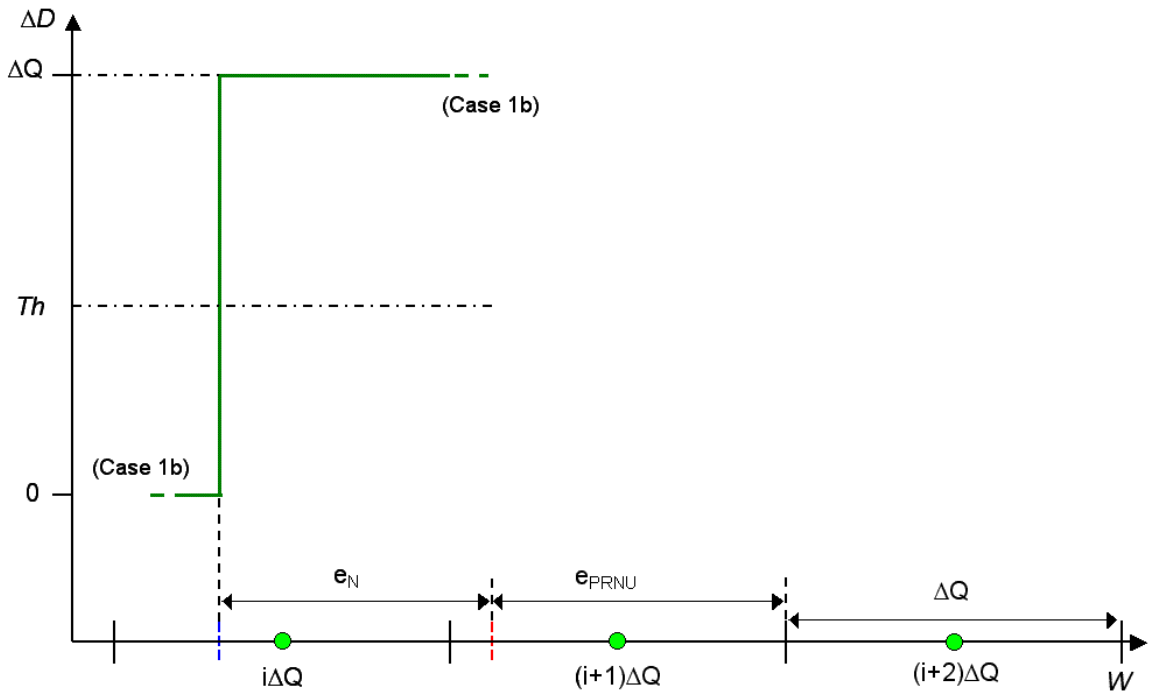

Case 2b with $D_c^2 > \Delta Q$, $0 \leq Th \leq \Delta Q$ (L=0)

Figure 2.25: Relationship between distortion, ΔD, and clean input image signal value, W, for Case 2b, with $D_C^2 > \Delta Q$ and $0 < Th \leq \Delta Q$, L=0.

2.6.2.2.4 Global error rate equation

With the range of W for unacceptable distortion ($\mathbf{B}_i$) determined, we are now in a position to solve the integral equation for the error rate, P_O. However, we still need to provide a threshold and the probability density functions (pdf) for the input image signal (W) and the noise signals that have been operated on by the system (e'_N and e'_{PRNU}). We will use statistical information based on appropriately selected test images and the use of our pixel and imager system models in order to determine $f_W(W)$, $f_{e_N}(e_N)$, and $f_{e_{PRNU}}(e_{PRNU})$. The threshold value itself will be a function of these probability density functions as well as the image system model (image processing and quantization levels). The derived error rate equation allows us to calculate $P_O(u,v)$ for frequency component (u,v). We must test each frequency component of a block (64 components

per block). As was done in [12], we must combine the individual values $P_O(u,v)$ into a global P_O using the summation law:

$$P_O = 1 - \prod_{u=1}^{N} \prod_{v=1}^{N} \{1 - P_O(u,v)\} \tag{2.40}$$

This equation can then be used in the simulation of error rate calculation using known signal and noise statistical models. The simulation can be used to yield a mapping from $f_{e'_{PRNU}}(e'_{PRNU})$ to error rate, and will only have to be performed a handful of times per sensor design. Thus, overall complexity is not a major concern. However, some computation complexity and time can be saved by assuming, as was done in [12], that $P_O(u,v)$ will be small for all of the frequency components (u,v), so that we can use the approximation:

$$P_O \approx \sum_{u=1}^{N} \sum_{v=1}^{N} P_O(u,v) \tag{2.41}$$

2.6.3 PRNU Distortion Testing Methodology

Two different sensor PRNU testing methodologies, a Monte Carlo simulation solution and a probability model-based simulation solution, will now be developed and discussed. Both of these methodologies will permit sensors to be tested for different applications. We will be able to take advantage of a sensor application having a certain set of magnitudes of quantization and ISO operating conditions. This will allow us to select sensors for different applications using the performance in our proposed PRNU screening methods. These methods permit us to choose operating conditions and

quantization levels to mask the perceptual effects of the corresponding PRNU. We will also show how these two methodologies result in solutions that are almost identical.

2.6.3.1 PRNU Distortion Monte Carlo Testing Methodology

We can now state a methodology for PRNU distortion testing using a Monte Carlo approach. The distortion measurements D_C^1 and D_C^2 are determined for the entire image of DCT terms. Then the difference measurements in these distortions are calculated, yielding our error significance metrics (ΔD). This is the perceptual distance between $Q(W_{noise})$ and $Q(W_{noise+PRNU})$, similar to that defined in [13]. Each 8x8 DCT pixel block of the sensor is then tested to determine if any of its 64 coefficients exceed the visibility thresholds ($Th(u,v)$) [89], [35]. This testing is done for both the luminance and chrominance data (Y, U, V, or Y, C_r, C_b channels). The error rate (P_O), or probability of block error, is determined using these measurements as a function of the PRNU probability density function, DCT quantization matrices used, the sensor operating conditions (electrons per DN or ISO number) that affect the sensor noise models, and the camera system image processing. The definition of error rate is taken from [12] and [13], which states that it is the probability that a DCT block will have at least one coefficient error that exceeds the defined threshold. Acceptability is defined as the percentage of blocks that have errors that can be tolerated. Input PRNU pdf, $PRNU_{peak\text{-}to\text{-}peak}$, or $PRNU_{rms}$ values are then correlated to the final error rates for a prescribed set of camera operating conditions. Multiple camera operating conditions can be used, which can correspond to different camera applications. We perform this analysis using a predetermined set of test images selected based on the camera application. A diagram of the testing methodology is shown in Figure 2.26.

2.6.3.2 PRNU Distortion Model-Based Simulation Testing Methodology

We can use Equation (2.27) of Section 2.6.2.2, along with pdfs of each DCT coefficient component for the input image and camera system processed noise terms, to calculate a table of error rates based upon the input parameters of operating conditions and PRNU values (σ_{PRNU}). We modify the error rate equation to operate in the discrete (sampled) domain instead of the continuous domain (summations used instead of integrals):

$$P_O(u,v) = \sum_{\mathbf{e_{PRNU}}} \sum_{\mathbf{e_N}} \sum_{\mathbf{UBi}} pmf_{e_{PRNU}}(e_{PRNU})(u,v)pmf_{e_N}(e_N)(u,v)pmf_W(W)(u,v) \quad (2.42)$$

In using the above error rate equation, we are reminded that the set of intervals of W values in each quantization bin which the distortion is unacceptable ($U\mathbf{B}_i$) is a function of the acceptable distortion threshold ($Th(u,v)$) for each DCT frequency coefficient (u,v). Additionally, we must apply the error rate equation for the three output channels of W (one luminance and two chrominance, e.g., YUV). Standard PRNU testing is then used to measure a PRNU error metric, such as block $PRNU_{peak\text{-}to\text{-}peak}$ or σ_{PRNU}, for a set of sensors. This measured PRNU error is correlated with a camera system processed PRNU noise (e'_{PRNU}) pdf curve ($f_{e'_{PRNU}}()$). Then the error rates for each sensor can be determined for different applications based on the measured PRNU block values.

2.7 Performance Measurements and Conclusions

In our proposed PRNU testing methods, we use Monte Carlo simulations and probability model-based simulations to create plots that relate measurements of raw block PRNU

values to failure rates for particular sensor applications. The failure rate curves are constructed for specific sensor operating conditions (gain setting, exposure time, etc.) and image processing settings. Each of these settings or groups of settings can be associated with a specific sensor application. The analysis path of our proposed Monte Carlo PRNU screening method is depicted in Figure 2.26, which shows the use of our sensor and camera models. A set of application appropriate images is used as input to the Monte Carlo simulations. We used over 50,000 8x8 pixel blocks to run through the Monte Carlo PRNU screening method and to generate probability data for the probability model-based simulation method. One of the input images used is shown in Figure 2.29.

The industry standard or conventional PRNU screening threshold value for the block PRNU peak-to-peak limit is a heuristic and subjective visualization limit. In the results presented in this thesis, we have used a conventional PRNU peak-to-peak testing threshold value of 10% to define PRNU block failure. This value is fairly typical for low and mid quality consumer applications [17]. It is a simple matter to use a different threshold value in our method.

We show the PRNU failure rates for the conventional peak-to-peak method (black curve) and our two proposed methods for different sensor gain settings (conversion factors of 28, 7, and 2.8 e-/DN) in Figure 2.27. The failure rate, shown on the Y-axis, is plotted in log scale as a function of the mean block $PRNU_{rms}$ value (σ_{gain}/μ_{gain}). This mean block $PRNU_{rms}$ value can be related to a maximum block $PRNU_{P-P}$ value, as shown in Figure 2.4. As sensor gain is increased, the conversion factor (e-/DN) decreases. The so called ‘base’ or good quality compression settings were used in the calculations for Figure 2.27. The JPEG DCT quantization matrices for the base setting are shown at the

end of the section in Table 2.6. These matrices can be scaled using a 'Quant Factor' to increase compression, where the 'base' setting has 'Quant Factor'=1.

The conventional PRNU screening method is fairly independent of the sensor gain settings used. This is due to the conventional method removing temporal noise through frame averaging. In actuality, the gain setting would affect the point on the pixel response curve (see photon transfer curve of Figure 2.12) where the measurements are made. Higher gain settings would force us to the left and down the pixel response curve (Figure 2.12). But when temporal noise is removed, we should measure the same pixel response variation to mean response ratio, so the conventional screening method will have the same failure rate curve for all of these simulated gain settings. In contrast, since our proposed method uses HVS visibility of PRNU as a distortion threshold, we will see different failure rate curves for different sensor gain settings.

Our sensor model has a base gain of 28 e-/DN, which provides the lowest noise and highest SNR sensor operation. Under this operational setting, the visibility of PRNU will be the greatest. Figure 2.27 shows that at the sensor base gain setting combined with typical DCT quantization ('Quant Factor'=1), the conventional and our proposed PRNU screening methods have similar sensor block PRNU variation values at which the failure rate becomes non-zero (0.001%). This is the point at which we define the sensors as beginning to fail the PRNU screening test. This state is shown as the failure rate knee point, circled in the plot. This agreement suggests that the $PRNU_{p-p}$ threshold limit (10% used in this case, which corresponds to a block mean σ_{PRNU}=1.5% for approximately 5100 8x8 blocks) can be determined by subjective visual analysis of images taken from

the sensor operating under its best (most severe) gain setting combined with typical JPEG compression.

The conventional threshold is not finely tuned for the complete camera system, which includes consideration of the image processing pipeline, compression, and system noise. Furthermore, the conventional threshold does not vary with these camera settings. We also note that the sensitivity of the conventional PRNU screening method to the input mean block PRNU amount is greater than that of our proposed method. This can be seen by comparing the slopes of the PRNU failure rate curves of Figure 2.27. Our proposed method produces a more gradual PRNU failure rate response to changes in the mean block PRNU amount, which becomes flatter as the sensor gain setting is increased (e-/DN decreases). This flattening can be advantageous, in that slight errors in PRNU measurements become less important, and lead to smaller errors in the failure rate calculation. Our proposed PRNU failure rate curve method is less sensitive to changes in PRNU since we consider the entire camera system (total noise, compression, image processing), and not just the measured block PRNU value.

We see in Figure 2.27 that the failure rate knee point will move to the right as the sensor gain setting is increased (and e-/DN decreases). This is due to the total noise increasing and the SNR decreasing, allowing more PRNU noise. As the sensor base gain setting is increased (representing worse noise performance), the PRNU failure rate curve moves to the right. This results in a lower sensor failure rate for a given PRNU variation (standard deviation). However, at lower gain settings, we approach the point where the DCT quantization noise will be dominant. At this point, lowering the sensor gain setting will have little effect on the failure rate curve. We can see this affect in Figure 2.27 by

looking at the relatively small movement between the sensor e-/DN=7 and e-/DN=28 curves compared to the e-/DN=2.8 and e-/DN=7 curves.

In Figure 2.28, we show how the DCT quantization setting affects our proposed PRNU failure rate method. Failure rate curves are shown in Figure 2.28 for a sensor gain setting of 28 e-/DN combined with the cases of 'Quant Factor' DCT factor values of 1, 1.5, 2, and no quantization applied. The plot shows how the failure rate curves shift to higher allowable mean block PRNU values as the DCT quantization is increased. This is due to the PRNU becoming less significant to the measured distortion as the quantization noise increases. The decrease in the sensor PRNU failure rate for a given mean block PRNU value as quantization is increased is significant. This shows that for applications with higher compression and lower image data rate transmission requirements, we can reduce the PRNU rejection rate of sensors. When we do not apply DCT quantization, the failure rate knee point decreases, and the failure rate curve moves to the left. The left-most curve in Figure 2.28 shows the sensor being operated at its highest conversion gain setting combined with no compression being applied, both of which reduces the masking of PRNU. However, this mode of sensor operation is not typical for lower and middle quality consumer CMOS sensors. The conventional heuristic PRNU threshold for these types of sensors is determined with the sensor operating under some degree of compression.

From the PRNU failure rate curves, we see several basic trends:

1) As the gain setting of the sensor is increased, a greater block PRNU error can be tolerated (see Figure 2.27). This is due to the other sources of noise increasing relative to the PRNU noise. The relative contribution of PRNU to the total overall distortion is reduced, and the allowable

distortion threshold is increased. The operation range of the pixel is reduced, removing some upper response region, which is more significant for PRNU.

2) As the JPEG DCT quantization is increased, a greater block PRNU error is allowed (see Figure 2.28). Thus, for higher compression and lower image data transmission rates, more block PRNU error is tolerable. This is due to the quantization noise increasing, and masking the PRNU. At lower gain settings (low ISO, high SNR), there is little separation between the failure rate curves when DCT quantization (compression) is applied (see Figure 2.27). This is due to the non-PRNU noise values not being high enough to improve the allowable PRNU failure rate. Thus, only the DCT coefficient error visibility thresholds affect the distortion thresholds, and the ΔD distortion is mostly due to the PRNU corruption. When no DCT quantization is applied, lower gain settings will continue to produce lower failure rate curves (shifted to the left), since distortion will be almost entirely due to PRNU corruption. Often, conventional PRNU testing does not consider these more severe operating conditions for a sensor, since they do not occur during typical camera operation. Thus, the heuristic block PRNU threshold is set higher (commonly $PRNU_{P\text{-}P}$ block threshold of 10% [16]), since it assumes a minimum amount of compression will be used.

3) Though not directly shown in the plots, more severe image processing can result in less block PRNU error being tolerated. This image processing includes color correction and saturation enhancement. Other image processing, such as Bayer pattern interpolation, which may low pass filter image data, can result in more block PRNU variation being tolerated. To understand the net effect of the image processing, a complete model must be simulated. The Monte Carlo analysis used image signal probability distributions taken at the output of the camera system model. The probability model-based simulations used the image processing system model to create the DCT block-wise models.

4) The conventional 'common' allowable PRNU peak-to-peak threshold of 10% [16] for low to mid quality consumer sensors roughly corresponds to the knee in the proposed PRNU screening method failure rate curve for our sensor operating at its base gain combined with base JPEG compression (matrices values in Table 2.6) and standard image processing. This point is shown in Figure 2.27. A mean block $PRNU_{rms}$ value of 1.5% corresponds to a maximum block $PRNU_{P-P}$ value of 10% for a sensor with approximately 300K to 1M pixels. We would expect the methods to be in close agreement for the most severe and realistic operating conditions.

5) The conventional PRNU peak-to-peak failure rate method is very sensitive to the PRNU threshold parameter. This can be seen in the very steep curves of the conventional PRNU failure rate shown in Figures 2.27 and 2.28. Our proposed method produces PRNU failure rate curves that have a more gradual response to changing block PRNU values than the conventional method. This can lead to a more stable PRNU metric, which is less sensitive to errors in block PRNU measurements. This reduced sensitivity is due to consideration of the entire camera system (total noise, compression, image processing).

6) The Monte Carlo and probability model-based simulation methods produce nearly identical error rate performance results. This is due to the use of the same underlying pixel and camera models, as well as the use of the same distortion and threshold methodologies.

We can use our proposed method to create a full set of failure rate curves for a sensor family. Subsets of the curves can then be assigned to different sensor applications. We can then screen sensors using the standard method of measuring PRNU block values. These measured values then are used with the new failure rate curves to determine failure rates for the different sensor applications. This is the classification of sensors based on their PRNU performance and the requirements of specific applications. We

use the idea that different sensor applications will have different requirements on quantization (compression) amounts, acceptable SNR, image processing applied, sensor gain settings, and other operating conditions. With this methodology, the yield rate of sensors can be increased. In order to determine quantitatively the potential yield rate improvement, we need to acquire more data on industry established acceptable PRNU block thresholds and failure rates per sensor. One difficulty we find is that much of this information is company proprietary. Thus, the task of calculating the yield rate improvement from the use of our PRNU method requires further study.

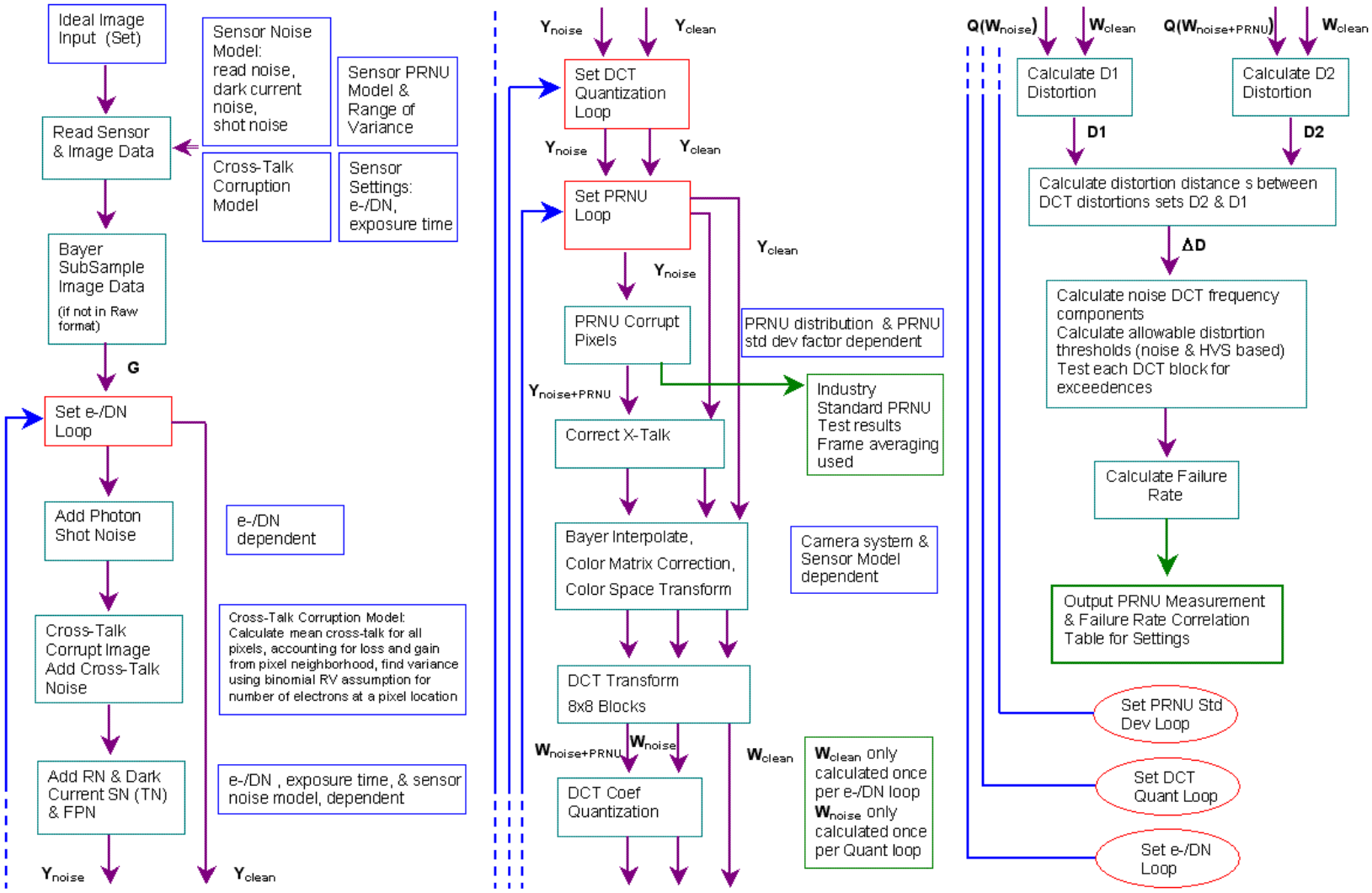

Figure 2.26: Analysis path (Flow Diagram) of proposed PRNU Monte Carlo distortion screening method.

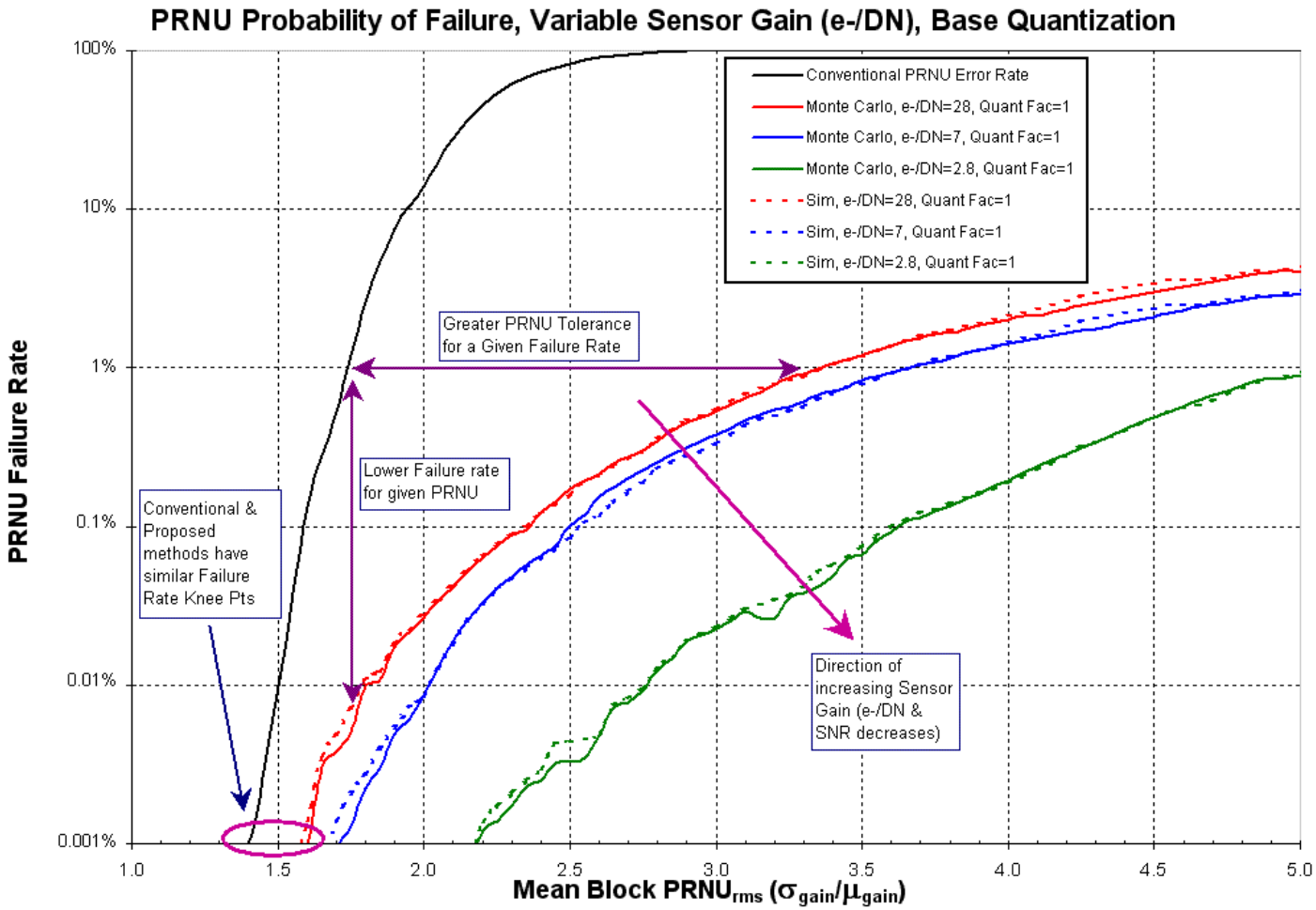

Figure 2.27: Monte Carlo and probability model-based simulation PRNU failure rate method curves for variable sensor gain at the base DCT quantization setting. Conventional PRNU failure rate curve is also shown. The 'knee' point is close to the mean block $PRNU_{rms}$ (σ_{gain}/μ_{gain}) value of 1.5, which corresponds to a maximum block $PRNU_{P\text{-}P}$ value (limit) of 10% for a sensor with approximately 300K to 1M pixels. 'Quant Factor=1' signifies that the DCT quantization matrices of Table 2.6 were applied.

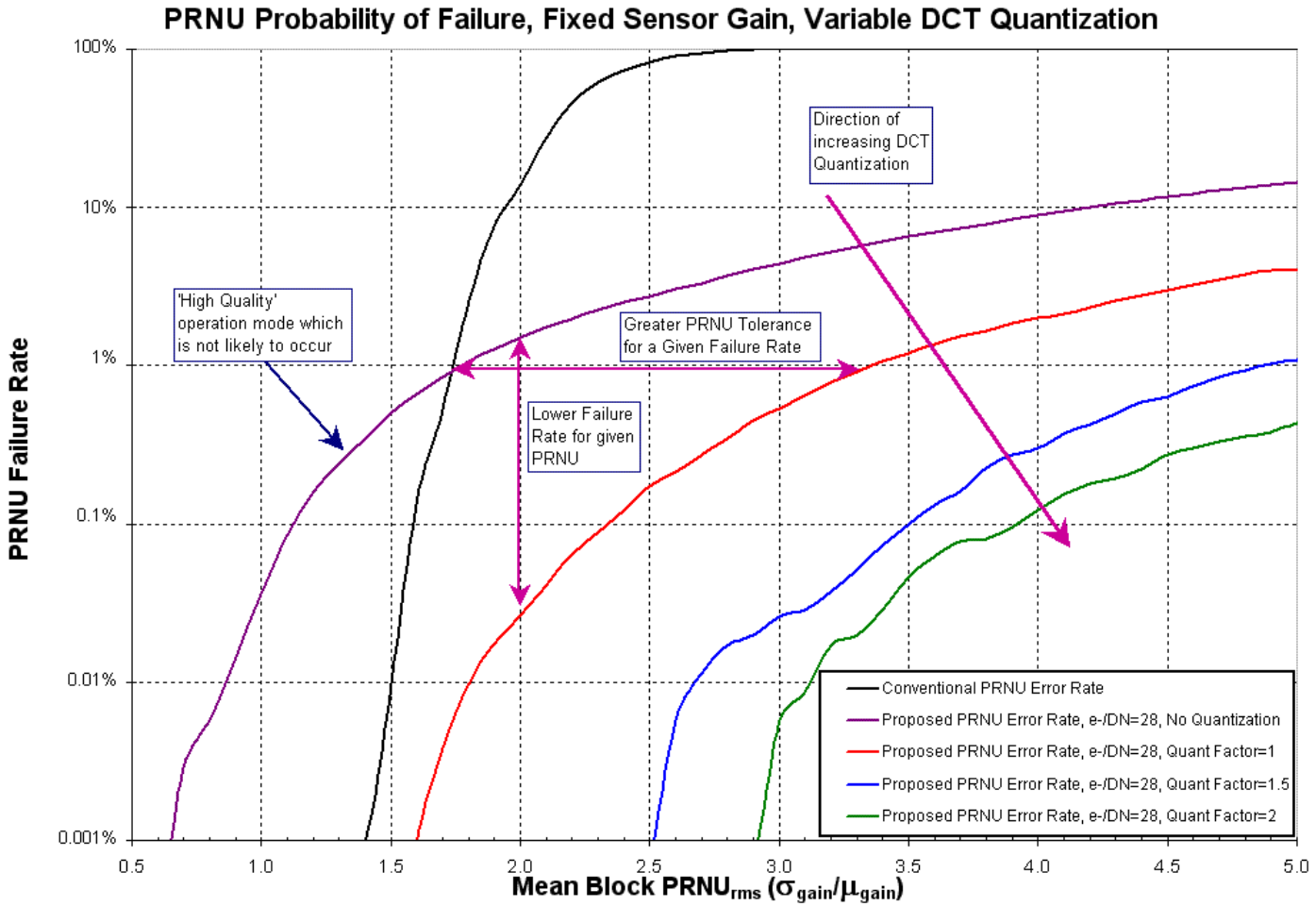

Figure 2.28: PRNU failure rate curves for sensor gain setting of e-/DN=28 (base gain) and variable with variable DCT quantization applied. 'Quant Factor' is the multiplicative terms applied to the JPEG DCT quantization matrices shown in Table 2.6. The far left curve is the case where DCT quantization was not applied and the lowest gain setting was used. This case is severe, and is not typically used for determining PRNU failure.

Figure 2.29: Sample image used or Monte Carlo PRNU screening method and to generate probability data for the probability model-based simulation method.

Table 2.6: Luminance [Y] and Chrominance [C_r & C_b] quantization matrices.

Luminance [Y] quantization matrix:

16	11	10	16	24	40	51	61
12	12	14	19	26	58	60	55
14	13	16	24	40	57	69	56
14	17	22	29	51	87	80	62
18	22	37	56	68	109	103	77
24	35	55	64	81	104	113	92
49	64	78	87	103	121	120	101
72	92	95	98	112	100	103	99

Chrominance [C_r & C_b] quantization matrix:

17	18	24	47	99	99	99	99
18	21	26	66	99	99	99	99
24	26	56	99	99	99	99	99
47	66	99	99	99	99	99	99
99	99	99	99	99	99	99	99
99	99	99	99	99	99	99	99
99	99	99	99	99	99	99	99
99	99	99	99	99	99	99	99

Chapter 3

Bayer Cross-Talk Reduction Method for Embedded Imaging Systems

3.1 Introduction

In this chapter we develop a simple multi-channel imager restoration method to correct color channel dependent cross-talk of a Bayer color filter array (CFA) sensor. In this effort, we break up each color channel into color channel components (CCC) and create separate cost functions (weakened optimization) for each CCC. Our restoration solution has its regularization parameters determined by maximizing the developed local pixel SNR estimations (HVS detection constraint), where local pixel adaptivity is applied. We utilize sensor characterization *a priori* information in our solution. The correction method is geared towards implementation into the on-chip digital logic of low-cost CMOS sensors. Thus, our solution is a direct and computationally simple technique.

The different sources of pixel cross-talk are discussed in Section 3.2.1. The general Bayer cross-talk problem which we must solve is presented in Section 3.2.2. The basic constrained least squares (CLS) problem solved by our method is presented in Section

3.2.2.1. In Section 3.2.2.2, color channel components are defined and their use in our solution is discussed. In Section 3.2.3, existing restoration methods that have been applied or could be applied to the Bayer cross-talk problem are discussed. The inadequacies of applying these methods to meet the particular requirements or constraints of our low-cost camera system are discussed in that section. The goals, requirements and constraints of our low-cost camera system Bayer cross-talk correction method are presented in Section 3.2.4. The motivation for our novel solution to the Bayer cross-talk problem is presented in Section 3.3.1. The general approach of methods that we use to address the inadequacies of existing restoration methods are developed in Section 3.3.2. In Section 3.4, we derive our deterministic separate CCC constrained least squares local SNR (SCLS SNR) method. Lastly, performance data and conclusions are presented in Section 3.5.

3.2 Bayer Cross-Talk Problem

3.2.1 Causes of Bayer Multi-Channel Blurring

Image sensor cross-talk is the loss of electrons or photons from a pixel to neighboring pixels. Pixel cross-talk degrades both image sharpness (modulation transfer function, MTF) and colorimetric accuracy (highly de-saturated, color-muted images). There are both photonic (optical) and electronic (lateral diffusion) forms of cross-talk, as shown in Figure 3.1. Photons can pass at an oblique angle through the CFA of one pixel such that they are collected by an adjacent pixel with a different color filter. After carriers have been created by photons in a photodiode, they may diffuse to the depletion region of an adjacent pixel. The depth that photons penetrate into the photodiode before creating an electron-hole pair is wavelength dependent [9]. Photons of shorter

wavelength (e.g., blue light) have greater photon energy, and excite the silicon's electrons sooner. They will not penetrate deep into the photodiode. Thus, blue pixels will experience less diffusion cross-talk loss. Photons of longer wavelength (e.g., red light) penetrate deeper into the photodiode. The carriers created by these photons are more likely to diffuse to neighboring pixels. The percentage of cross-talk will increase as the size of pixels is progressively reduced.

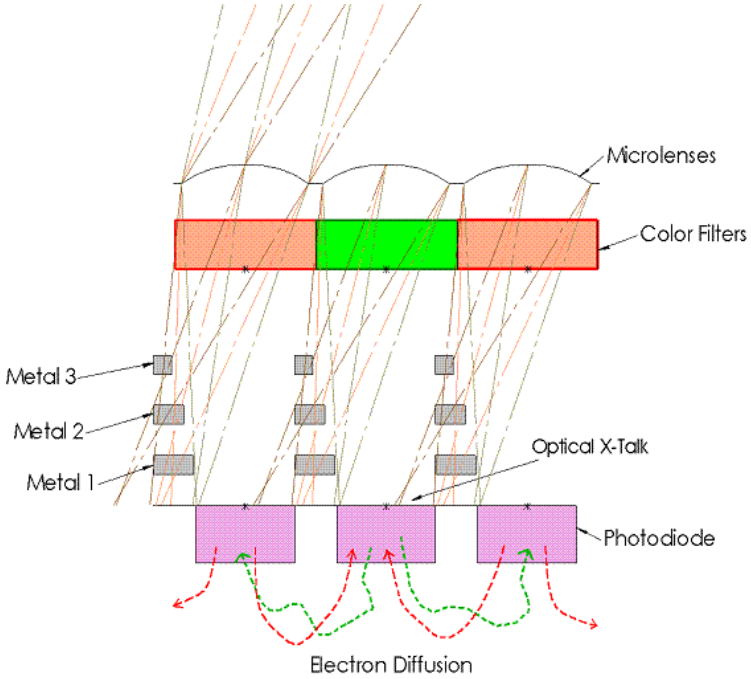

Figure 3.1: Photonic and electronic forms of pixel cross-talk.

The Bayer pattern, shown in Figure 3.2, is the most commonly used CFA for low-cost sensors. For imagers that use the Bayer CFA pattern, there will be a larger degree of cross-talk from red pixels to green pixels than other color combinations. Additionally, due to asymmetric pixel lay-outs, the amount of cross-talk signal received by green pixels on odd and even rows can be different. The color pixel type dependencies of cross-talk make it a Bayer multi-channel blurring problem. Both the optical and diffusion cross-talk can be characterized for a sensor design, and then used for its correction.

Typical values of cross-talk coefficients for a CMOS sensor with small pixels [17] are shown in Figure 3.3. From Figure 3.3, we see that the extent of the cross-talk blurring matrices is small (typically within a 5x5 pixel area).

B	GO	B	GO
GE	R	GE	R
B	GO	B	GO
GE	R	GE	R

Figure 3.2: Bayer CFA pattern (typical types: red, green-even, green-odd, blue).

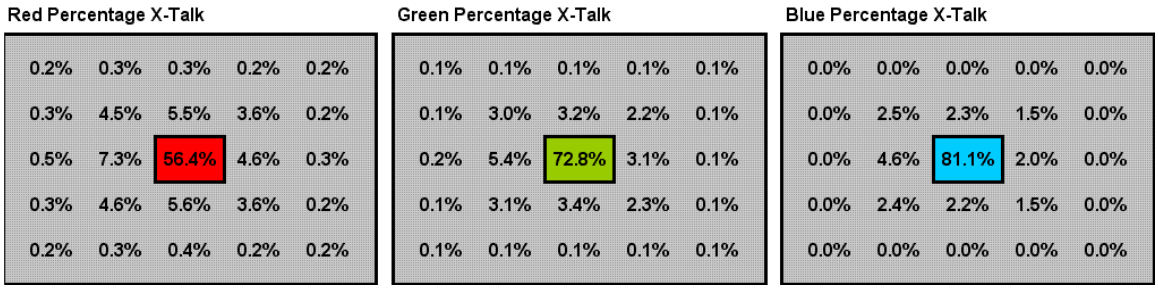

Figure 3.3: Cross-talk loss coefficients for a typical small pixel CMOS sensor [17].

3.2.2 Bayer Multi-Channel Blurring Problem Formulation

The Bayer multi-channel cross-talk problem can be viewed as a blurring restoration problem with four channels: green-odd, red, green-even, and blue (Go, R, Ge, B). We can assume without loss of generality that each of the N=4 color channels has M×M or M^2 pixels. The Bayer cross-talk blurring problem can be written in stacked vector and matrix form as:

$$\boldsymbol{y} = \boldsymbol{H}\,\boldsymbol{f} + \boldsymbol{n}\,, \tag{3.1}$$

where **y** is the $NM^2 \times 1$ observed blurred image with additive noise vector, **f** is the $NM^2 \times 1$ input (non-corrupted) image vector, **n** is the $NM^2 \times 1$ noise image vector, and **H** is the $NM^2 \times NM^2$ multi-channel blurring matrix. We can write the **y**, **f**, and **n** vectors for the Bayer color channels as:

$$\boldsymbol{y} = \begin{bmatrix} y_{Go} \\ y_R \\ y_{Ge} \\ y_B \end{bmatrix}, \qquad \boldsymbol{f} = \begin{bmatrix} f_{Go} \\ f_R \\ f_{Ge} \\ f_B \end{bmatrix}, \qquad \boldsymbol{n} = \begin{bmatrix} n_{Go} \\ n_R \\ n_{Ge} \\ n_B \end{bmatrix} \tag{3.2}$$

The Bayer CFA multi-channel blurring matrix (**H**) can be written as:

$$\boldsymbol{H} = \begin{bmatrix} H_{GoGo} & H_{RGo} & H_{GeGo} & H_{BGo} \\ H_{GoR} & H_{RR} & H_{GeR} & H_{BR} \\ H_{GoGe} & H_{RGe} & H_{GeGe} & H_{BGe} \\ H_{GoB} & H_{RB} & H_{GeB} & H_{BB} \end{bmatrix}, \tag{3.3}$$

where the full blurring matrix **H** is composed of stationary block-circulant $M^2 \times M^2$ sub matrices $\mathbf{H}_{ji}$. The sub matrices $\mathbf{H}_{ji}$ are defined as having the *j* index being the input channel and the *i* index being the output (blurred) channel. Thus, $\mathbf{H}_{RGe}$ would represent the blurring of the green-even channel due to the red channel. The assumption of a stationary block-circulant cross-talk blurring matrix is usually valid for our target camera system, as can be seen from characterization data of sensor cross-talk [17]. However, stationarity can be sometimes be invalidated by optical effects resulting from low-cost lenses and small pixels. We will not consider these optical non- stationary effects in this thesis.

Numerous multi-channel deterministic regularization methods have been developed. Many of these methods are non-linear and require iterative solutions. Other solutions

make simplifying assumptions such as neglecting the dependence between the color channels, not considering the full spatial blurring, or not being adaptive to the local noise levels. The most popular and practical restoration methods are discussed in Section 3.2.3. We employ a direct deterministic regularization estimation method, which we discuss in Section 3.2.2.1 as part of our problem formulation.

3.2.2.1 Constrained least squares solution

A widely accepted deterministic regularization method is constrained least squares (CLS) restoration [5]. CLS methods minimize a linear operator on the estimated restored image $\hat{\mathbf{f}}$ (such as $\mathbf{Q}\hat{\mathbf{f}}$) subject to some set of conditions [3]. The operator **Q** is the regularization functional, which reduces the effects of the small singular values of **H** that occur at high frequencies, while leaving the larger ones unchanged. One popular choice for the known condition is the norm of the noise signal ($||\mathbf{n}||^2$). Using this approach, along with the smoothness constraint, $||\mathbf{Q}\hat{\mathbf{f}}||^2$, the constrained optimization problem can be written as determining a solution $\hat{\mathbf{f}}$ which [27]:

minimizes: $|| \boldsymbol{Q}\hat{\boldsymbol{f}} ||^2$,

subject to the constraint: $|| \boldsymbol{y} - \boldsymbol{H}\hat{\boldsymbol{f}} ||^2 = || \boldsymbol{n} ||^2$ (3.4)

This can be solved using a Lagrangian technique, that is obtaining $\hat{\mathbf{f}}$ so as to minimize the cost function [5], [27]:

$$\phi(\hat{\boldsymbol{f}}, \beta) = (|| \boldsymbol{y} - \boldsymbol{H}\hat{\boldsymbol{f}} ||^2 - || \boldsymbol{n} ||^2) + \beta || \boldsymbol{Q}\hat{\boldsymbol{f}} ||^2 , \quad (3.5)$$

where the Lagrange multiplier, or regularization parameter, β, is adjusted in order to meet the defined constraint or set of constraints [5]. Estimates of the signal (**f**) and noise

(**n**) energy values can be used to determine β [5], [26], [27]. Iterative methods are often used in order to determine the optimal value of β [5], [27]. For our direct solution, we use sensor characterization noise models that are signal-dependent in order to calculate restored pixel SNR estimates (refer to Section 3.4.2.2). We determine the optimal regularization parameter value by maximizing the estimates of the corrected pixel SNR using an off-line search method (see Section 3.4.2.2.4):

$$\beta = \text{maximize: } || \hat{\boldsymbol{f}}^{2} / \check{\boldsymbol{n}}^{2} ||^{2} , \tag{3.6}$$

where $\hat{\mathbf{f}}$ is the estimated restored pixel value, and $\check{\mathbf{n}}$ is the estimated noise value. Our problem is further defined to operate on color channel components, as discussed in the Section 3.2.2.2. The local pixel SNR optimization is derived in Section 3.4.2.2.4.

3.2.2.2 Separation of color channel components

For the Bayer CFA (see Figure 3.2), the color channel components (CCC) are defined as being each of the four-color channels that compose each color channel. All four color channels are components of each blurred color channel. During reconstruction, each CCC is corrected. Thus, referring to Equations (3.2) and (3.3), we can write each output (observed) blurred channel *i* as:

$$\boldsymbol{y}_i = \boldsymbol{H}_{Goi}\,\boldsymbol{f}_{Go} + \boldsymbol{H}_{Ri}\,\boldsymbol{f}_{R} + \boldsymbol{H}_{Gei}\,\boldsymbol{f}_{Ge} + \boldsymbol{H}_{Bi}\,\boldsymbol{f}_{B} \text{ , or}$$

$$\boldsymbol{y}_i = \boldsymbol{y}_{Goi} + \boldsymbol{y}_{Ri} + \boldsymbol{y}_{Gei} + \boldsymbol{y}_{Bi} \tag{3.7}$$

The vector $\mathbf{y}_i$ is defined as a color channel, and the vector terms $\mathbf{H}_{ji}\ \mathbf{f}_j$ and $\mathbf{y}_{ji}$ (e.g., $\mathbf{H}_{Goi}\ \mathbf{f}_{Go}$ and $\mathbf{y}_{Goi}$) are defined as CCCs. The matrix $\mathbf{H}_{ji}$ operates on channel *j* ($\mathbf{f}_j$) to produce

$\mathbf{y}_{ji}$, which corrupts channel *i*, where *i* and *j* belong to the set {Go, R, Ge, B}. Likewise, we can define each reconstructed channel *i* as:

$$\hat{\boldsymbol{f}}_i = \boldsymbol{A}_{Goi}\,\boldsymbol{y}_{Go} + \boldsymbol{A}_{Ri}\,\boldsymbol{y}_R + \boldsymbol{A}_{Gei}\,\boldsymbol{y}_{Ge} + \boldsymbol{A}_{Bi}\,\boldsymbol{y}_B \tag{3.8}$$

The $\mathbf{A}_{ji}$ matrices are defined as the color channel correction matrices for color channel *i*. For example, $\mathbf{A}_{Goi}$ corrects the color channel Go component of color channel *i*. Each vector term $\mathbf{A}_{ji}\,\mathbf{y}_j$ (e.g., $\mathbf{A}_{Goi}\,\mathbf{y}_{Go}$) is a CCC vector term of the reconstructed color channel vector $\hat{\mathbf{f}}_i$.

Applying the CLS solution from the Section 3.2.2.1 to each CCC term (see Section 3.4.1 for details), our constraints for our separated CCC CLS (SCLS) problem are:

$$\begin{aligned} &\text{minimize: } \| \boldsymbol{Q}_{ji}\,\hat{\boldsymbol{f}}_{ji} \|^2 , \\ &\text{subject to the constraint: } \| \boldsymbol{y}_j - \hat{\boldsymbol{H}}_{ji}\,\hat{\boldsymbol{f}}_{ji} \|^2 = \| \check{\boldsymbol{n}}_j \|^2 , \end{aligned} \tag{3.9}$$

where $\hat{\mathbf{f}}_{ji}$ is the restored CCC value, and the optimal regularization parameter values, β_{ji}, are determined by using an off-line search method (see Section 3.4.2):

$$\beta_{ji} = \text{maximize: } \| \hat{\boldsymbol{f}}_{ji}^{\,2} / \check{\boldsymbol{n}}_j^{\,2} \|^2 \tag{3.10}$$

Thus, our problem formulation consists of the constraints of Equation 3.9x combined with using Equation 3.10x to determine the regularization parameter values. Equations (3.9) and (3.10) are further simplified to scalar form to operate over local pixel areas, as discussed in Section 3.4.2.

The use of SCLS simplifies the Bayer cross-talk problem (Equations (3.1), (3.2), (3.3) and (3.4)) and allows for a direct solution. However, it neglects the correlation of the

errors between different CCC components and introduces an error which will be image dependent. We also use the approximation that the sum of the separately minimized CCC cost function terms will be the minimum of the sum of the cost function terms (weakened optimization). These errors are examined in Section 3.4.1.2. The SCLS simplification benefits outweigh the relatively small errors from an exact solution.

3.2.3 Examination of Existing Image Blurring Solutions

We review single channel blurring restoration in Section 3.2.3.1. We then examine multi-channel blurring in the Section 3.2.3.2. More details on multi-channel blurring restoration methods can be found in Appendix C.

3.2.3.1 Inverse Filtering Problem

A direct solution of the simple degradation problem shown in Figure 3.4 can be found by solving for an estimate $\hat{\mathbf{f}}$ which minimizes the Euclidean norm:

$$min \; || \boldsymbol{y} - \boldsymbol{H}\hat{\boldsymbol{f}} \; ||^2 \tag{3.11}$$

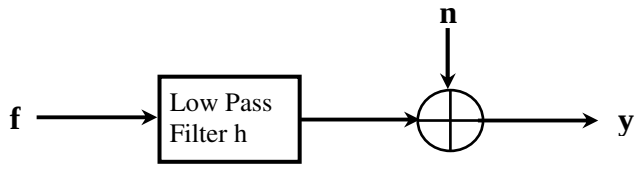

Figure 3.4: Simple blurring and additive noise problem.

This is a least squares fit to the data, and leads to the generalized inverse filter (unconstrained) solution:

$$\hat{\boldsymbol{f}} = (\boldsymbol{H}^T\boldsymbol{H})^{-1}\,\boldsymbol{H}^T\boldsymbol{y}\,, \tag{3.12}$$

with **H** being the matrix form of the convolution filter **h**. When a stationary model is used, **H** is block circulant and can be diagonalized with the use of the 2-D DFT. This is due to the eigenvalues of a block circulant matrix being the 2-D discrete Fourier coefficients of the impulse response of the degradation system, and the eigenvectors being the complex exponential basis functions of this transform [5]. We can write in matrix form:

$$\mathbf{H} = \boldsymbol{W}\boldsymbol{H}\boldsymbol{W}^{-1} , \tag{3.13}$$

where $\boldsymbol{H}$ is a diagonal matrix comprising the 2-D DFT coefficients of **H**, and $\boldsymbol{W}^{-1}$ is a matrix containing the components of the complex exponential basis functions of the 2-D DFT. Using the DFT properties of block circulant matrices, the solution can be written in the discrete frequency domain as:

$$\boldsymbol{F}(l) = \boldsymbol{H}^{*}(l)\boldsymbol{G}(l) \,/\, \|\boldsymbol{H}(l)\|^{2} , \tag{3.14}$$

where $\boldsymbol{F}(l)$ is the DFT of the restored image, $\boldsymbol{H}(l)$ is the PSF (point spread function or blurring) DFT, and $\boldsymbol{G}(l)$ is the observed image DFT. These terms are functions of the 2-D discrete frequency index l, where $l=(k_1,k_2)$ for $k_1,k_2=0,\ldots,N-1$, for a NxN point DFT. In Equation (3.14), * denotes complex conjugation. Using this method, we can solve for the inverse matrix or an inverse convolution filter.

A significant problem with the application of Equation (3.14) is that the blurring problem is ill-posed [82]. Because **H** is ill-conditioned, small bounded deviations may lead to unbounded deviations in the solution. Thus, additional constraints are needed in order to guarantee the uniqueness of the solution and make the problem well-posed. For the cross-talk blurring problem, the degradation matrix **H** is a low pass filter, which means that $H(l)$ is small for l corresponding to high frequencies. Since the noise occurs at all

frequencies, the noise at frequencies where *H(l)* is near zero will be greatly amplified. The condition number of the blurring **H** matrix is the ratio of its maximal and minimal eigenvalues (non-zero values only), and is a measure of how well-posed it is. A problem with a blurring **H** matrix that has a low condition number is said to be well-conditioned, while a problem with a high condition number is said to be ill-conditioned.

Many techniques have been developed to solve this problem [5], including direct, iterative and recursive approaches. Direct approaches to regularization in a restoration problem can use either a stochastic or a deterministic model for the original image. The model represents prior information about the solution that can be used to make the problem well-posed. Stochastic regularization uses a linear filtering approach that computes the estimate $\hat{\mathbf{f}}$:

$$min\ E\{||\ \mathbf{f} - \hat{\mathbf{f}}\ ||^2\} \tag{3.15}$$

Using the stochastic model for **f** and **n** requires prior knowledge of the statistics of the image data that are then used to regularize the problem. Solving the problem using the DFT also requires that the image and noise fields be stationary, which often is not the case. Perhaps most importantly, costly calculations of correlations matrices for the image and noise data must often be performed. It has been shown [93] that stochastic solutions are very sensitive to the accuracy of the estimations of the image and noise correlations. Because of these requirements and constraints, a stochastic regularization approach is not desirable for a low-cost camera system. The linear estimate that minimizes Equation (3.15) leads to the classical form of the Wiener filter:

$$\hat{\mathbf{f}} = \mathbf{R}_{ff}\mathbf{H}^T(\mathbf{H}\mathbf{R}_{ff}\mathbf{H}^T + \mathbf{R}_{nn})^{-1}\mathbf{y}\ , \tag{3.16}$$

where $\mathbf{R}_{ff}$ and $\mathbf{R}_{nn}$ are the correlation matrices of the image and noise data, respectively.

As discussed in Section 3.2.2.1, deterministic regularization applies prior information about the original image for regularizing the restoration problem [31]. The Lagrangian cost function of Equation (3.4) can be solved by performing the indicated minimization. We take the derivative with respect to $\hat{\mathbf{f}}$, set the result to zero and solve, giving:

$$\hat{\boldsymbol{f}} = (\boldsymbol{H}^T\boldsymbol{H} + \beta\boldsymbol{Q}^T\boldsymbol{Q})^{-1}\boldsymbol{H}^T\boldsymbol{y} \tag{3.17}$$

The Lagrange multiplier β must be determined for the given set of constraints [5]. As has been discussed, this often is done in an iterative fashion in order to determine the optimal value.

3.2.3.2 Existing Bayer multi-channel blurring problem solutions

There exist many restoration methods that can be applied to the Bayer cross-talk problem (Equations (3.1), (3.2), and (3.3)). Due to their complexity, memory requirements, and execution time, many of these methods cannot be implemented into simple low-cost camera systems. Other methods in common use for low-cost systems do not adequately correct the image data. We present some of the more important and commonly used restoration methods for Bayer multi-channel blurring in the sections which follow. More details on these methods can be found in Appendix C. Additionally, more restoration methods are reviewed in Appendix C.

3.2.3.2.1 Multi-channel methods that optimize color channel regularization

The more complex multi-color channel restoration methods allow for the optimization of the regularization parameter for each color channel separately. These restoration

methods typically employ an iterative solution or must use estimations of signal and noise statistics. Two methods are developed in [27] for determining the regularization parameter of each color channel: a set theoretic (ST) approach and a constrained least squares (CLS) optimization. These two methods serve as the foundation for many other methods. Both of these methods solve the multiple channel regularization equation:

$$[\boldsymbol{H}^T\boldsymbol{\Lambda}\boldsymbol{H} + \boldsymbol{Q}^T\boldsymbol{Q}]\hat{\boldsymbol{f}} = \boldsymbol{\Lambda}\boldsymbol{H}^T\boldsymbol{y}, \tag{3.18}$$

where $\boldsymbol{\Lambda}$ is a matrix of N color channel regularization parameters (λ_i), and is written in the form:

$$\boldsymbol{\Lambda} = \begin{bmatrix} \lambda_1[I] & 0 & 0 & 0 \\ 0 & \lambda_2[I] & 0 & 0 \\ 0 & 0 & \lambda_3[I] & 0 \\ 0 & 0 & 0 & \lambda_4[I] \end{bmatrix}, \tag{3.19}$$

and where [I] is an identity matrix of size $M^2 \times M^2$. The regularization operator, **Q**, used in [27] has both 2-D Laplacian (within channel smoothing) and 3-D Laplacian (across channel smoothing) components. Using a Laplacian smoothing prior simplifies the problem since it results in a quadratic regularization operator (system of linear equations) [48]. The multi-channel blurring matrix **H** was defined by Equation (3.3). The objective is to determine the optimal regularization parameters (λ_i) of diagonal matrix $\boldsymbol{\Lambda}$.

The ST approach uses a smoothness constraint for each color channel (E_i), where an assumption of equal channel smoothness is used. This is done using an estimate of the full original image (**f**) statistics. This method also requires an estimate of each color channel's additive noise (e_i) . The regularization parameters are then determined from these estimations. The requirement for accurate estimates of E_i and e_i have been found

to be overly restrictive [44]. Iterative methods can be used to determine accurate estimates for the regularization parameters [48].

A CLS optimization approach is developed in [27] for the case when the smoothness constraint value *E* is not known *a priori* or a satisfactory estimate is not available. For this method, we seek a solution $\hat{\mathbf{f}}$ which:

$$\begin{aligned} &\text{minimizes:} && \| \boldsymbol{Qf} \|^2 \\ &\text{subject to:} && \| \boldsymbol{H_i f} - \boldsymbol{y}_i \|^2 = \| \boldsymbol{n}_i \|^2 = e_i^2 \text{ , for } i=1,2, \ldots, N \text{ ,} \end{aligned} \tag{3.20}$$

where $\mathbf{H}_i$ is the i^{th} channel $M^2 \times NM^2$ matrix $\mathbf{H}_i=[\mathbf{H}_{1i}, \mathbf{H}_{2i}, \ldots \mathbf{H}_{Ni}]$ and $\mathbf{n}_i$ is the noise of color channel *i*. The solution of the regularization Equation (3.18) subject to these constraints, Equation (3.20), requires that we must simultaneously find the values of λ_i, which can be written as:

$$Z_i(\lambda_1, \lambda_2, \ldots \lambda_N) = (\| \boldsymbol{H}_i \hat{\boldsymbol{f}} - \boldsymbol{y}_i \|^2 = \| \boldsymbol{n}_i \|^2) \text{ for } i=1,2, \ldots, N \tag{3.21}$$

This leads to a nonlinear problem, which has a very high computational cost, since the roots of the nonlinear functions $Z_i(\lambda_1, \lambda_2, \ldots \lambda_N)$ must be found simultaneously to give the desired λ_i values. Typically, it is solved using an iterative method, such as Newton iterations, to find the matrix of λ_i values (matrix $\boldsymbol{\Lambda}$) of Equation (3.19).

The solution of Equation (3.18) can be written as:

$$\begin{aligned} &\hat{\boldsymbol{f}} = \hat{\boldsymbol{A}} \boldsymbol{y} \text{ , with} \\ &\hat{\boldsymbol{A}} = [\, \boldsymbol{H}^T \boldsymbol{\Lambda} \boldsymbol{H} + \boldsymbol{Q}^T \boldsymbol{Q} \,]^{-1} \boldsymbol{H}^T \end{aligned} \tag{3.22}$$

Then, similar to Equation (3.8), we can write the reconstructed channel *i* using Bayer channel notation (Go, R, Ge, B) as:

$$\hat{\boldsymbol{f}}_i = \hat{\boldsymbol{A}}_{Goi}\,\boldsymbol{y}_{Go} + \hat{\boldsymbol{A}}_{Ri}\,\boldsymbol{y}_R + \hat{\boldsymbol{A}}_{Gei}\,\boldsymbol{y}_{Ge} + \hat{\boldsymbol{A}}_{Bi}\,\boldsymbol{y}_B, \tag{3.23}$$

and the multi-channel restoration matrix $\hat{\mathbf{A}}$ in the Bayer CFA notation (Go, R, Ge, B) is written as:

$$\hat{\boldsymbol{A}} = \begin{bmatrix} \hat{A}_{GoGo} & \hat{A}_{RGo} & \hat{A}_{GeGo} & \hat{A}_{BGo} \\ \hat{A}_{GoR} & \hat{A}_{RR} & \hat{A}_{GeR} & \hat{A}_{BR} \\ \hat{A}_{GoGe} & \hat{A}_{RGe} & \hat{A}_{GeGe} & \hat{A}_{BGe} \\ \hat{A}_{GoB} & \hat{A}_{RB} & \hat{A}_{GeB} & \hat{A}_{BB} \end{bmatrix}, \tag{3.24}$$

As with Equation (3.8), each vector term $\hat{\mathbf{A}}_{ji}\,\mathbf{y}_j$ of Equation (3.23) is a CCC vector term of the reconstructed color channel vector $\hat{\mathbf{f}}_i$. We would like to find a simple, direction form of $\hat{\mathbf{A}}$ which satisfies our requirements of Section 3.2.4.

For both the ST and CLS methods, the amount of within-color channel smoothing and cross-color channel smoothing applied are controlled by the same regularization parameter. This restriction can result in sub-optimal performance, since this solution does not consider the interaction of the channels in determining the optimal regularization values λ_i for each channel. Each λ_i term is optimized using only its channel noise and maximum energy estimations, but each corrected channel will be a function of all the observed channels and all of the regularization parameters ($\hat{\mathbf{f}}_i$=Func{$\mathbf{y}$, $\mathbf{H}$, $\mathbf{Q}$, $\lambda_{i=1,4}$}). These methods also do not take into account the local or global difference of values of the noise terms of the within and cross CCCs. Both of the methods in [27]

use global fixed noise variance values. The use of estimations and iterative steps also make these methods too computationally expensive for our target application.

3.2.3.2.2 Simple direct solutions commonly used in low-cost imaging systems

There are several simple and direct solutions to the Bayer cross-talk blurring problem that can be implemented in low-cost camera systems. However, they use assumptions that limit their performance. Several of these methods are discussed in Appendix C. A simple and common approach used in industry in to correct the signal error due to cross-talk utilizes a 3-by-3 color matrix correction. This correction, which is representative of methods used in low-cost camera systems, essentially performs a linear minimum mean squared error (LMMSE) color correction. The loss of image sharpness is normally corrected in a separate step, which typically is concerned with edge sharpness and not inverse filtering. An optimal 3x3 color correction matrix can be determined using linear regression [43] or calculated from sensor and lighting parameters. The 3x3 color correction matrix $\mathbf{T_{CC}}$ can be broken down into a 3x3 saturation matrix $\mathbf{T_{Sat}}$ and a 3x3 white balance matrix $\mathbf{T_{WB}}$ that only has terms on its main diagonal, as shown:

$$\boldsymbol{T_{Sat}}\ \boldsymbol{T_{WB}} = \boldsymbol{T_{CC}},$$

$$\begin{vmatrix} T_{Sat11} & T_{Sat12} & T_{Sat13} \\ T_{Sat21} & T_{Sat22} & T_{Sat23} \\ T_{Sat31} & T_{Sat32} & T_{Sat33} \end{vmatrix} \begin{vmatrix} T_{WB1} & 0 & 0 \\ 0 & T_{WB2} & 0 \\ 0 & 0 & T_{WB3} \end{vmatrix} = \begin{vmatrix} T_{CC11} & T_{CC12} & T_{CC13} \\ T_{CC21} & T_{CC22} & T_{CC23} \\ T_{CC31} & T_{CC32} & T_{CC33} \end{vmatrix} \qquad (3.25)$$

Using this approach, the white balance matrix corrects for the ambient lighting conditions (dynamic, scene dependent), and the $\mathbf{T_{Sat}}$ matrix coefficients correct for the sensor dependent responses. These sensor dependent responses include cross-talk, as well as the responsivity of silicon and the transmissivity of the CFA used.

In order to maintain the white balance of an image, the $\mathbf{T_{Sat}}$ matrix must have the coefficients of each of its rows sum to one. Thus, as the magnitude of the off-diagonal saturation terms increase, the on-diagonal terms of $\mathbf{T_{Sat}}$ must also increase. This means that for sensors that have more cross-talk, the $\mathbf{T_{Sat}}$ coefficients will have larger values, and the SNR of the processed images will decrease, due to amplification of the noise.

The calculations of the ideal correction coefficients for a 3x3 $\mathbf{T_{Sat}}$ matrix are shown in Figure 3.5. The cross-talk coefficients for a DVGA CMOS sensor are used, where the pixel area applied has been restricted to 3x3 pixels. In the signal diffusion table of the figure, the amount of charge that enters a target pixel (center pixel) and ends up at the specified pixel location is shown. This data is derived from sensor cross-talk characterization [17].

There are several sources of error from using this approach. The mean blurred transfer of signal from one pixel type to neighboring pixel type is used in constructing a 4x4 cross-talk transfer matrix. This forces the averaging of cross-talk that occurs in different directions. For example, a blue pixel has four neighboring red pixels, each of which has a particular cross-talk value. But an average cross-talk value will end up being used for all of its red pixel neighbors. The inverse matrix operation will create a mean blurring correction matrix. Another error is, in order to simplify the camera correction process, the difference in green-even and green-odd pixel responsivity is not taken into account. The correction matrix is reduced from a 4x4 matrix to a 3x3 matrix, which introduces a bias error. The 3x3 correction matrix allows the correction to be applied to a Bayer interpolated pixel triplet (RGB values at each pixel location). Thus, an ideal correction is not possible with this method. By treating the green even and odd pixels the same, a bias error is created since neither pixel type is corrected using the proper coefficients.

This error increases as the asymmetrical behavior of cross-talk increases. Often, simple smoothing or median filtering is used to correct this fixed pattern error [54]. But these methods do not correctly restore the non-blurred image values.

DVGA CMOS sensor Cross-talk coefs, 3x3 area used, amount of charge that entered target pixel (center pixel) that ends up at the specified pixel location

Blue	Green Even
Green Odd	Red

Amount of Signal Diffused to Neighbor Pixels

Wave Length								
Blue Pixel			Green Pixel			Red Pixel		
0.025	0.023	0.015	0.030	0.032	0.022	0.045	0.055	0.036
0.046	0.810	0.020	0.054	0.743	0.031	0.073	0.607	0.046
0.024	0.022	0.015	0.031	0.034	0.023	0.046	0.056	0.036

Mean Transfer from Pixel to Pixel

To \ From	Blue	Green Odd	Green Even	Red
Blue	0.810	0.066	0.085	0.163
Green Odd	0.045	0.743	0.106	0.119
Green Even	0.066	0.106	0.743	0.111
Red	0.079	0.085	0.066	0.607

Inverse Matrix

Inverse of Mean Transfer from Pixel to Pixel

In \ Out	Blue	Green Odd	Green Even	Red
Blue	1.277	-0.062	-0.110	-0.311
Green Odd	-0.041	1.401	-0.175	-0.232
Green Even	-0.085	-0.169	1.397	-0.200
Red	-0.151	-0.170	-0.113	1.742

Reduce to 3x3

In \ Out	Blue	Green	Red
Blue	1.277	-0.086	-0.311
Green	-0.063	1.227	-0.216
Red	-0.151	-0.141	1.742

Mean blurred transfer of signal from one pixel type to neighboring pixel type.

Inverse matrix operation corrects mean blurring

Reduction from 4x4 to 3x3 correction causes further blurring (averaging), thus ideal correction is not possible.

Figure 3.5: Calculations of the color correction matrix for a typical low-cost camera sensor.

This method has no regularization in place, and cannot account for different noise levels. A common industry approach is to adjust the ideal 3x3 $\mathbf{T_{CC}}$ matrix to approach the $\mathbf{T_{WB}}$ matrix as the overall camera system noise increases (or the SNR decreases). Thus, the coefficients of the saturation matrix are reduced in magnitude when higher camera system gains are used (indicative of lower lighting levels and lower SNR). The adjustment is very rough and global (no local effects considered). By using this adaptive

3x3 matrix approach, the performance at the low quality operating conditions (low light, low SNR) is improved. The control for this adjustment is usually tied to camera exposure time, sensor analog gain, and required digital gain. This idea is shown in Figure 3.6 for the same camera system as defined in Figure 3.5.

3x3 Correction Matrix, $\mathbf{T_{CC}}$

	Blue	Green	Red
Blue	1.277	-0.086	-0.311
Green	-0.063	1.227	-0.216
Red	-0.151	-0.141	1.742

Decreasing SNR, Increasing Camera Gain →

3x3 White Balance Matrix, $\mathbf{T_{WB}}$

	Blue	Green	Red
Blue	0.970	0.000	0.000
Green	0.000	1.002	0.000
Red	0.000	0.000	1.343

Figure 3.6: Typical low-cost camera color correction matrix adjustment.

3.2.3.2.3 Summary of limitations of existing multi-channel blurring correction methods

Simple and direct solutions to the Bayer cross-talk blurring problem, such as the ones discussed in Section 3.2.3.2.2 and Appendix C, can be implemented in low-cost camera systems. However, these methods use assumptions that limit their performance, such as not correcting cross-channel blurring and not accurately correcting the spatial blurring due to cross-talk. The more complex restoration methods examined in Section 3.2.3.2.1 and Appendix C require iterative solutions or rely on having accurate estimations of image and noise statistics. Additionally, these regularization methods use a single regularization parameter for all of the CCCs that compose a color channel. These methods also do not use local pixel adaptivity based the HVS's sensitivities and usually do not make use of noise models which vary with signal magnitude.

3.2.4 Requirements and Goals of Our Solution

The goals, requirements, and constraints of our Bayer sensor cross-talk correction method for implementation in a low-cost camera system are:

1) The correction method must be appropriate for a low-cost camera system, which leads to limits on the required memory, operation execution time, and chip area of implementation (complexity of algorithm). Due to execution time limits, the correction method must have a direct, non-iterative, non-recursive approach. Due to limited memory and execution time, we cannot perform real-time global image and noise estimations. We also will not be able to perform real-time frequency domain operations or invert large matrices in the inverse blurring solution. We would like to use a convolution, sliding filter approach, since this matches the implementation of the other image correction methods used in these camera systems and is relatively simple and fast.

2) Our solution must address human visual system (HVS) sensitivities. Specifically, the HVS's sensitivity to local signal to noise contrast and low-frequency color must be optimized in our solution [7], [19], [56], [64], [73], [75], [76], [85]. Thus, we must adjust the regularization parameters based on the HVS's sensitivities. We wish to take advantage of this constraint to simplify the calculations required for the noise and image statistics used. Following these HVS requirements, we wish to create a real-time spatial SNR adaptive solution.

3) Our restoration method must be adaptive to global operating conditions. This requirement follows from the range of lighting and exposure time conditions in which the camera must operate. The algorithm should also be adaptive to local image SNR conditions (item 2 above), as is driven by the HVS behavior [7], [19], [56], [73].

4) We must exploit sensor *a prior* characterization data. In order to use a direct correction method, we must have accurate local pixel SNR estimations. We will meet this goal using mean local estimations derived from sensor characterization data. Simple noise models for the pixels must be used to define pixel SNR behavior curves.

5) We must correct for asymmetrical behavior of cross-talk. Detailed cross-talk characterization data must be used in correcting this blurring. Usually, median or mean filtering is used to correct asymmetrical blurring in low-cost camera systems. These systems do not properly correct the green-even/green-odd pixel mismatch problem. Of course, the wavelength dependent behavior of cross-talk (which defines the $\mathbf{H}_{ji}$ matrices) must be exploited.

6) Our method must apply an accurate white balance correction. For high SNR operating conditions, camera systems generally apply an ideal color correction (see Section 3.2.3.2.2). These corrections include a white balance and a saturation correction. When the operation conditions are poor, with low SNR, a white balance is still performed. However, the saturation correction is reduced or skipped. Our correction method must apply a white balance correction for all operating conditions, but must also be adaptive to the operating SNR in applying the saturation correction. We will later show how our use of separate CCC correction addresses this requirement.

3.3 Proposed Solution to the Bayer Cross-Talk Problem

3.3.1 Motivation and General Approach of Our Proposed Solution

The general ideas of how our proposed solution addresses the various weaknesses of existing restoration methods when applied to the Bayer cross-talk, low-cost camera system problem are presented in this section. We listed in Section 3.2.4 the set of requirements and constraints that we must meet. In this section, we list the general

approach and ideas that we will use to meet these requirements, as well as noting where we have developed new approaches to the solution of the Bayer cross-talk problem.

1) We separate each color channel into a summation of CCCs, which allows the separate regularization of each CCC (refer to Equation (3.7)). This permits exploiting the different degrees of blurring filter ill-conditioning for the CCCs and the SNR values of the color channels. This separation also leads to significantly reducing the complexity of the solution. No restoration methods have previously used this approach.

2) We use the local pixel SNR value to calculate the regularization parameter. This is done to match the HVS's sensitivity to local SNR [7], [19], [56], [73] and low-frequency color error [64], [75], [76], [85]. We have not seen this approach used by other restorations methods. We make use of signal-dependent noise models, determined from sensor characterization, to determine local pixel SNR estimations. The use of local pixel SNR ensures good white color balance, while providing adaptive saturation correction. It does not require expensive signal energy calculations. Instead, *a priori* calculations are performed off-line, reducing the amount of computations that must be done real time. The use of local SNR values for each CCC allows spatially adaptive corrections, whereas most existing methods use global regularization values based on total image signal and noise energies.

3) We use a local mean estimate, or blurred estimate, for the local CCC SNR values. This improves the accuracy of our estimate, while matching the HVS's color error and SNR sensitivity. The improved estimate allows the use of a direct method; instead of an iterative solution that would be too complex and take too long to run. The local averaging process reduces the error in our local CCC SNR estimate by smoothing the noise. Again, we make use of signal-dependent noise models determined from sensor characterization. We have not seen

this locally adaptive approach combined with sensor SNR characterization used by other restorations methods.

4) Detailed cross-talk characterization data is used to create directional (pixel neighborhood) filters. Existing heuristic methods used in low-cost camera systems do not address local non-symmetrical blurring and are not locally adaptive in their corrections. They only have a gross overall camera SNR operating condition adaptivity. These systems do not properly correct the green-even/green-odd pixel mismatch problem.

5) Sensor characterization information is used to create simple noise models for the pixels, which define pixel SNR behavior curves. These noise models will be a function of the pixel signal level. This information, along with cross-talk blurring data, is used to create off-line look-up tables for selecting the optimal regularization parameters that are applied on a local spatial manner across the image. This creates a real-time spatial SNR adaptive solution. Use of sensor characterization is not considered novel.

In our restoration method, we incorporate the HVS attribute that the probability of visual detection is dependent upon the local SNR (contrast sensitivity of the human eye) [7]. This criteria follows from Crozier's Law of signal probability of human detection [19], which states that the psychometric 50% probability of detection is proportional to the constant K = Signal/Noise = SNR. In 1948, Rose [31] used K to relate luminance threshold to noise (SNR). As documented in [48], human visual object detectability is proportional to image contrast and inversely proportional to background noise. We also utilize the HVS's attribute that the low-frequency spatial components of color lead to the optimal color match (Schade experiments [75], [76] and extensions [64], [85]). This shows that, for color accuracy, it is most important to have low spatial frequency data color corrected accurately. This behavior of the HVS is depicted in Figure 3.7. Using

local averaged values of pixel data provides more accurate estimations of local mean pixel SNR and low spatial frequency color measurements, due to the smoothing of noise.

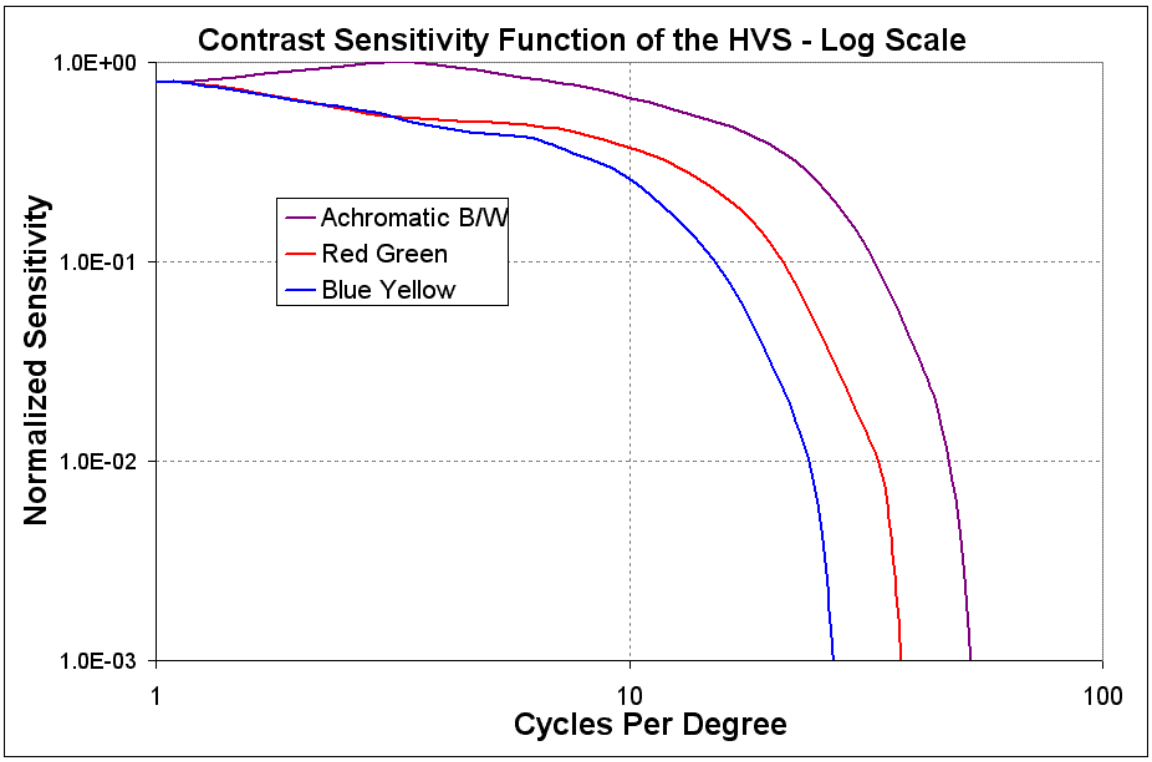

Figure 3.7: HVS is sensitive to low spatial frequency color saturation [64], [85] and their errors.

3.3.2 General Approach of Separating CCC Terms

The separation of each color channel into a summation of CCCs allows the separate regularization of each CCC. This provides the advantage of allowing the use of different regularization parameters for each component, instead of one best value applied to all of the components. Existing restoration methods, such as [27], use a single regularization parameter for each component. The advantage of the CCC separation can be seen by looking at the regularization estimate of the input signal:

$$\hat{\boldsymbol{f}} = \{\boldsymbol{H}^T\boldsymbol{H} + \beta\boldsymbol{Q}^T\boldsymbol{Q}\}^{-1}\,\boldsymbol{H}^T\boldsymbol{y}\ , \text{ or}$$

$$\hat{\boldsymbol{f}} = \boldsymbol{A}(\beta)\boldsymbol{y}\ , \tag{3.26}$$

$$\text{where } \boldsymbol{A}(\beta) = \{\boldsymbol{H}^T\boldsymbol{H} + \beta\boldsymbol{Q}^T\boldsymbol{Q}\}^{-1}\,\boldsymbol{H}^T \tag{3.27}$$

The terms in Equations (3.26) and (3.27) are defined in Sections 3.2.2 and 3.2.3.1, and β is used as the regularization parameter. Equation (3.26) can be written for one of the Bayer color channel as:

$$\hat{\boldsymbol{f}}_i = \boldsymbol{A}_i(\beta_i)\boldsymbol{y}\ , \tag{3.28}$$

where $\mathbf{A}_i$ is the i^{th} channel $M^2 \times NM^2$ matrix $\mathbf{A}_i=[\mathbf{A}_{1i}, \mathbf{A}_{2i}, \ldots \mathbf{A}_{Ni}]$. Equation (3.28) can be written as the summation of CCCs of color channel *i*:

$$\hat{\boldsymbol{f}}_i = \sum_{j=0}^{3} \boldsymbol{A}_{ji}(\beta_i)\boldsymbol{y}_j \tag{3.29}$$

As was discussed in Section 3.2.2.2, we can define our color component terminology using Equation (3.29) as reference. The vector $\hat{\mathbf{f}}_i$ is defined as a corrected color channel (e.g., corrected red). The terms $\mathbf{A}_{ji}(\beta_i)\mathbf{y}_j$ (e.g., $\mathbf{H}_{GoR}\,\mathbf{f}_{Go}$) are defined as corrected CCCs. For each Bayer color channel, there are four components that are used in either the correction or blurring of the channel's value.

In Equation (3.29), which follows the multi-channel methods such as [27], we see that there is one value of the regularization parameter for each color channel *i*. We can improve the noise smoothing, data fidelity matching trade-off (noise variance/bias) by allowing a separate regularization parameter for each CCC. We can then write Equation (3.29) as:

$$\hat{\boldsymbol{f}}_i = \sum_{j=0}^{3} \boldsymbol{A}_{ji}(\beta_{ji})\boldsymbol{y}_j \,, \tag{3.30}$$

The advantage in using the form of Equation (3.30) comes from each color channel (within the local neighborhood) $\mathbf{y}_j$ having different local SNR values and each of the blurring matrices that operate on the different CCCs having different degrees of ill-conditioning (from the eigenvalue magnitudes). Thus, we find an optimum regularization parameter, β_{ji}, for each CCC of each color channel. This gives us 4 values per pixel (which has only one color channel), and 16 values for a local 4 channel/4 pixel kernel area. The derivation of the cost functions for this approach are located in Section 3.4.1.1.

3.4 Derivation of Deterministic Separated CLS Local SNR Method

In deriving our deterministic regularized constrained least squares separated CCC local pixel SNR method (SCLS SNR), we first discuss the separation of the CCC in Section 3.4.1. Then in Section 3.4.2, we consider how to at determine the CCC regularization parameter value in order to optimize the corrected local pixel mean signal SNR.

3.4.1 Derivation of Bayer Cross-Talk Problem Separation of Color Channel Components

3.4.1.1 Bayer Blurring Problem Cost Function

In Sections 3.2.3.1 and 3.2.3.2.1, cost functions were presented for single and multi-channel blurring problems. In this section we derive separate CCC cost functions for the Bayer blurring problem. We showed in Section 3.2.2 that the Bayer multi-channel blurring problem can be written in stacked vector and matrix form with Equation (3.1):

$$\boldsymbol{y} = \boldsymbol{H}\,\boldsymbol{f} + \boldsymbol{n}$$

where the $NM^2 \times 1$ vectors **y**, **f**, and **n** are defined by Equation (3.2), and the $NM^2 \times NM^2$ multi-channel blurring matrix **H** for N color channel is defined by Equation (3.3). The full blurring matrix **H** was shown to be composed of stationary block-circulant $M^2 \times M^2$ sub matrices $\mathbf{H}_{ji}$, where the *j* index is the input color channel and the *i* index is the output (blurred) color channel.

The noise, **n**, that is represented in Equations (3.1) and (3.2) is signal-dependent, zero mean, Gaussian, and uncorrelated from pixel to pixel. We discuss basic information on image sensor noise in Section 2.3.1. Detailed information on CMOS image sensor noise is presented in Appendix A. Fixed pattern or time-invariant noise can usually be eliminated by the imaging sensor design. The temporal noise sources are generally uncorrelated from pixel to pixel [42]. When light intensity is integrated over times longer than the coherence time and is large, the Poisson-to-normal limit is appropriate (the central limit theorem, CLT, applies). That is, when the number of photons detected by the device is large, then the signal can be well modeled by a signal-dependent Gaussian distribution. For low light intensity situations, the independent Gaussian read noise, pixel offset, pixel gain variation, and other noise sources will dominate over the Poisson shot noise. Thus, the noise can still be approximated as an independent Gaussian model. We then can use a pixel to pixel independent signal-dependent Gaussian model for the sensor noise. This signal to noise relationship is characterized for our target sensor and is available as *a priori* data for our restoration method.

We showed in Section 3.2.2 that for the Bayer case, we can write each output blurred channel *i* using Equation (3.7):

$$\boldsymbol{y}_i = \boldsymbol{H}_{Goi}\,\boldsymbol{f}_{Go} + \boldsymbol{H}_{Ri}\,\boldsymbol{f}_{R} + \boldsymbol{H}_{Gei}\,\boldsymbol{f}_{Ge} + \boldsymbol{H}_{Bi}\,\boldsymbol{f}_{B}\,,$$

where the vector $\mathbf{y}_i$ is defined as a color channel and the $\mathbf{H}_{ji}$ $\mathbf{f}_j$ terms are defined as CCCs. For each color channel, there are four components that are used in the correction and blurring of the channel's value.

Since matrix **H** is composed of stationary block-circulant sub matrices ($\mathbf{H}_{ji}$), we can use the properties of the DFT to solve the corresponding N equations for the N input color channels (the eigenvalues of a block circulant matrix are the 2-D DFT coefficients). This will give us the inverse of the blurring matrix:

$$\boldsymbol{G} = (\boldsymbol{H}^T\boldsymbol{H})^{-1}\,\boldsymbol{H}^T\,, \tag{3.31}$$

The de-blurring (inverse filter) matrix **G** will also be composed of stationary block-circulant sub matrices. Due to the circulant properties of the blurring, both the blurring and de-blurring operations can be applied in a convolution (sliding filter window) manner. Since the problem is ill-posed (due to the blurring matrices $\mathbf{H}_{ij}$) and noise is added, when we solve for the input channels we get the naïve (or inverse) solution ($\mathbf{f}^+_i$):

$$\boldsymbol{f}^+_i = \boldsymbol{G}_{Goi}\,\boldsymbol{y}_{Go} + \boldsymbol{G}_{Ri}\,\boldsymbol{y}_{R} + \boldsymbol{G}_{Gei}\,\boldsymbol{y}_{Ge} + \boldsymbol{G}_{Bi}\,\boldsymbol{y}_{B}\,, \tag{3.32}$$

which can have significant noise amplification. In matrix form for all four of the Bayer channels, we can write the naïve, simple inverse solution as:

$$\begin{bmatrix} f^+_{Go} \\ f^+_{R} \\ f^+_{Ge} \\ f^+_{B} \end{bmatrix} = \begin{bmatrix} G_{GoGo} & G_{RGo} & G_{GeGo} & G_{BGo} \\ G_{GoR} & G_{RR} & G_{GeR} & G_{BR} \\ G_{GoGe} & G_{RGe} & G_{GeGe} & G_{BGe} \\ G_{GoB} & G_{RB} & G_{GeB} & G_{BB} \end{bmatrix} \begin{bmatrix} y_{Go} \\ y_{R} \\ y_{Ge} \\ y_{B} \end{bmatrix}, \tag{3.33}$$

where, in the above matrix equation, the $\mathbf{G}_{ji}$ matrices can be easily found using the DFT convolution properties. We note that although $\mathbf{G}=(\mathbf{H}^T\mathbf{H})^{-1}\mathbf{H}^T$, in general $\mathbf{G}_{ji}\neq\mathbf{H}_{ji}^{-1}$.

Per our definition, we see again in Equation (3.32) that the vector $\mathbf{f}^+_i$ is referred to as a color channel. The terms $\mathbf{G}_{ji}\ \mathbf{y}_j$ (e.g., $\mathbf{G}_{GoR}\ \mathbf{y}_{Go}$) are identified as CCCs, where there are four of these components that are used in the correction of a channel's value. We see in Figure 3.8 that we can view each color component correction as being composed of the sum of independent color channel corrections. For the Bayer 4 channel case, each corrected color component in Equation (3.33) is composed of the sum four color channel corrections. The original color corruption problem also can be viewed as four separate color component corruptions for each color channel.

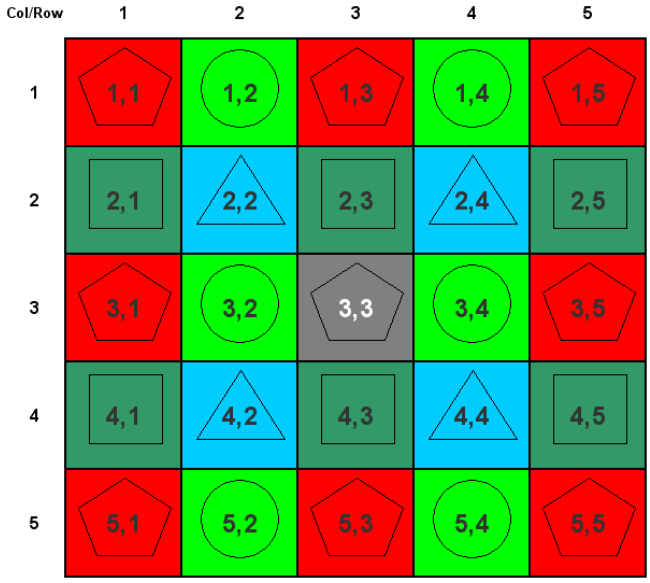

Pixel at location (3,3) is corrupted by pixels in 5x5 neighborhood
Four pixel types (R, Ge, Go, B), e.g., Blue pixels are at (2,2), (2,4), (4,2), (4,4)
Corruption can be viewed as 4 filters ($\mathbf{H}_{ji}$) operating on 4 pixel types ($\mathbf{f}_j$)
Correction can be viewed as 4 filters ($\mathbf{G}_{ji}$ or $\mathbf{W}_{ji}$) operating on 4 pixel types ($\mathbf{y}_j$)
Operations can be limited to local 5x5 pixel area shown.

Figure 3.8: Local extent of the cross-talk blurring and correction filters. Each blurring and correction will consist of between 4 and 9 pixels.

Since we have an ill-conditioned problem, we will use a deterministic regularization approach to find the solution of Equation (3.1) [5], [31]. We then wish to find the minimization of the CLS objective (cost) function [3], [5], [26]:

$$\phi(\mathbf{f}, \beta) = \| \mathbf{H}\,\mathbf{f} - \mathbf{y} \|^2 + \beta \| \mathbf{Q}\,\mathbf{f} \|^2 , \tag{3.34}$$

where we have imposed a constraint on the smoothness ($\| \mathbf{Q}\,\mathbf{f} \|^2$) of the least squares fit of the data ($\| \mathbf{H}\,\mathbf{f} - \mathbf{y} \|^2$). This gives the estimate of the input signal as [3], [5], [31]:

$$\hat{\mathbf{f}} = \{\mathbf{H}^T\mathbf{H} + \beta\mathbf{Q}^T\mathbf{Q}\}^{-1}\,\mathbf{H}^T\mathbf{y} \tag{3.35}$$

The regularization parameter β can be selected based on different optimization criteria, such as constrained noise and signal energies [26]. In our solution, we select the value of the regularization parameter β based upon an estimate of the corrected signal to noise ratio (SNR). The corrected SNR estimate is determined using noise models, as discussed in Section 3.4.2.2. This criteria is similar to the MMSE solution approach [26]. Furthermore, in our solution, we separate the corrected signal $NM^2 \times 1$ vector $\hat{\mathbf{f}}$ into CCC terms, as indicated by the four terms in the naïve solution of Equation (3.32). This approach gives us Equation (3.8) of Section 3.2.2.2, the color reconstructed channel *i* vector $\mathbf{f}_i$ written as:

$$\hat{\mathbf{f}}_i = \mathbf{A}_{Goi}\,\mathbf{y}_{Go} + \mathbf{A}_{Ri}\,\mathbf{y}_R + \mathbf{A}_{Gei}\,\mathbf{y}_{Ge} + \mathbf{A}_{Bi}\,\mathbf{y}_B \text{, or}$$

$$\hat{\mathbf{f}}_i = \hat{\mathbf{f}}_{Goi} + \hat{\mathbf{f}}_{Ri} + \hat{\mathbf{f}}_{Gei} + \hat{\mathbf{f}}_{Bi} ,$$

and the ideal input channel *i* vector $\mathbf{f}_i$ written as:

$$\mathbf{f}_i = \mathbf{f}_{Goi} + \mathbf{f}_{Ri} + \mathbf{f}_{Gei} + \mathbf{f}_{Bi} , \tag{3.36}$$

where we have 4 CCC terms per color channel, each of which is a $M^2 \times 1$ vector. We do this in order to replace the optimization Equation (3.34) with 16 separate optimization equations (with 16 different β_{ji} terms) of the form:

$$\phi(\mathbf{f}_{ji}, \beta_{ji}) = \| \hat{\mathbf{H}}_{ji} \mathbf{f}_{ji} - \mathbf{y}_j \|^2 + \beta_{ji} \| \mathbf{Q}_{ji} \mathbf{f}_{ji} \|^2 \quad (3.37)$$

In Equation (3.37), $\hat{\mathbf{H}}_{ji}$ is the blurring applied to channel *i* by channel *j* for CCC term $\mathbf{f}_{ji}$, where $\mathbf{f}_{ji}$ is the component of channel *i* due to channel *j*, which is dependent upon $\mathbf{y}_j$. The separation of the cost function of Equation (3.34) into the CCC cost functions of Equation (3.37) results in weakened optimization, and introduces an error which is examined in Section 3.4.1.2. Since both the cross-talk blurring and de-blurring matrices are block circulant, we can use the DFT to easily solve for the $\hat{\mathbf{H}}_{ji}$ values:

$$\mathbf{G}_{ji} = [\{\mathbf{H}^T \mathbf{H}\}^{-1} \mathbf{H}^T]_{ji} , \quad (3.38)$$

where $\mathbf{G}_{ji}$ is defined as a circulant component sub-matrix of the complete inverse of matrix **H**, and

$$\hat{\mathbf{H}}_{ji} = \{\mathbf{G}_{ji}^T \mathbf{G}_{ji}\}^{-1} \mathbf{G}_{ji}^T , \quad (3.39)$$

where $\hat{\mathbf{H}}_{ji}$ is defined as the inverse of the ideal correction component sub-matrix $\mathbf{G}_{ji}$.

One of the advantages of separating the single cost function of Equation (3.34), for the Bayer case, into 16 separate cost functions of Equation (3.37) is that we can use individual optimal regularization parameters β_{ji}. These β_{ji} terms are matched to the stability or sensitivity (seen from the eigenvalues) of the blurring filters $\hat{\mathbf{H}}_{ji}$. The eigenvalues of each of the 16 color-channel-to-color-channel blurring filters and their corresponding 2-D Laplacian regularization filters are listed in Tables 3.1 and 3.2, respectively. The differences in the filters' stabilities can be seen from this eigenvalue

data, which determine the matrix condition numbers. The eigenvalue data was calculated based upon the characterization cross-talk data shown in Figure 3.3 for red, green and blue color filter pixels. As mentioned, the assumptions and errors associated with applying weakened optimization in converting Equation (3.34) to Equation (3.37) are presented in Section 3.4.1.2. Using the approach of Equation (3.37) gives the estimate of the input signal CCC $M^2 \times 1$ vector, $\hat{\mathbf{f}}_{ji}$, as:

$$\hat{\boldsymbol{f}}_{ji} = \{ \hat{\boldsymbol{H}}_{ji}^T \hat{\boldsymbol{H}}_{ji} + \beta_{ji} \boldsymbol{Q}_{ji}^T \boldsymbol{Q}_{ji} \}^{-1} \hat{\boldsymbol{H}}_{ji}^T \boldsymbol{y}_j , \tag{3.40}$$

and the estimate of an input signal color channel ($\hat{\mathbf{f}}_i$) as:

$$\hat{\boldsymbol{f}}_i = \sum_{j=0}^{4} \{ \hat{\boldsymbol{H}}_{ji}^T \hat{\boldsymbol{H}}_{ji} + \beta_{ji} \boldsymbol{Q}_{ji}^T \boldsymbol{Q}_{ji} \}^{-1} \hat{\boldsymbol{H}}_{ji}^T \boldsymbol{y}_j \tag{3.41}$$

The regularization of the CCC of Equation (3.40) is illustrated in the matrix operation of Figure 3.9. The optimization Equations (3.40) and (3.41), along with Equations (3.32), (3.36), (3.38), and (3.39), can be used to define the naïve (inverse) component solution (where β_{ji} is set to zero) as:

$$\boldsymbol{f}^+_{ji} = \boldsymbol{G}_{ji} \boldsymbol{y}_j , \tag{3.42}$$

where from Equations (3.14) and (3.40), we have :

$$\boldsymbol{G}_{ji} = \boldsymbol{A}_{ji}(\beta_{ji}=0) = \{ \hat{\boldsymbol{H}}_{ji}^T \hat{\boldsymbol{H}}_{ji} \}^{-1} \hat{\boldsymbol{H}}_{ji}^T = [\{\boldsymbol{H}^T \boldsymbol{H}\}^{-1} \boldsymbol{H}^T]_{ji} \tag{3.43}$$

Looking at existing restoration methods that are used to solve the multi-channel problem, we see from Equations (3.18) and (3.19) [27], that each $\hat{\mathbf{f}}_i$ estimate (color channel solution) is a function of all four λ_i values (they are all present in the $\boldsymbol{\Lambda}$ matrix

terms for all of the $\hat{\mathbf{f}}_i$'s). From Equation (3.41), we see that our $\hat{\mathbf{f}}_i$ estimate is also a function of four β_{ji} values (as well as $\hat{\mathbf{H}}_{ji}$ being a function of function of all 16 H_{ji} sub-matrices). We have, however, separated the solution of $\hat{\mathbf{f}}_i$ into CCCs at the expense of ignoring the cross-channel component correlations. This simplification greatly reduces the complexity of the problem, while avoiding the use of image cross-channel correlations that are costly to calculate. Additionally, it has been shown [93] that stochastic methods which use this cross channel signal correlations data are very sensitive to errors in the correlation statistics.

Table 3.1: Eigenvalues of each of the 16 color-channel-to-color-channel blurring filters, $\hat{H}_{ji}^{T}\hat{H}_{ji}$. Note that these matrix filters are of size 5x5. Eigenvalues less than 1E-5 are ignored (clipped to zero).

Ĥ_GoGo	**Ĥ_RGo**	**Ĥ_GeGo**	**Ĥ_BGo**
5.13E-01	3.10E+01	1.47E+02	7.18E+02
0.00E+00	1.97E-05	8.46E-02	1.88E+00
0.00E+00	0.00E+00	0.00E+00	0.00E+00
0.00E+00	0.00E+00	0.00E+00	0.00E+00
0.00E+00	0.00E+00	0.00E+00	0.00E+00
Ĥ_GoR	**Ĥ_RR**	**Ĥ_GeR**	**Ĥ_BR**
5.95E+01	3.03E-01	9.96E+01	1.95E+02
2.91E-04	0.00E+00	3.11E-02	7.49E-02
0.00E+00	0.00E+00	0.00E+00	0.00E+00
0.00E+00	0.00E+00	0.00E+00	0.00E+00
0.00E+00	0.00E+00	0.00E+00	0.00E+00
Ĥ_GoGe	**Ĥ_RGe**	**Ĥ_GeGe**	**Ĥ_BGe**
1.55E+02	3.34E+01	5.14E-01	2.11E+02
1.44E-01	3.50E-04	0.00E+00	2.64E-02
0.00E+00	0.00E+00	0.00E+00	0.00E+00
0.00E+00	0.00E+00	0.00E+00	0.00E+00
0.00E+00	0.00E+00	0.00E+00	0.00E+00
Ĥ_GoB	**Ĥ_RB**	**Ĥ_GeB**	**Ĥ_BB**
2.94E+02	4.23E+01	1.46E+02	6.42E-01
3.11E-01	1.07E-03	5.46E-02	0.00E+00
0.00E+00	0.00E+00	0.00E+00	0.00E+00
0.00E+00	0.00E+00	0.00E+00	0.00E+00
0.00E+00	0.00E+00	0.00E+00	0.00E+00

Table 3.2: Eigenvalues of each of the 16 color-channel-to-color-channel Laplacian regularization filters, $Q_{ji}^T Q_{ji}$. Note that these matrix filters are of size 5x5. Eigenvalues less than 1E-5 are ignored (clipped to zero).

Q_GoGo	**Q_RGo**	**Q_GeGo**	**Q_BGo**
1.25E+01	1.65E+01	8.00E+00	1.65E+01
6.81E-01	6.98E-01	2.00E+00	6.98E-01
0.00E+00	0.00E+00	0.00E+00	0.00E+00
0.00E+00	0.00E+00	0.00E+00	0.00E+00
0.00E+00	0.00E+00	0.00E+00	0.00E+00
Q_GoR	**Q_RR**	**Q_GeR**	**Q_BR**
1.65E+01	1.25E+01	1.65E+01	8.00E+00
6.98E-01	6.81E-01	6.98E-01	2.00E+00
0.00E+00	0.00E+00	0.00E+00	0.00E+00
0.00E+00	0.00E+00	0.00E+00	0.00E+00
0.00E+00	0.00E+00	0.00E+00	0.00E+00
Q_GoGe	**Q_RGe**	**Q_GeGe**	**Q_BGe**
8.00E+00	1.65E+01	1.25E+01	1.65E+01
2.00E+00	6.98E-01	6.81E-01	6.98E-01
0.00E+00	0.00E+00	0.00E+00	0.00E+00
0.00E+00	0.00E+00	0.00E+00	0.00E+00
0.00E+00	0.00E+00	0.00E+00	0.00E+00
Q_GoB	**Q_RB**	**Q_GeB**	**Q_BB**
1.65E+01	8.00E+00	1.65E+01	1.25E+01
6.98E-01	2.00E+00	6.98E-01	6.81E-01
0.00E+00	0.00E+00	0.00E+00	0.00E+00
0.00E+00	0.00E+00	0.00E+00	0.00E+00
0.00E+00	0.00E+00	0.00E+00	0.00E+00

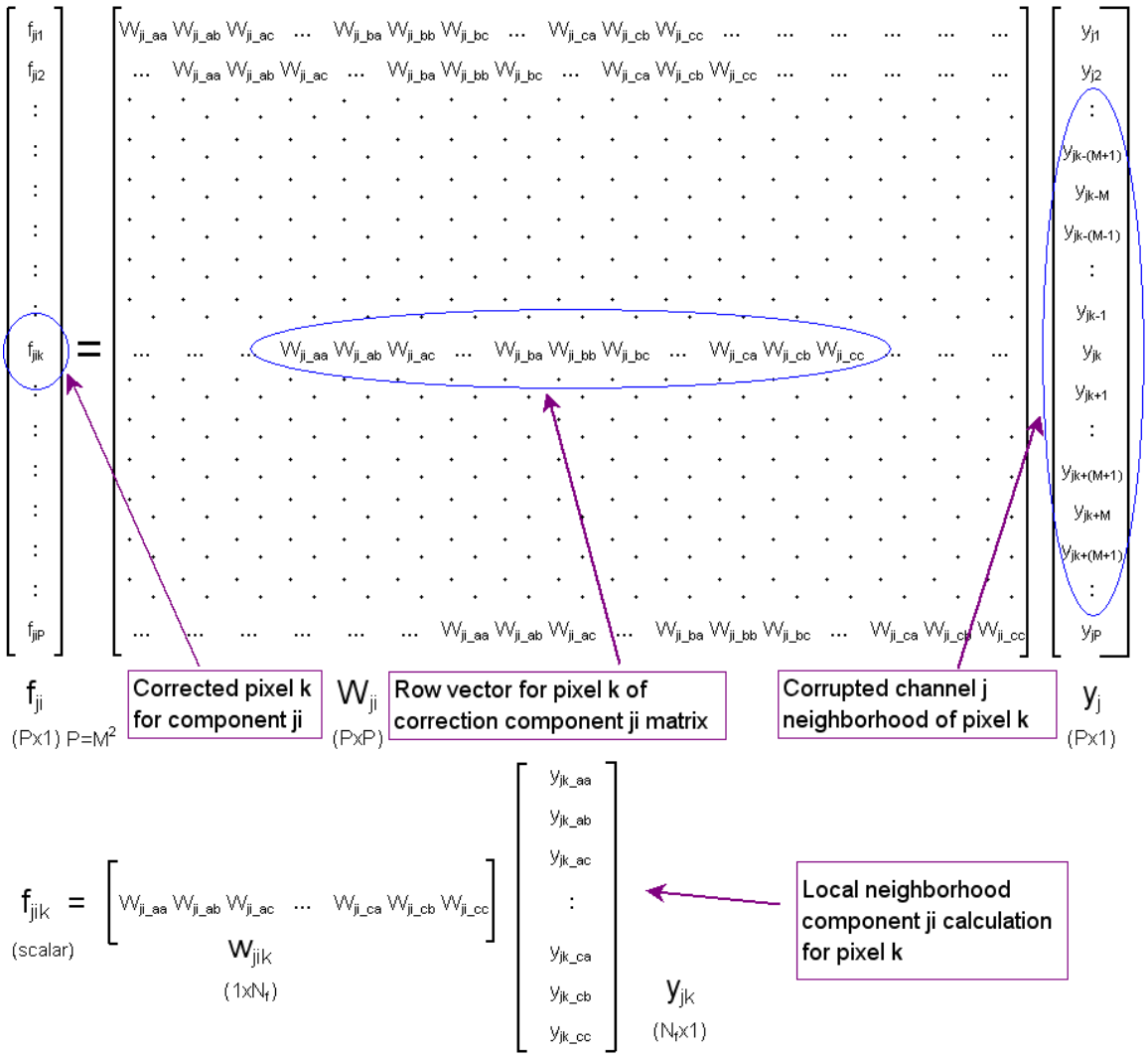

Figure 3.9: Regularization matrix equation showing the relationship between the corrected CCC *ji* term at pixel *k*, and the observed channel *j* pixel values in the local neighborhood of pixel *k*. Local pixel *k* component *ji* shown calculated for local extent regularization, where N_f will usually be between 4 and 9.

3.4.1.2 Error Due to Not Considering Cross CCC Error Correlation

We now look at the error introduced by using our separation set of color component cost functions simplification instead of the full matrix cost function equation. We will determine the error in using Equation (3.37) for 16 separate optimizations instead of using the full matrix Equation (3.34). Rewriting Equation (3.34) in terms of minimizing the difference between the ideal and corrected signals (using **f** – **Gy** instead of **y** – **Hf**):

$$\phi(\boldsymbol{f}, \boldsymbol{\beta}) = \| \boldsymbol{f} - \boldsymbol{Gy} \|^2 + \boldsymbol{\beta} \| \boldsymbol{GQf} \|^2 , \quad (3.44)$$

where we have previously defined $\mathbf{G} = \{\mathbf{H}^T\mathbf{H}\}^{-1}\ \mathbf{H}^T$. We can define the modified smoothness constraint:

$$\boldsymbol{Q'f} = \boldsymbol{GQf} , \quad (3.45)$$

and then update the smoothness constraint matrices coefficient values and drop the prime on **Q** for simplicity, giving us:

$$\phi(\boldsymbol{f}, \boldsymbol{\beta}) = \| \boldsymbol{f} - \boldsymbol{Gy} \|^2 + \boldsymbol{\beta} \| \boldsymbol{Qf} \|^2 , \quad (3.46)$$

We see from Equation (3.46) that we are performing a constrained least squares regularization of the difference (**f**–**Gy**) instead of (**y**–**Hf**). This is done to allow the separation of the CCCs of **f** in the optimization functional, since we have $\mathbf{f}^+_{ji} = \mathbf{G}_{ji}\mathbf{y}_j$ (refer to Equations (3.40) and (3.42)). Expanding terms in Equation (3.46), we can write:

$$\phi(\mathbf{f}, \beta) = \left\| \sum_{i=0}^{3} \mathbf{f}_i - \sum_{i=0}^{3} \mathbf{G}_i\mathbf{y} \right\|^2 + \beta \left\| \sum_{i=0}^{3} \mathbf{Q}_i\,\mathbf{f} \right\|^2 , \quad (3.47)$$

Further expanding the terms gives:

$$\phi(\boldsymbol{f}, \boldsymbol{\beta}) = \sum_{i=0}^{3} \left\| \boldsymbol{f}_i - \boldsymbol{G}_i\boldsymbol{y} \right\|^2 + \sum_{m,n,n\neq m} (\boldsymbol{f}_m - \boldsymbol{G}_m\boldsymbol{y})^T(\boldsymbol{f}_n - \boldsymbol{G}_n\boldsymbol{y}) +$$

$$\sum_{i=0}^{3} \beta_i \| \boldsymbol{Q}_i\,\boldsymbol{f} \|^2 + \sum_{m,n,n\neq m} \beta_m\, (\boldsymbol{Q}_m\,\boldsymbol{f})^T(\boldsymbol{Q}_n\,\boldsymbol{f}) \quad (3.48)$$

We observe that the matrix $\mathbf{Q}_j$ is defined to operate only on the channel *j* data. Thus, the coefficients of the matrix product $\mathbf{Q}_j^T\mathbf{Q}_i$ will be equal to zero when $i \neq j$. So the last term in the above equation will be a zero vector:

$$\sum_{m,n,n\neq m} \beta_m (\boldsymbol{Q}_m \boldsymbol{f})^T(\boldsymbol{Q}_n \boldsymbol{f}) = \boldsymbol{0} \tag{3.49}$$

Likewise, the cross-channel error product terms in the Equation (3.48) will also be zero since the color channel vectors ($\mathbf{f}_m - \mathbf{G}_m\mathbf{y}$) and ($\mathbf{f}_n - \mathbf{G}_n\mathbf{y}$) have no non-zero terms in common vector positions when $m \neq n$. So the second term in Equation (3.48) will also be a zero vector:

$$\sum_{m,n,n\neq m} (\boldsymbol{f}_m - \boldsymbol{G}_m\boldsymbol{y})(\boldsymbol{f}_n - \boldsymbol{G}_n\boldsymbol{y}) = \boldsymbol{0} \tag{3.50}$$

Equation (3.48) is then the same as applying the method of Lagrange multipliers with the minimum criteria, $||\mathbf{f}_i - \mathbf{G}_i\mathbf{y}||^2$, and the smoothness constraints, $||\mathbf{Q}_i\mathbf{f}||^2$, which leads to the CLS summation cost function equation (refer to Equation (2.12) of [27]):

$$\phi(\boldsymbol{f}, \boldsymbol{\beta}) = \sum_{i=0}^{3} \{ || \boldsymbol{f}_i - \boldsymbol{G}_i\boldsymbol{y} ||^2 + \beta_i || \boldsymbol{Q}_i \boldsymbol{f} ||^2 \} , \tag{3.51}$$

where $\mathbf{G}_i$ and $\mathbf{Q}_i$ are the i^{th} channel $M^2 x NM^2$ matrices:

$\boldsymbol{G}_i=[\boldsymbol{G}_{1i}, \boldsymbol{G}_{2i}, \ldots \boldsymbol{G}_{Ni}]$, and

$\boldsymbol{Q}_i=[\boldsymbol{Q}_{1i}, \boldsymbol{Q}_{2i}, \ldots \boldsymbol{Q}_{Ni}]$ for color channel *i*.

In Equation (3.51), each color channel ($\mathbf{f}_i$) has its fidelity to the observed data ($\mathbf{g}$) calculated separately. We presume that minimizing each $\phi(\mathbf{f}_i, \beta_i)$ term of the summation

in Equation (3.51) independently (with a separate regularization parameter β_i) will result in an optimal cost function:

$$min[\ \phi(\mathbf{f}, \boldsymbol{\beta})\ ] \longrightarrow \sum_{i=0}^{3} \quad min[\ \phi(\mathbf{f}_i, \beta_i)\ ] \tag{3.52}$$

We can then write for one color channel *i*:

$$\phi(\mathbf{f}_i, \beta_i) = \| \mathbf{f}_i - \mathbf{G}_i \mathbf{y} \|^2 + \beta_i \| \mathbf{Q}_i \mathbf{f} \|^2 \tag{3.53}$$

We must note at this point that the term $\mathbf{Q}_i \mathbf{f}$ will have components which are dependent upon $\mathbf{f}_i$ for i=1,…,N (N=4). This implies that, as with the ST approach [27], this simplification of minimizing separate channel cost functions may lead to a sub-optimal solution or weakened optimization.

Expanding terms in Equation (3.53), we can write:

$$\phi(\mathbf{f}_i, \beta_i) = \Big\| \sum_{j=0}^{3} \mathbf{f}_{ji} - \sum_{j=0}^{3} \mathbf{G}_{ji} \mathbf{y}_j \Big\|^2 + \beta_i \Big\| \sum_{j=0}^{3} \mathbf{Q}_{ji} \mathbf{f}_j \Big\|^2 ,$$

$$\phi(\mathbf{f}_i, \beta_i) = \Big\| \sum_{j=0}^{3} \mathbf{f}_{ji} - \sum_{j=0}^{3} \mathbf{G}_{ji} \mathbf{y}_j \Big\|^2 + \beta_i \Big\| \sum_{j=0}^{3} \mathbf{Q}_{ji} \Big(\sum_{k=0}^{3} \mathbf{f}_{jk} \Big) \Big\|^2 \tag{3.54}$$

Now we observe that the M^2xM^2 matrix $\mathbf{Q}_{ji}$ is defined to operate only on the channel *j* to channel *i* CCC. The coefficients at all other color channel locations will be equal to zero. This matches the non-zero coefficient locations of the M^2xM^2 $\mathbf{H}_{ji}$ and $\mathbf{G}_{ji}$ matrices. Thus, we can write by definition:

$\boldsymbol{Q}_{ji}\,\boldsymbol{f}_{jk} = \boldsymbol{0}$ for all $i \neq k$, and

$$\boldsymbol{Q}_{ji}\,\boldsymbol{f}_{j} = \boldsymbol{Q}_{ji}\,\boldsymbol{f}_{ji} \tag{3.55}$$

We note that $\mathbf{f}_j$ and $\mathbf{f}_{ji}$ are both M^2x1 column vectors. Then we have:

$$\phi(\boldsymbol{f}_i, \beta_i) = \Big\| \sum_{j=0}^{3} \boldsymbol{f}_{ji} - \sum_{j=0}^{3} \boldsymbol{G}_{ji}\boldsymbol{y}_j \Big\|^2 + \beta_i \Big\| \sum_{j=0}^{3} \boldsymbol{Q}_{ji}\,\boldsymbol{f}_{ji} \Big\|^2 \tag{3.56}$$

Further expanding the terms:

$$\begin{aligned}\phi(\boldsymbol{f}_i, \beta_i) = {} & \sum_{j=0}^{3} \Big\| \boldsymbol{f}_{ji} - \boldsymbol{G}_{ji}\boldsymbol{y}_j \Big\|^2 + \sum_{m,n,n\neq m} (\boldsymbol{f}_{mi} - \boldsymbol{G}_{mi}\boldsymbol{y}_m)(\boldsymbol{f}_{ni} - \boldsymbol{G}_{ni}\boldsymbol{y}_n) + \\ & \sum_{j=0}^{3} \beta_i \| \boldsymbol{Q}_{ji}\,\boldsymbol{f}_{ji} \|^2 + \sum_{m,n,n\neq m} \beta_i\,(\boldsymbol{Q}_{mi}\,\boldsymbol{f}_{mi})(\boldsymbol{Q}_{ni}\,\boldsymbol{f}_{ni})\end{aligned} \tag{3.57}$$

We see from comparing the cost functions of Equations (3.57) and (3.37), that we can obtain the channel component separation form of Equation (3.37) if we ignore the cross-channel component error and high-pass filtered terms of Equation (3.57):

$$\sum_{m,n,n\neq m} (\boldsymbol{f}_{mi} - \boldsymbol{G}_{mi}\boldsymbol{y}_m)(\boldsymbol{f}_{ni} - \boldsymbol{G}_{ni}\boldsymbol{y}_n) + \sum_{m,n,n\neq m} \beta_i\,(\boldsymbol{Q}_{mi}\,\boldsymbol{f}_{mi})(\boldsymbol{Q}_{ni}\,\boldsymbol{f}_{ni}) \ , \tag{3.58}$$

By ignoring these terms, we are considering each CCC of a color channel to be independent from one another. We note that costly calculations of estimations of the image channel correlations are difficult to determine accurately and lead to solutions that are sensitive to errors in those estimations [93]. The value of the terms of Equation (3.58) will be dependent upon the actual image sensor data collected. Thus,

quantification of the error due to ignoring the terms of Equation (3.58) will be image data dependent. Using the CCC independence approximation, we have the equation:

$$\phi(\mathbf{f}_{i,}\,\beta_i) = \sum_{j=0}^{3} \left|\left| \mathbf{f}_{ji} - \mathbf{G}_{ji}\mathbf{y}_j \right|\right|^2 + \sum_{j=0}^{3} \beta_i \,||\, \mathbf{Q}_{ji}\,\mathbf{f}_{ji} \,||^2 \text{ , or}$$

$$\phi(\mathbf{f}_{i,}\,\beta_i) = \sum_{j=0}^{3} \left\{ \left|\left| \mathbf{f}_{ji} - \mathbf{G}_{ji}\mathbf{y}_j \right|\right|^2 + \beta_i \,||\, \mathbf{Q}_{ji}\,\mathbf{f}_{ji} \,||^2 \right\} \tag{3.59}$$

Further separating Equation (3.59) into the sum of color component *j* of color channel *i*, and allowing β_i to be independent for each channel component (β_{ji}), we can write:

$$\phi(\mathbf{f}_{i,}\,\beta_i) = \sum_{j=0}^{3} \phi(\mathbf{f}_{ji,}\,\beta_{ji}) \text{ ,} \tag{3.60}$$

Now we use the logic that minimizing each $\phi(\mathbf{f}_{ji,}\,\beta_{ji})$ term of the summation of Equation (3.60) independently (with independent regularization parameters β_{ji}) will result in an optimal cost function:

$$\phi(\mathbf{f}_{ji,}\,\beta_{ji}) = ||\, \mathbf{f}_{ji} - \mathbf{G}_{ji}\mathbf{y}_j \,||^2 + \beta_{ji}||\, \mathbf{Q}_{ji}\,\mathbf{f}_{ji} \,||^2 \tag{3.61}$$

It is noted that in the CLS method of [27], each $\mathbf{Q}_{ji}$ term has its out-of-channel coefficients independently scaled based upon the mean signal magnitude of the color channels. This corresponds to our method of using independent β_{ji} values for each $\mathbf{Q}_{ji}$, where each β_{ji} term will scale each Laplacian $\mathbf{Q}_{ji}$ matrix.

Equation (3.61) is then written in the more standard form of:

$$\phi(\mathbf{f}_{ji,}\,\beta_{ji}) = ||\, \mathbf{y}_j - \hat{\mathbf{H}}_{ji}\,\mathbf{f}_{ji} \,||^2 + \beta_{ji}||\, \mathbf{Q}_{ji}\,\mathbf{f}_{ji} \,||^2 \text{ ,} \tag{3.62}$$

which is used in the Section 3.4.2.1 in the development of a regularization solution form for CCC terms. Equation (3.62) is simplified further in Section 3.4.2.2 by extracting the local scalar pixel value from the vector/matrix form of the equation, resulting in a pixel correction solution that will optimize the local low spatial frequency SNR of each corrected pixel.

From this investigation of the separation set of CCC cost functions, we see that we will have weakened optimization in our solution due to the two simplifying approximations:

1) The sum of the separately minimized color component cost function terms will be the minimum of the sum of the cost function terms.
2) We can neglect the correlation of the errors between different CCC components ($[\mathbf{f}_{mi} - \mathbf{G}_{mi}\mathbf{y}_m][\mathbf{f}_{ni} - \mathbf{G}_{ni}\mathbf{y}_n]$, for $m \neq n$), as well as neglecting the correlation between the different high-pass filtered color components themselves ($[\mathbf{Q}_{mi}\ \mathbf{f}_{mi}][\mathbf{Q}_{ni}\ \mathbf{f}_{ni}]$, for $m \neq n$). Thus, we assume that the sum of the products terms between different CCCs will be negligible compared to the squared same CCC terms (we drop the terms of Equation (3.58)).

In [27], Galatsanos and Katsaggelos apply their method using 3 channels, whereas we use 4 color channels. Our approach will correct for the difference between the even and odd green channels, which can lead to highly visible fixed pattern noise. Additionally, Galatsanos and Katsaggelos only use 7 non-zero coefficients in total for the **H** and **Q** matrices of each color channel. For each color channel only 1 coefficient is used to represent the cross-talk to each of the other color channels. In our approach, we use 25 non-zero coefficients total for the **H** and **Q** matrices of each color channel. For each color channel, from 4 to 6 coefficients are used to represent the cross-talk to each of the other color channels. 9 coefficients are used for the in-channel matrices. [27] uses the relative magnitude ratios of the color channels to determine the values of the cross-

channel coefficients in the regularization matrices (**Q**). We compare the performance of the ST and CLS methods of [27] with our proposed method in Section 3.5.

3.4.2 Derivation of Local Pixel Cost Function and SNR Optimization

3.4.2.1 Local Pixel Regularization Solution Form for CCC

Regularization methods, such as [26], often use the global minimization of the MSE as a criterion to determine the optimal global regularization parameter (β). We instead use the maximization of the local pixel SNR as a criterion to determine the optimal locally adaptive regularization parameter. The use of local adaptivity is driven by the HVS's sensitivity to local pixel values [7], [19], [56], [73]. In this section, we derive the local pixel form of the cost function and its solution, with many of the equations illustrated in Figure 3.9.

In Section 3.4.1 we derived the CCC form of the cost function for our Bayer cross-talk problem (see Equation (3.62)). The estimated regularization pixel signal solution for the cost function of Equation (3.62) is given by the equation:

$$\hat{\boldsymbol{f}}_{ji} = \{\hat{\boldsymbol{H}}_{ji}^T \hat{\boldsymbol{H}}_{ji} + \beta_{ji} \boldsymbol{Q}_{ji}^T \boldsymbol{Q}_{ji}\}^{-1} \hat{\boldsymbol{H}}_{ji}^T \boldsymbol{y}_j \tag{3.63}$$

It is noted that Equation (3.63) is similar to the MAP cost function, except that the covariance matrix **C** is not included. We can write Equation (3.63) in local pixel form for the k^{th} element of $\hat{\mathbf{f}}_{ji}$. First, we rewrite Equation (3.63) as:

$$\hat{\boldsymbol{f}}_{ji} = \boldsymbol{W}_{ji}(\beta_{ji})\, \boldsymbol{y}_j \,, \tag{3.64}$$

where:

$$\boldsymbol{W}_{ji}(\beta_{ji}) = \{\hat{\boldsymbol{H}}_{ji}^{T}\hat{\boldsymbol{H}}_{ji} + \beta_{ji}\boldsymbol{Q}_{ji}^{T}\boldsymbol{Q}_{ji}\}^{-1}\,\hat{\boldsymbol{H}}_{ji}^{T} \quad (m\times m \text{ matrix}) \tag{3.65}$$

Then the scalar estimate of k^{th} element of vector $\hat{\mathbf{f}}_{ji}$ ($\hat{f}_{jik}$, the *ji* component of the k^{th} pixel) can by written as the dot product of the k^{th} row of $\mathbf{W}_{ji}(\beta_{ji})$ and $\mathbf{y}_j$:

$$\hat{f}_{jik} = \boldsymbol{w}_{jik}(\beta_{jik})\,\boldsymbol{y}_j\,, \tag{3.66}$$

where $\mathbf{w}_{jik}(\beta_{jik})$ is a 1×m row vector (the k^{th} row of $\mathbf{W}_{ji}(\beta_{ji})$):

$$\boldsymbol{w}_{jik}(\beta_{jik}) = \boldsymbol{k}\,\{\hat{\boldsymbol{H}}_{ji}^{T}\hat{\boldsymbol{H}}_{ji} + \beta_{ji}\boldsymbol{Q}_{ji}^{T}\boldsymbol{Q}_{ji}\}^{-1}\,\hat{\boldsymbol{H}}_{ji}^{T}\,, \tag{3.67}$$

and **k** is a 1×m vector that has all zero terms except at the k^{th} position where it is 1. We note in Equation (3.66) that $\mathbf{w}_{jik}(\beta_{jik})$ will be a function of the local pixel *k* due entirely to the regularization term β_{jik} (which is a function of $\mathbf{y}_j$), otherwise it would not vary for the CCC *ji*.

Equation (3.66) gives the reconstructed pixel value at location *k* (a scalar). The regularization parameter β_{jik} can vary for each row of the m×m matrix $\mathbf{W}_{ji}(\beta_{ji})$. Allowing β_{jik} to vary for each element of $\hat{\mathbf{f}}_{ji}$ will give us a local pixel optimization. Equations (3.64) and (3.66) are illustrated in Figure 3.9.

3.4.2.1.1 Discussion of Local Pixel Regularization Form

The extent of the blurring matrices is small, and is typically within a 5x5 pixel area, as shown in Figure 3.3. In Equations (3.66) and (3.67), we see that as β_{jik} approaches zero (indicative of a low noise situation), the corrected local signal estimate f_{jik} approaches the naïve (inverse) solution (f^{+}_{jik}). As β_{jik} approaches infinity (suggesting a very high noise situation), the corrected local signal estimate f_{jik} approaches the zero solution. However,

due to the limited extent of the image (fixed, finite size), the impulse response of the blurring filters cannot have boundaries that extend to infinity, and the value of β_{jik} cannot approach infinity.

The stacked vector-matrix form of regularization solution can also be written in terms of convolution solution. Using the block circulant properties of the blurring and regularization matrices, we can apply the DFT to write the solution as local extent matrix. Since the blurring cross-talk matrices operate over a 5-by-5 pixel area, the CLS regularization matrix correction will also operate over the same limited extent 5-by-5 pixel area. Thus, we can write Equation (3.66) using matrices defined over the local pixel *k* 5-by-5 pixel area. This corresponds to the non-zero coefficients in the matrix and vectors of Figure 3.9.

3.4.2.2 Optimal Regularization Parameter Pixel SNR Solution

3.4.2.2.1 Discussion of the SNR Regularization Parameter Approach

We wish to derive a pixel correction solution that will optimize the local low spatial frequency SNR of each corrected pixel. We will apply the maximization of the local pixel SNR as our constraint applied to the CLS regularization problem. In many of the existing regularization solution methods, the global image noise is used to determine the regularization parameter. We define the pixel SNR as the estimated pixel magnitude value divided by the square root of the variance of the total pixel noise (total error in signal value). The SNR is a relative value, which matches the HVS's sensitivity better than using noise values.

The derivation of the reconstructed pixel value is developed using a CLS regularization method. The direct maximization of the local mean SNR with respect to a regularization parameter requires knowledge of the original image data (**f**). Since this data is not available, a predicted method, based upon an estimate of the local blurred SNR (defined as SNR_{jik_m}) is used. We use the local mean of the actual pixel values together with noise characterization models (see Section 2.3.1 and Appendix B) to calculate the local mean SNR estimate. The reconstructed local pixel SNR equation, which must be maximized, is derived and shown in Equation (3.81).

The circulant matrices $\hat{\mathbf{H}}_{ji}^T\hat{\mathbf{H}}_{ji}$ and $\mathbf{Q}_{ji}^T\mathbf{Q}_{ji}$ can be diagonalized with the use of the 2-D DFT [5]. The eigenvalues of each of the 16 CCC blurring filters ($\hat{\mathbf{H}}_{ji}^T\hat{\mathbf{H}}_{ji}$) and the 16 2-D Laplacian regularization filters ($\mathbf{Q}_{ji}^T\mathbf{Q}_{ji}$) are listed in Tables 3.1 and 3.2, respectively. Each CCC requires a different 2-D Laplacian regularization operator that is applied to the proper pixels within the Bayer color pattern (refer to Figure 3.8). Since the extent of the blurring and regularization matrices is small, we have a maximum of 5 eigenvalues for matrix products $\hat{\mathbf{H}}_{ji}^T\hat{\mathbf{H}}_{ji}$ ($\hat{\mathbf{H}}_{ji}$ is sparse) and $\mathbf{Q}_{ji}^T\mathbf{Q}_{ji}$ (N_p=5, N_q=5, as shown in Tables 3.1 and 3.2).

We can write the square of the estimated value of the corrected pixel ($\hat{f}_{jik}^2$) from Equation (3.66) with $\mathbf{w}_{jik}(\beta_{jik})$ written for the local pixel *k*, which uses local $\hat{\mathbf{H}}_{ji}^T\hat{\mathbf{H}}_{ji}$ and $\mathbf{Q}_{ji}^T\mathbf{Q}_{ji}$ matrices information. Since the extent of the blurring and regularization matrices is small, only the small local area of pixel values of $\mathbf{f}_{ji}$ will affect the value of $\hat{f}_{jik}$. As was shown in Figure 3.9, we can take the non-zero coefficients from the large global matrix as shown in the figure to construct our small, local extent matrix for each CCC. For our 5x5 local pixel neighborhood extent, we will have between 4 and 9 pixels with which to

operate. We can also use the DFT applied to the convolution form of the problem to construct the local convolution filters, which can then be used to construct the local matrix.

3.4.2.2.2 Derivation of Local Regularized Pixel Estimate

Using the assumptions of local blurring [24], elements in the local extent of pixel *k* of the vector $\mathbf{y}_j$ will often approach being constant (refer to Figures 3.7 and 3.9). In determining the best local value of the regularization parameter to use, we will use the local mean value of the pixels in the neighborhood of pixel *k* to determine the local mean estimate $\hat{f}_{jik\_m}$. The local mean observed channel for pixel *k* is denoted by y_{jk_m}. Since the row vector $\mathbf{w}_{jik}(\beta_{jik})$ will have a limited extent, defined as N_f pixels, we can write the vector dot product $\mathbf{w}_{jik}(\beta_{jik})\ \mathbf{y}_j$ as:

$$\begin{aligned}
&\boldsymbol{w}_{jik}(\beta_{jik})\,\boldsymbol{y}_j \;=\; \{\,\boldsymbol{w}_{jik}(\beta_{jik})\,\}_{1xN_f}\,\{\,\boldsymbol{y}_{jk}\,\}_{N_f x1}\,,\\
&\boldsymbol{w}_{jik}(\beta_{jik})\,\boldsymbol{y}_j \;\approx\; \{\,\boldsymbol{w}_{jik}(\beta_{jik})\,\}_{1xN_f}\;\{\,y_{jk_m}\;\; y_{jk_m}\;\; y_{jk_m}\ldots y_{jk_m}\,\}^T_{N_f x1}\,,\\
&\boldsymbol{w}_{jik}(\beta_{jik})\,\boldsymbol{y}_j \;=\; y_{jk_m}\,\{\,\boldsymbol{w}_{jik}(\beta_{jik})\,\}_{1xN_f}\,\{1\ 1\ \ldots\ 1\}^T_{N_f x1} \qquad (3.68)
\end{aligned}$$

Thus, the term y_{jk_m} can then be moved outside of the summation resulting from the dot product of the row vector and the column vector terms of Equation (3.68). Since local averaging is used for the y_{jk_m} value, noise suppression of the data results, improving the accuracy of our estimation. Then we can write:

$$\begin{aligned}
&\hat{f}_{jik_m}{}^2 = \{\,\boldsymbol{w}_{jik}(\beta_{jik})\,\boldsymbol{y}_j\,\}^2\,,\\
&\hat{f}_{jik_m}{}^2 = [\,y_{jk_m}\,\{\,\boldsymbol{w}_{jik}(\beta_{jik})\,\}_{1xN_f}\,\{1\ 1\ \ldots\ 1\}^T_{N_f x1}\,]^2\,,\\
&\hat{f}_{jik_m}{}^2 = y_{jk_m}{}^2\,[\,\{\,\boldsymbol{k}\,\{\hat{\boldsymbol{H}}_{ji}{}^T\hat{\boldsymbol{H}}_{ji} + \beta_{ji}\boldsymbol{Q}_{ji}{}^T\boldsymbol{Q}_{ji}\}^{-1}\,\hat{\boldsymbol{H}}_{ji}{}^T\,\}_{1xN_f}\,\{1\ 1\ \ldots\ 1\}^T_{N_f x1}\,]^2\,,
\end{aligned}$$

$$\hat{f}_{jik\_m}{}^2 = y_{jk\_m}{}^2 \left\{ \sum_{p=1}^{N_f} w_{jip}(\beta_{jik}) \right\}^2 , \qquad (3.69)$$

over the local area of pixel *k*. The vector $\mathbf{w}_{jik}$ has scalar values (w_{jip}) for index p equal from 1 to N_f,. From the limited extent of the blurring, N_f will typically be less than or equal to 9 for each color component-to-color component blurring filter. It is noted that when the regularization parameter β_{jik} is set to zero, the estimated value of the mean corrected pixel ($\hat{f}_{jik\_m}$) from Equation (3.69) will be the naïve, inverse filtering, or Maximum Likelihood (ML) solution (denoted by $f^{+}_{jik\_m}$). The ML estimate becomes the least squares method for Gaussian likelihood functions when the covariance matrix is taken as the identity matrix.

3.4.2.2.3 Derivation of Local Regularized Pixel SNR Estimate

We define the corrected mean square error (MSE) of a scalar pixel as being composed of two parts: signal error due to noise in the original signal (noise variance error, which can result from noise being amplified by the correction process), and signal error due to blurring (bias error, which can result from under-correction used to avoid noise amplification). The bias error is the difference between the true pixel value and the mean of possible estimates. The variance error is the measure of the spread of estimates (due to noise) about the mean of possible estimates. Defining the scalar MSE as the sum of these two error sources is well established [26]:

$$\check{n}_{jik}{}^2 = MSE = E[e_{jik}{}^2] = E[\{f_{jik} - \hat{f}_{jik}\}^2] ,$$

$$\check{n}_{jik}{}^2 = bias\{f_{jik}, \hat{f}_{jik}\}^2 + var\{\hat{f}_{jik}\} ,$$

$$\check{n}_{jik}{}^2 = \{ f_{jik} - E[\hat{f}_{jik}] \}^2 + E[\{\hat{f}_{jik} - E[\hat{f}_{jik}] \}^2] \qquad (3.70)$$

The 'corrected' scalar local pixel error (or the total MSE of the estimated local k^{th} pixel value $\hat{f}_{jik}$) for the regularization method can then be derived from the local bias and variance errors [22], [34]. Using Equations (3.67) and (3.69), and using $\hat{f}_{jik\_m}$ for $\hat{f}_{jik}$ since we are using the local mean SNR constraint, the local mean bias is found from:

$$bias\{f_{jik}, \hat{f}_{jik}\} = f_{jik} - E[\, y_{jk\_m} \{ \boldsymbol{k} \{\hat{\boldsymbol{H}}_{ji}^T \hat{\boldsymbol{H}}_{ji} + \beta_{ji} \boldsymbol{Q}_{ji}^T \boldsymbol{Q}_{ji}\}^{-1} \hat{\boldsymbol{H}}_{ji}^T \}_{1xN_f} \{1\ 1\ \ldots\ 1\}^T_{N_f x1} \,]$$

$$bias\{f_{jik}, \hat{f}_{jik}\} = f_{jik} - y_{jk\_m} \Big\{ \sum_{p=1}^{N_f} w_{jip}(\beta_{jik}) \Big\} \tag{3.71}$$

Since we do not know the value of the true pixel value f_{jik} (or f_{jik_m}), and since for the bias we want to look at the non-random noise error, we will use the naïve local mean estimate ($f^+_{jik\_m}$) for f_{jik}. The naïve solution will be the value of $\hat{f}_{jik\_m}$ (from Equation (3.69)) when β_{jik} is set to zero. The naïve local mean estimate is based upon our observable (known) data (y_{jk_m}). Equation (3.71) can then be written to give us the estimate (prediction) of the scalar corrected local mean pixel bias as:

$$\begin{aligned} bias\{f_{jik}, \hat{f}_{jik}\} = \;& y_{jk\_m} [\, \boldsymbol{k} \{\hat{\boldsymbol{H}}_{ji}^T \hat{\boldsymbol{H}}_{ji}\}^{-1} \hat{\boldsymbol{H}}_{ji}^T \,]_{1xN_f} \{1\ 1\ \ldots\ 1\}^T_{N_f x1} - \\ & y_{jk\_m} [\, \boldsymbol{k} \{\hat{\boldsymbol{H}}_{ji}^T \hat{\boldsymbol{H}}_{ji} + \beta_{ji} \boldsymbol{Q}_{ji}^T \boldsymbol{Q}_{ji}\}^{-1} \hat{\boldsymbol{H}}_{ji}^T \,]_{1xN_f} \{1\ 1\ \ldots\ 1\}^T_{N_f x1} , \\ bias\{f_{jik}, \hat{f}_{jik}\} = \;& y_{jk\_m} \{ \boldsymbol{v}_{jik}(\beta_{jik}) \}_{1xN_f} \{1\ 1\ \ldots\ 1\}^T_{N_f x1} , \\ bias\{f_{jik}, \hat{f}_{jik}\} = \;& y_{jk\_m} \Big\{ \sum_{p=1}^{N_f} v_{jip}(\beta_{jik}) \Big\} \end{aligned} \tag{3.72}$$

where:

$\boldsymbol{v}_{jik}(\beta_{jik})$ is the k^{th} row of the matrix product $\{\hat{\boldsymbol{H}}_{ji}^T\hat{\boldsymbol{H}}_{ji} + \beta_{ji}\boldsymbol{Q}_{ji}^T\boldsymbol{Q}_{ji}\}^{-1}\,\beta_{ji}\boldsymbol{Q}_{ji}^T\boldsymbol{Q}_{ji}$:

$$\boldsymbol{v}_{jik}(\beta_{jik}) = \boldsymbol{k}\,[\,\{\hat{\boldsymbol{H}}_{ji}^T\hat{\boldsymbol{H}}_{ji} + \beta_{ji}\boldsymbol{Q}_{ji}^T\boldsymbol{Q}_{ji}\}^{-1}\,\beta_{ji}\boldsymbol{Q}_{ji}^T\boldsymbol{Q}_{ji}\,] \tag{3.73}$$

The vector $\mathbf{v}_{jik}$ has values for index p equal from 1 to N_f, where from the limited extent of the blurring, N_f will typically be less than or equal to 9 for each CCC blurring filter. A bias error will typically result in an under-correction of the color saturation. In particular, when a color component j to i is not fully corrected, there will be an appearance of color de-saturation.

The variance error is found from Equations (3.69) and (3.70) using the additive noise vector $\mathbf{n}_{ji}$:

$$var\{\hat{f}_{jik}\} = E\left[\{\boldsymbol{w}_{jik}(\beta_{jik})\,\boldsymbol{y}_j - E[\boldsymbol{w}_{jik}(\beta_{jik})\,\boldsymbol{y}_j]\}^2\right], \tag{3.74}$$

and with $\boldsymbol{y}_j = \hat{\boldsymbol{H}}_j\boldsymbol{f}_{ji} + \boldsymbol{n}_{ji}$ *and* $\boldsymbol{p}_{jik}(\beta_{jik}) = \boldsymbol{w}_{jik}(\beta_{jik})\,\hat{\boldsymbol{H}}_{ji}$:

$$var\{\hat{f}_{jik}\} = E\left[\{\,\boldsymbol{p}_{jik}(\beta_{jik})\,\boldsymbol{f}_{ji} + \boldsymbol{w}_{jik}(\beta_{jik})\,\boldsymbol{n}_{ji} - E[\boldsymbol{p}_{jik}(\beta_{jik})\,\boldsymbol{f}_{ji} + \boldsymbol{w}_{jik}(\beta_{jik})\,\boldsymbol{n}_{ji}]\}^2\right],$$

$$var\{\hat{f}_{jik}\} = E\left[\{\,\boldsymbol{w}_{jik}(\beta_{jik})\,\boldsymbol{n}_{ji}\}^2\right] \tag{3.75}$$

As was done in Equation (3.68), we will use the local mean value of the pixels in the neighborhood of pixel k, y_{jk_m}, to give us an estimate of the local mean noise, n_{jik_m}. Our sensor characterization noise models are used here. Using this local average signal noise value (n_{jik_m}) and the limited extent of the filters (over N_f pixels), we can write the vector dot product $\mathbf{w}_{jik}(\beta_{jik})\,\mathbf{n}_{ji}$ as:

$$\boldsymbol{w}_{jik}(\beta_{jik})\,\boldsymbol{n}_{ji} = \{\,\boldsymbol{w}_{jik}(\beta_{jik})\,\}_{1xN_f}\,\{\,\boldsymbol{n}_{jik}\,\}_{N_f x1},$$

$$\boldsymbol{w}_{jik}(\beta_{jik})\,\boldsymbol{n}_{ji} = \{\,\boldsymbol{w}_{jik}(\beta_{jik})\,\}_{1xN_f}\,\{n_{jik\_m}\;\; n_{jik\_m}\;\; n_{jik\_m}\ldots n_{jik\_m}\}^T_{N_f x1},$$

$$\boldsymbol{w}_{jik}(\beta_{jik})\,\boldsymbol{n}_{ji} \;=\; n_{jik\_m}\,\{\,\boldsymbol{w}_{jik}(\beta_{jik})\,\}_{1xN_f}\,\{1\ 1\ \ldots\ 1\}^{T}_{N_f x1} \tag{3.76}$$

Now we can use Equations (3.75) and (3.76) to write over the local area of pixel *k*:

$$var\{\hat{f}_{jik}\} = E\left[\{\,\boldsymbol{w}_{jik}(\beta_{jik})\,\boldsymbol{n}_{ji}\,\}^2\right],$$

$$var\{\hat{f}_{jik}\} = E\left[n_{jik\_m}{}^2\,(\{\,\boldsymbol{w}_{jik}(\beta_{jik})\,\}_{1xN_f}\{1\ 1\ \ldots\ 1\}^{T}_{N_f x1})^2\right],$$

$$var\{\hat{f}_{jik}\} = E\left[n_{jik\_m}{}^2\,\{\hat{\boldsymbol{H}}_{ji}{}^{T}\hat{\boldsymbol{H}}_{ji} + \beta_{jik}\boldsymbol{Q}_{ji}{}^{T}\boldsymbol{Q}_{ji}\}^{-2}\,\hat{\boldsymbol{H}}_{ji}{}^{T}\hat{\boldsymbol{H}}_{ji}\right],$$

$$var\{\hat{f}_{jik}\} = \sigma_{jik\_m}{}^2\left\{\sum_{p=1}^{N_f} w_{jip}(\beta_{jik})\right\}^2 \tag{3.77}$$

Again, the vector $\mathbf{w}_{jik}$ has values for *p* equal from 1 to N_f, where from the limited extent of the blurring, N_f will typically be less than or equal to 9 for each color component-to-color component blurring filter. In Equation (3.77), $\sigma_{jik\_m}{}^2$ is the predicted local average noise variance. Its value is predicted based upon the characterization (*a prior*) data relating pixel signal magnitude to noise variance. Combining Equations (3.72) and (3.77), we can write the local mean pixel corrected (regularized) pixel noise estimate as:

$$\check{n}_{jik}{}^2 = y_{jk\_m}{}^2\left\{\sum_{p=1}^{N_f} v_{jip}(\beta_{jik})\right\}^2 + \sigma_{jik\_m}{}^2\left\{\sum_{p=1}^{N_f} w_{jip}(\beta_{jik})\right\}^2 \tag{3.78}$$

Now, using the equations for the regularization estimates of the local signal (Equation (3.69)) and local total noise (Equation (3.78)), we can write the equation for the squared local regularized pixel SNR estimate ($S\check{N}R_{jik}{}^2$), which we wish to maximize:

$$S\check{N}R_{jik}{}^2 \;=\; \hat{f}_{jik}{}^2 \,/\, \check{n}_{jik}{}^2\,,$$

$$\check{SNR}_{jik}^{2} = y_{jk\_m}^{2} \left\{ \sum_{p=1}^{N_f} w_{jip}(\beta_{jik}) \right\}^2 \Big/ \left[y_{jk\_m}^{2} \left\{ \sum_{p=1}^{N_f} v_{jip}(\beta_{jik}) \right\}^2 + \sigma_{jik\_m}^{2} \left\{ \sum_{p=1}^{N_f} w_{jip}(\beta_{jik}) \right\}^2 \right] \quad (3.79)$$

The local blurred mean estimate of the squared SNR at pixel *k* for the color component *j* to color component *i* is defined as:

$$SNR_{jik\_m}^{2} = y_{jk\_m}^{2} / \sigma_{jik\_m}^{2} \quad (3.80)$$

We can then write the squared local regularized pixel SNR equation in terms of the local blurred mean estimate of the squared SNR at pixel *k*:

$$\check{SNR}_{jik}^{2} = SNR_{jik\_m}^{2} \left\{ \sum_{p=1}^{N_f} w_{jip}(\beta_{jik}) \right\}^2 \Big/ \left[SNR_{jik\_m}^{2} \left\{ \sum_{p=1}^{N_f} v_{jip}(\beta_{jik}) \right\}^2 + \left\{ \sum_{p=1}^{N_f} w_{jip}(\beta_{jik}) \right\}^2 \right] \quad (3.81)$$

3.4.2.2.4 Optimization of Local Regularized Pixel SNR

We now can optimize the local regularized pixel SNR by determining the value of β_{jik} that optimizes the above equation for the local blurred estimate of the squared SNR:

$$\beta_{jik} = \max_{\beta} \left[\check{SNR}_{jik}^{2} \right] \quad (3.82)$$

One simple approach to solving this equation is to perform an off-line exhaustive search over β_{jik} for quantized set of local blurred mean estimated SNR values. This is a reasonable approach since the color channel to color channel blurring behavior of CMOS imagers is usually approximately constant across the sensor array and from

sensor to sensor for the same sensor design. The optimal β_{jik} values can then be stored in a look-up table (LUT) for real-time usage. Additionally, the corresponding coefficients for the separated CCC constrained least squares (SCLS) SNR regularized convolution filters can be calculated off-line and stored for real-time use in a camera system. This approach minimizes the required number of calculations that must be performed in a camera system during image processing. In implementing this solution, one would then determine the optimal values of the regularization parameter from Equation (3.81), and store the corresponding correction filter coefficient values w_{jip} in a LUT. In real-time usage, the local mean observed channel y_{jk_m} value, combined with the sensor characterization *a priori* data, gives us the local blurred mean SNR estimate, which then gives us our correction filter coefficients.

The optimal values of the regularization parameter β_{jik} from Equation (3.81) are used in the separated CCC CLS SNR (SCLS SNR) regularization Equation (3.66) at each pixel for each CCC. As we have seen, the optimal β_{jik} value is a function of the CCC blurring filters ($\hat{\mathbf{H}}_{ji}$, dependent upon its stability) and the corresponding local mean pixel color channel (y_{jk_m}) SNR value. The optimal regularization parameter β_{jik} value is then plugged into the local CCC *ji* regularization Equation (3.66). We see that the observed local color channel *j* data ($\mathbf{y}_{jk}$) is used in the SCLS SNR restoration Equation (3.66), and not the local mean data (y_{jk_m}), which was used in determining β_{jik}. This is due to our deterministic constraint being the local mean SNR CCC maximization. During real-time implementation of the SCLS SNR method, we calculate the local mean pixel *k* channel component SNR ($S\check{N}R_{jik}$) from Equation (3.80) and use that value to look up the corresponding coefficients of w_{jip}. Thus, we have as our SCLS SNR regularization equation for pixel *k*:

$$\hat{f}_{jik} = \boldsymbol{w}_{jik}(\beta_{jik})\, \boldsymbol{y}_j \text{ , or}$$

$$\hat{f}_{jik} = \sum_{p=1}^{N_f} \left\{ y_{jkp}\, w_{jip}(\beta_{jik}) \right\} , \tag{3.83}$$

where y_{jkp} are the N_f channel *j* observed pixel values in the local pixel *k* area. Equation (3.83), along with Equations (3.64) and (3.66), are illustrated in Figure 3.9.

If we wish to reduce the number of calculations or the amount of memory required by the SCLS SNR regularization method, we can make a number of simplifications to the algorithm's implementation. The computation of the estimate of the local mean observed channel for pixel *k*, y_{jk_m}, can be simplified by using fewer pixels in the calculation or simply using the value of the observed pixel *k*'s value directly (which would result in using the improper color channel for 3 of the 4 computations). Additionally, we can reduce the size of the input local mean SNR-to-correction filter coefficient LUT. In our standard implementation, we have used one set of coefficients per each integer local SNR estimate. Values for SNR estimates between these integer values are obtained through linear interpolation. We can reduce our memory requirements by using stored coefficients at SNR estimates greater than unity granularity. We can also eliminate the interpolation calculations and simply use the coefficients closest to our SNR estimation. These complexity reductions are examined in the next section.

3.5 Performance Comparisons and Conclusions

3.5.1 Performance Results

The corrected dB SNR improvement restoration performance to algorithm complexity is shown in Figure 3.10 for several Bayer restoration methods. The plot shows the

improvement from the uncorrected pixel data that results for each restoration method. The performance measurements of the methods are averaged over a range of typical operating conditions. Input images with mean SNR pixel values ranging in value from 10 to 40 were used as input to the restoration algorithms. All methods used the same sensor characterization *a priori* data, which included knowledge of the mean pixel cross-talk values. Algorithm complexity was measured by calculating the mean number of operations performed per pixel. Additions, multiplications, and memory look-ups were considered in the complexity measurement, as were the number of iterations required for the non-direct method.

Two heuristic methods commonly used in low cost camera systems are shown in Figure 3.10. These methods are the simple 3*x*3 matrix color correction method and the same method with matrix correction terms that are adaptive to the overall camera operating SNR conditions (refer to Section 3.2.3.2.2 for details). The ideal coefficients derived *a priori* from the cross-talk characterization are used. This *a priori* cross-talk characterization information is shown in Figure 3.3. The 3*x*3 adaptive matrix method also uses a simple median filter to smooth out the green-odd/even pixel mismatches.

The more complex methods of ST and CLS restoration using noise and smoothing constraints are also plotted in Figure 3.10 (refer to Section 3.2.3.2.1 and Appendix C). In order to provide a more challenging testing environment for our SCLS SNR method, the ST, CLS, and SCLS SNR methods used the same noise and SNR characterization data. Additionally, the ST and CLS methods were adjusted to operate on four color channels (R, Ge, Go, B), in a similar manner as our SCLS SNR method. The CLS method has the optimal per color channel regularization parameters used, which are found through an iterative solution. The CLS method is referenced as our ideal, optimal

solution. A trend curve is also shown, which demonstrates the trade-off between restoration SNR performance and algorithm complexity.

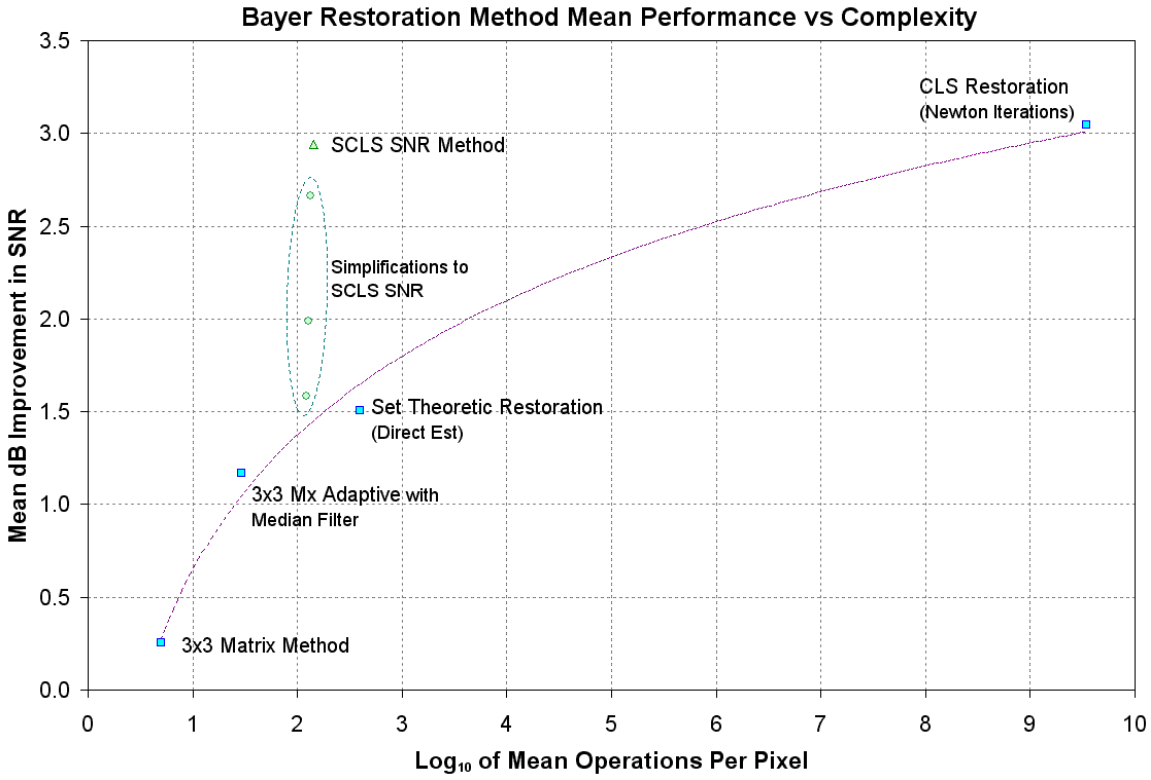

Figure 3.10: Restoration dB SNR improvement performance and complexity comparisons. Performances averaged over operating mean pixel SNR range of input 10 to 40. Improvement measured relative to uncorrected data. ST and CLS iterative restorations are non-spatially adaptive.

The ST and CLS methods both required that ideal regularization matrices be calculated using full image estimates of color channel spatial frequency bounds. As expected, we see a trade-off between high performance and low algorithm complexity. The iterative method required in the CLS solution to determine the regularization parameters significantly increases the number of operations performed. At each iteration, the Jacobian must be calculated. Our goal was to derive a lower complexity restoration algorithm that would provide restoration performance better than heuristic methods

currently implemented in low cost camera systems. From the data points for our SCLS SNR method provided in the plot, we see that we have met this goal.

Several SCLS SNR method data points are shown in Figure 3.10. These correspond to our baseline solution, as well as to some algorithm simplifications. These simplifications lead to lower algorithm complexity, due to fewer calculations and less memory requirements. We have tested a simplified SNR estimation method, where instead of using the local mean estimations (y_{jk_m} and σ_{jik_m} in Equation (3.80)), we use the target pixels SNR estimate. For the cross-channel corrections, this estimate does not use the proper pixel channel SNR values, but is less complex to implement. Additionally, the mapping from the SNR estimate to the regularization parameter value (or directly to the convolution matrix correction coefficients) is simplified by using a coarser LUT. This results in less memory required and faster processing. Our baseline LUT used one set of correction coefficients per each integer value of the input SNR estimate. Values of the coefficients for intermediate SNR values (non integer) were found through simple linear interpolation. The coarser LUTs used input SNR increments of 4, 8, and 10 instead of 1, and no interpolation.

The input mean SNR operating condition versus the output SNR dB improvement (after correction) is shown in Figure 3.11. The same five methods from Figure 3.10 are compared here. The range of mean input SNR values represents the extended range that a low cost camera system would expect to experience. The input and output SNR values are calculated as the mean of all of the pixel SNR values in our test image.

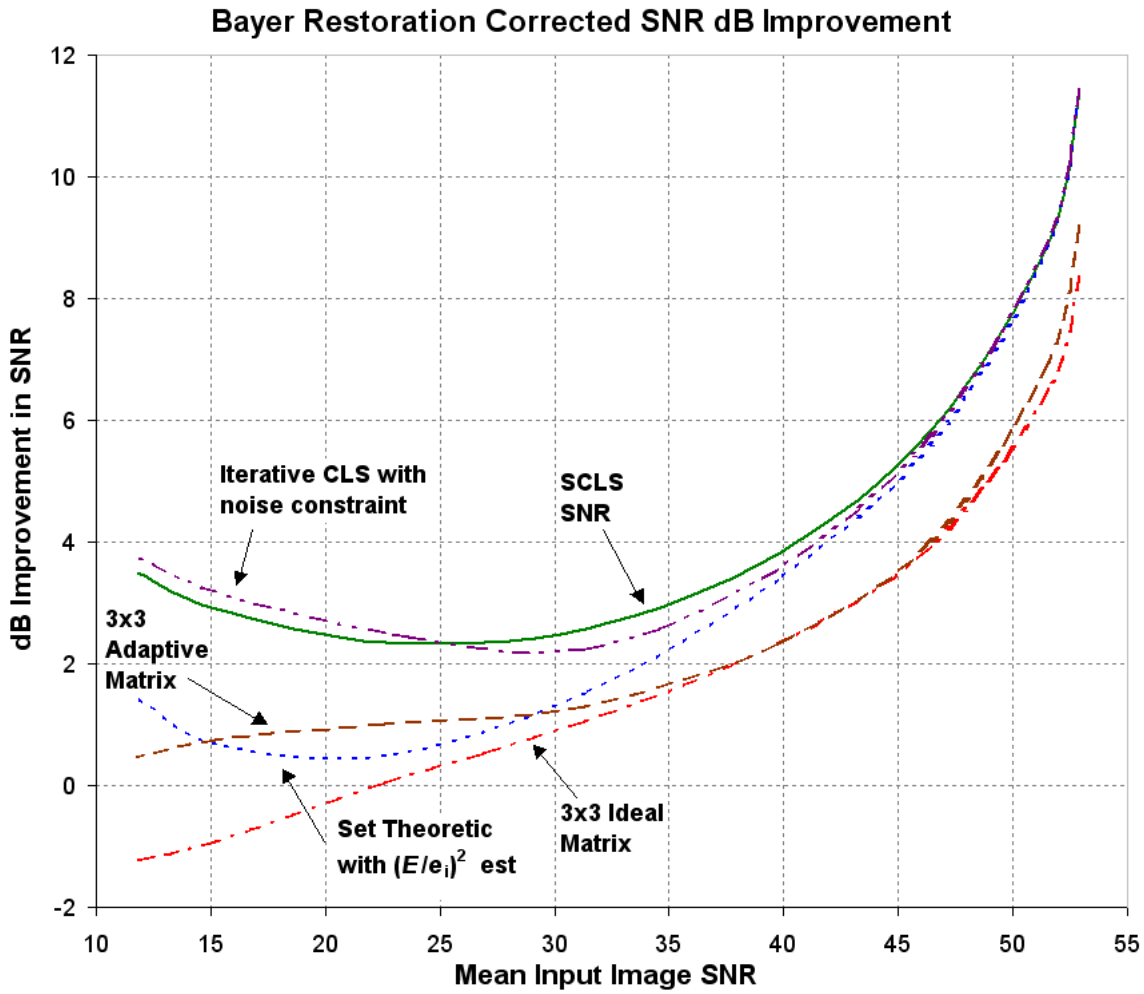

Figure 3.11: Corrected dB SNR improvements as a function of input image SNR. SNR values are mean of all of the image pixels.

The performance plot shows that applying the ideal full 3x3 matrix correction limits output SNR at low input SNR due to noise amplification, while it limits output SNR at high input SNR due to its inability to fully correct the spatial color-dependent blurring. The adaptive 3*x*3 matrix correction method shown here uses a median filter to reduce the fixed-pattern noise (FPN) created by the green-odd/even pixel cross-talk behavior.

All three of the regularization methods shown (ST, CLS with noise constraint and optimal regularization parameters, and SCLS SNR methods) obtain similar performance at high input SNR values. This is due to the regularization parameters approaching zero as the

input mean pixel SNR value become large (or, similarly, the input noise values approach zero) for all three methods. As the input SNR values are reduced, we see that the optimally, iteratively obtained, regularization parameters of the CLS method result in the optimal performance. The performance of the ST method is limited by the accuracy of the estimations of the global signal energy and high frequency content (as well as the noise estimations). As mentioned, all three regularization methods used the same noise and SNR characterization data. The SCLS SNR method was able to outperform the ST method, as well as the heuristic methods, by utilizing variable local SNR data and separating each CCC correction. Accurate regularization parameters were found from the characterization based local mean SNR values.

The use of separate CCC restoration based on local pixel SNR information accounts for the excellent performance of the SCLS SNR restoration method. As was detailed in Section 3.4.2.2, the optimal value of β_{jik} for Equation (3.81) is found for use in the restoration equation. The optimal β_{jik} value is a function of the CCC blurring filters and the local mean pixel SNR value for that CCC. The optimal β_{jik} values for each CCC as a function of local mean pixel SNR can be calculated and stored in a LUT for real-time use. Additionally, the corresponding coefficients for the SCLS SNR convolution filters can be calculated off-line and stored for real-time use in a camera system. This approach minimizes the required number of calculations that must be performed in a camera system. Using this approach of determining the optimal restoration parameter values, we can generate contour plots displaying the optimal β values as a function of input local mean pixel SNR values for each CCC. In Figures 3.12 through 3.15, we show corrected mean pixel SNR versus input mean pixel SNR and β values plots for blue to green-odd (cross-CCC) and green-odd to green-odd (within-CCC) blurring.

These plots show the benefits of separating the corrected CCCs. This allows each color CCC correction to have the optimal regularization applied in its correction. In general, on-diagonal CCC terms (*i=j*) will have smaller optimal β_{ji} values than off-diagonal CCC terms due to the off-diagonal CCC blurring filters being less stable and more sensitive to noise. This behavior is shown in the plots by contours of the maximum normalized corrected SNR values. The corrected SNR values are normalized to a value of unity across the input SNR range.

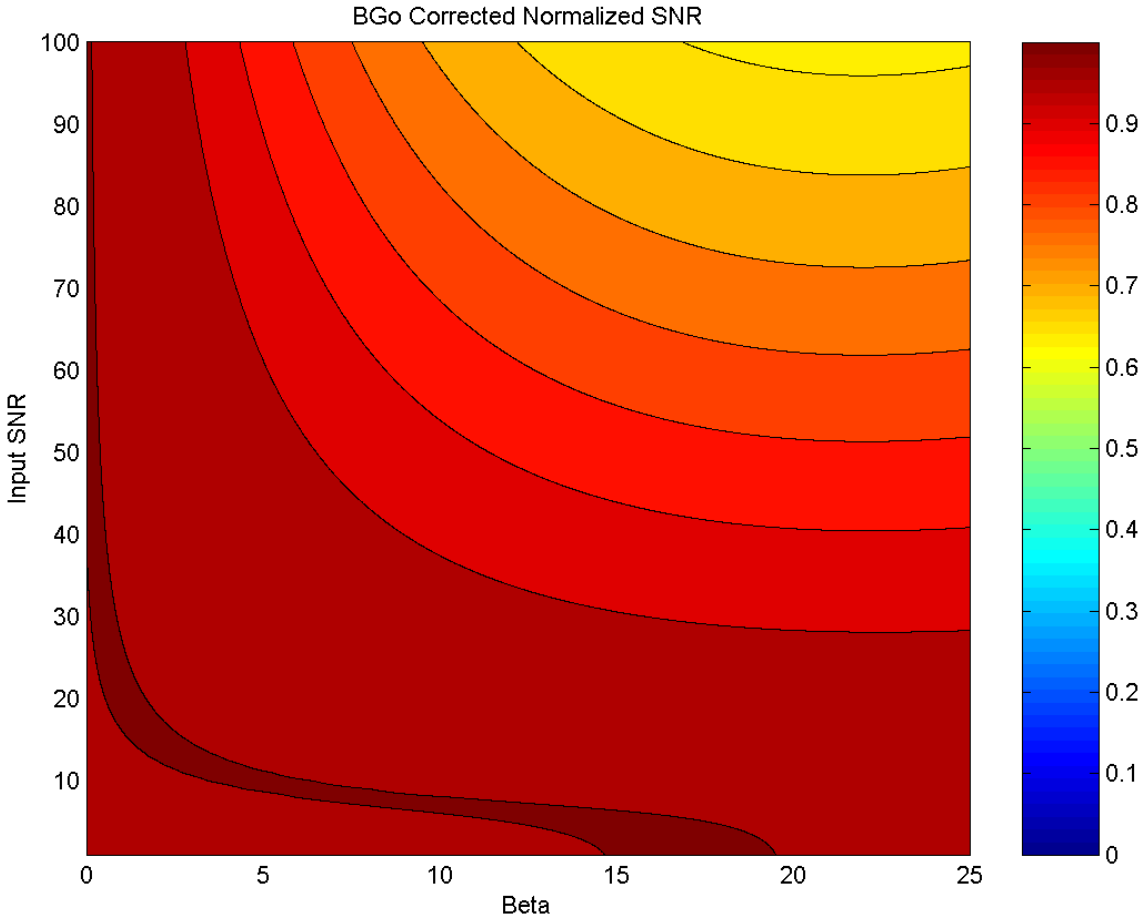

Figure 3.12: CCC *j* to *i* β_{ji} terms (blue to green-odd) as a function of local pixel SNR, with the maximum corrected SNR values per input SNR normalized to unity. Off-diagonal blurring CCC filters often are ill-conditioned, requiring larger optimal β_{ji} terms. The optimal β_{ji} value becomes large (>5) when the input mean pixel SNR value becomes small (<10).

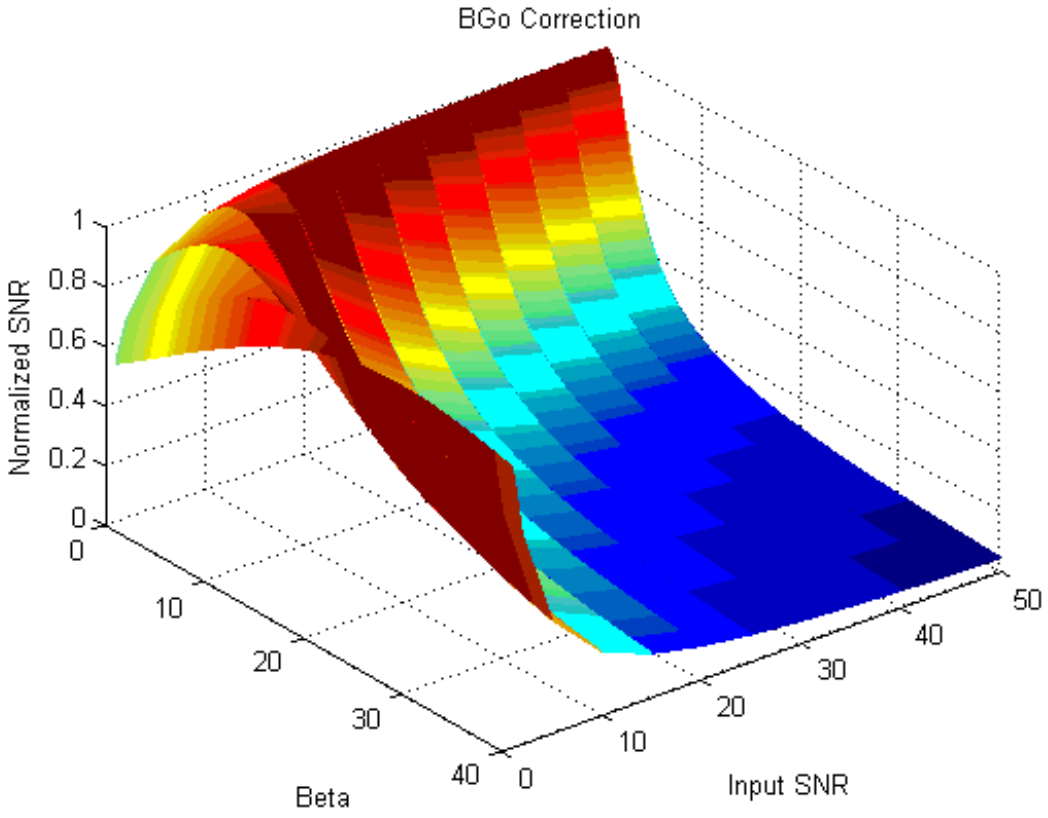

Figure 3.13: 3-D surface plot of CCC *j* to *i* β_{ji} terms (blue to green-odd) as a function of local mean pixel SNR, with the maximum corrected SNR values per input SNR normalized to unity. The optimal β_{ji} value becomes large (>5) when the input mean pixel SNR value becomes small (<10).

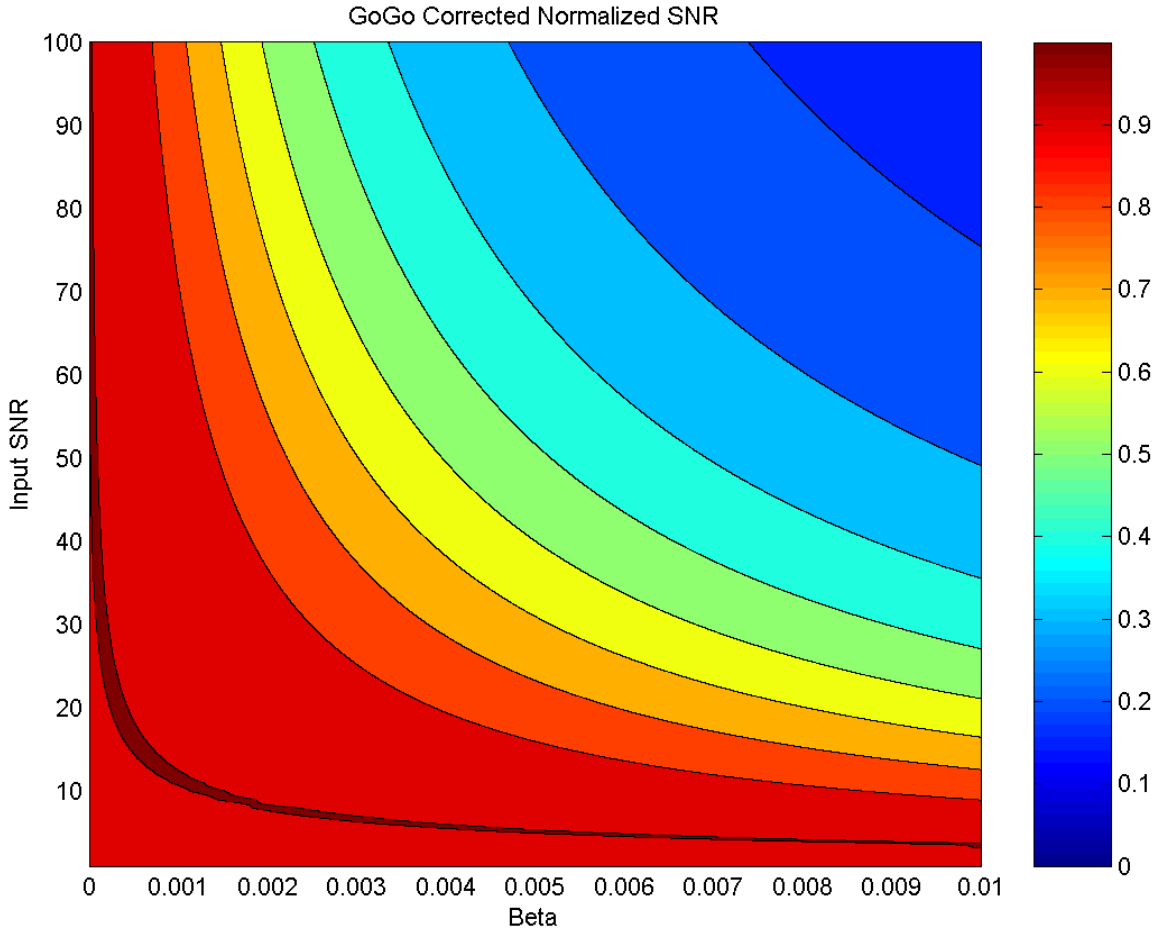

Figure 3.14: CCC *i* to *i* β_{ii} terms (green-odd to green-odd) as a function of local pixel SNR, with the maximum corrected SNR values per input mean SNR normalized to unity. There is a dark red (maximum corrected SNR) region close to the left edge of the plot (at β<0.01). On-diagonal blurring filters are better conditioned, requiring smaller optimal β_{ii} terms. The optimal β_{ii} value remains small (<0.1) even when the input mean pixel SNR value is small (<10), and the optimal β_{ii} value is very small (<0.001) when the input SNR is in its normal operating range (>10).

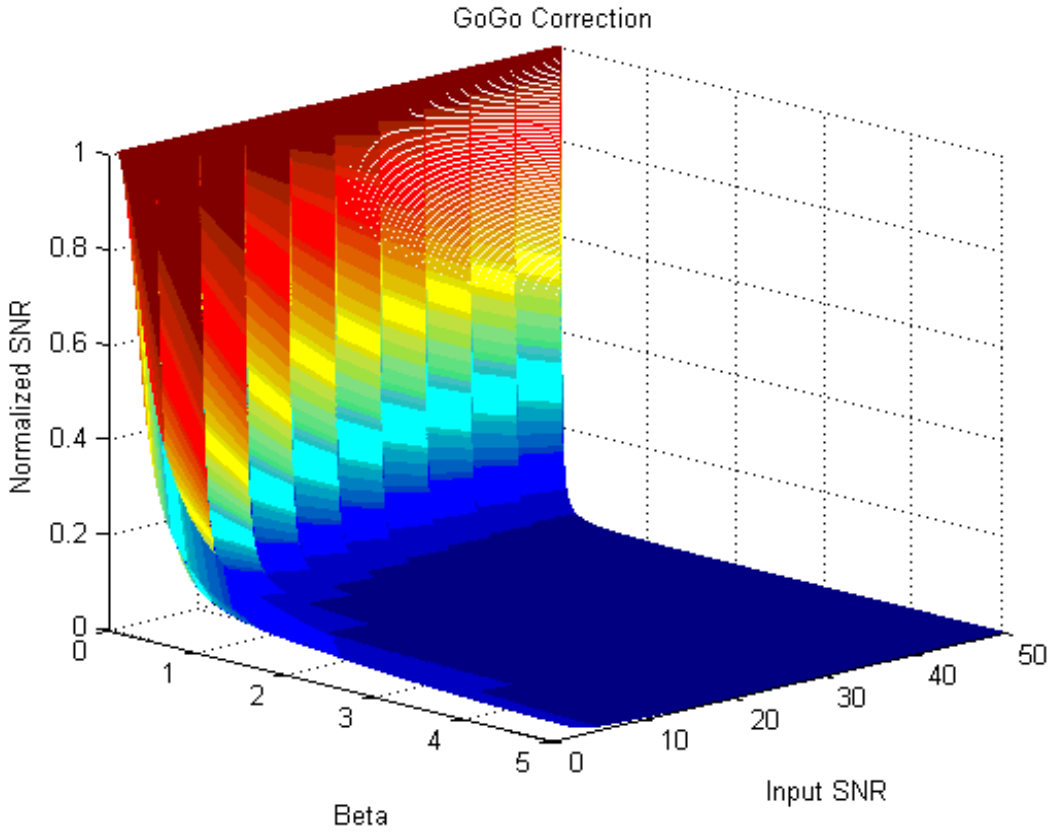

Figure 3.15: 3-D surface plot of CCC *i* to *i* β_{ii} terms (green-odd to green-odd) as a function of local pixel SNR, with the maximum corrected SNR values per input SNR normalized to unity. The optimal β_{ii} value remains small (<0.1) even when the input mean pixel SNR value is small (<10), and the optimal β_{ii} value is very small (<0.001) when the input SNR is in its normal operating range (>10).

The test image used in our analysis is shown in Figure 3.16. This test image possesses all of the features that concern us: saturated colors, low and high spatial frequency data. The range of input mean SNR values was obtained by adjusting input lighting values and exposure times. Additionally, ideal images were created by utilizing multiple frame averaging to remove temporal noise and full fixed pattern noise removal along with ideal cross-talk inversion (with near zero noise).

Figure 3.16: Ideal input test image used for performance analysis.

The cross-talk and noise corruption of the ideal input test image has a detailed section shown in Figure 3.17 for an overall input SNR of 30, which corresponds to an electron to digital count conversion factor (e^-/DN) of 1.4. In Figure 3.18, we show samples of an image cross-talk corrected by the simple 3*x*3 matrix color correction method, the ST method, and our SCLS SNR method. These images show the overall corrected SNR value and the SNR value of the gray square (18% gray). The overall SNR is our metric that we use to measure image correction. It is the average corrected pixel SNR, using the knowledge of the ideal (uncorrupted) pixel values. The 18% gray SNR is the measured flat field SNR of the MacBeth chart 18% reflector gray square. It is a metric commonly used in industry to measure the quality of processed sensor images (refer to

ISO standard 12232-1998E). The three images show that the SCLS SNR method performs better than the other two methods of similar complexity. It should be noted that further processing would typically be performed on the cross-talk restored pixel data. One can view the cross-talk restoration process as the color correction step in the color sensor process (along with the Bayer interpolation step). After the color correction step, one might perform some sort of flat area noise smoothing (such as median filtering) and an edge sharpening filtering. These image processing steps would improve the appearance of the final processed images.

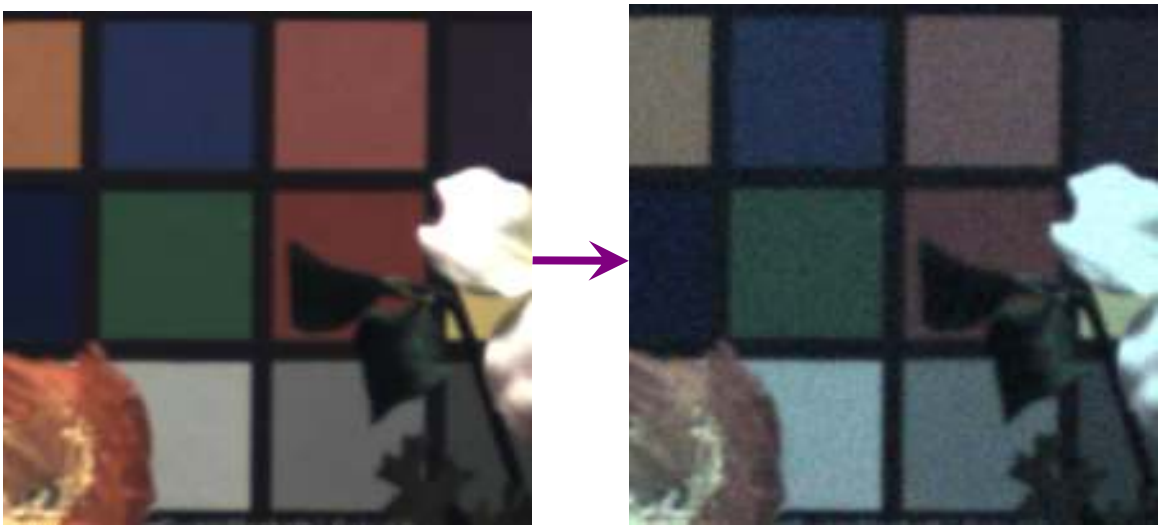

Figure 3.17: Input test image detail section corrupted for conversion factor e-/DN=1.4, Overall SNR=30, 18% Gray SNR=18. Images with any specified SNR value can be constructed using characterization and camera system models.

Figure 3.18: Detail of SNR=30 image section after correction by methods:
Top Left: Optimal 3x3 Matrix, Overall SNR=35, 18% Gray SNR=15,
Top Right: ST, Overall SNR=37, 18% Gray SNR=16,
Bottom: SCLS SNR, Overall SNR=42, 18% Gray SNR=18.

3.5.2 Discussion of Performance and Conclusions

The separate optimization of CCC terms has been shown to be very advantageous for the Bayer cross-talk problem. This is due to the full restoration of within color channel blurring ($j=i$) usually having small noise amplification (small blur matrix condition number), whereas the full restoration of cross color channel blurring ($j\neq i$) often having

large noise amplification (large blur matrix condition number). Although methods such as [27] can scale the **Q** matrices for different CCCs, they cannot simultaneously adjust for the CCC's blurring matrix stabilities and SNR values.

The pixel SNR after correction for within color channel blurring ($j=i$) is more sensitive to bias error, than the pixel SNR for cross color channel blurring ($j\neq i$). This is due to the majority of the correction for the within color channel blurring case being a simple gaining of the target pixel's value. Because of this, the pixel signal divided by pixel noise ratio will have little change as the regularization parameter's value approaches zero. This is also a consequence of the within color channel blurring filters having smaller condition numbers. However, the bias error will increase as regularization parameter's value increases. Correcting the within color channel blurring corresponds to a heuristic white balance correction in a standard camera system, which does not affect the SNR due to the noise variance. Thus, to maximize the pixel SNR due to noise variance and bias error (total noise), a correction approaching the ideal full inverse correction ($\beta_{ii}=0$) is usually required. Since, from a HVS standpoint, the white balance should always be performed, the proposed restoration method's behavior matches the HVS's sensitivities [64], [75], [76], [85]. Existing methods that use the MSE as a metric for calculating the regularization parameter will not produce the optimal value for white balance, since the noise variance will increase with a decreasing regularization parameter value. Even when the bias error is included in the MSE calculation, this will result in too large of a regularization parameter value being calculated.

For the cross color channel blurring ($j\neq i$) case, more independent pixels in the local neighborhood are involved in the correction, leading to a noise amplification situation.

This is a consequence of the cross color channel blurring filters having larger condition numbers. The CCC correction will involve between 4 and 6 pixels in the local 5 by 5 pixel neighborhood. Thus, more blurring, resulting from a greater regularization parameter value ($\beta_{ji}>0$), is often required in order to obtain the maximum corrected pixel SNR. The optimal value of β_{ji} will result from the maximum value of the corrected CCC divided by the total MSE derived as the sum of the corrected noise variance and the corrected bias error. Existing methods that do not take into account bias error will produce regularization parameters that are too large and penalize the saturation correction too much. Additionally, even existing methods that use the total MSE estimate for the regularization calculation do not consider the estimated corrected SNR value. The HVS's sensitivity to the local SNR relationship is not represented well by the MSE. Methods using the MSE metric will find minimum MSE regularization parameter values which attenuate the corrected signal value too much. As a result, from the maximum SNR point of view, they will produce regularization parameters that are too large and overly reduce the saturation correction. From the HVS's sensitivity to local SNR [7], [19], [56], [73], the existing methods using the MSE metric will over smooth the images.

Using our proposed method for a local pixel area with a high SNR for all of the color components, we will apply an ideal inverse filtering correction. This corresponds to an ideal full 3x3 color correction $\mathbf{T_{cc}}$ matrix application in a heuristic camera system, which corrects white balance and saturation. When we have a local pixel area with a low SNR for all of the color components, we will apply close to an ideal inverse filtering correction for the within CCC terms, but a greatly regularized correction to the cross CCC terms. This is similar to a heuristic camera system applying an ideal white balance correction

$\mathbf{T_{WB}}$ matrix with a greatly reduced $\mathbf{T_{Sat}}$ matrix. This separate optimized correction of the CCCs is not possible in the existing methods that use one regularization parameter per channel.

The greatest visual effect of Bayer cross-talk blurring is the de-saturation of color. Since the extent of the blurring is often limited to a local 5 by 5 pixel neighborhood, blurring of the high frequency details of the image will not be as noticeable to the human observer as is the color corruption. Since the Bayer color filter array has different color filtered (CFA) pixels next to one another, there will be significant color blurring for small pixels. Thus, the trade-off between color correction and noise amplification will be the most significant criterion. This criterion leads us to use the local mean SNR estimate as the metric in selecting the optimal regularization parameter. Since the HVS sensitivity to color is greatest for low frequency components [64], [75] (Figure 3.7), the local mean values are best to use in the correction process. As discussed in this thesis, the HVS is also sensitive to relative error or local SNR. Thus, the use of the local average SNR is best to use in the correction of local pixel values and consequently the local color values.

In summary, the advantages of our proposed SCLS SNR method over standard camera correction methods being used are that our method:

1) is spatially adaptive
2) treats each CCC separately and optimally
3) corrects the green odd and even channels (which have different cross-talk characteristics)
4) uses sensor characterization models which define pixel SNR values as a function of pixel signal level
5) is automatically matched to the HVS's SNR sensitivity
6) can be implemented as a simple, direct method

3.5.3 Comparison to Red/Black Ordering

One of the key assumptions and simplifications that we make in our SCLS SNR method is that each CCC is independent from each other. This assumption will not usually be valid, since each color channel is typically not independent from the other color channels. The amount of correlation between color channels changes as a function of spatial location within a picture. The color channel correlation also varies greatly from picture to picture. The greatest correlation between color channels will be between the odd and even green channels of a Bayer CFA imager. This is where the breakdown of the channel independence assumption will be the most severe.

A multigrid method, such as Red-Black Gauss-Seidel, can be used to parallelize computations. In these schemes, a set of points (red points) are updated at one step, and then another set of points (black points) are updated in the next step. For an image, this would be done on a single channel. The two-color (red/black) approach using a 5-point Laplacian can be used to separate the coupling between any two points (red or black points), so that any point can be updated simultaneously. In our application, we assume each plane is independent. Thus, we are not applying a red/black type sub-sampling of a color plane. One important feature of our method is that it is not iterative. Red/black-ordering uses a successive over-relaxation (SOR) type iterative solution, which would not be applicable to our Bayer cross-talk problem due its constraints.

Chapter 4

Conclusions and Future Work

4.1 Conclusions

Sensor characterization data and camera system image processing information were utilized to develop image sensor testing and image quality enhancement methods for commercial CMOS image sensors. The approach we developed was to link system algorithms to the sensor performance characteristics.

In Chapter 2, we presented novel image sensor PRNU testing methods. Monte Carlo and probability model-based simulation approaches were used to create functions which relate measurements of raw block PRNU values to failure rates for particular sensor applications. These methods allow failure rate curves to be constructed for specific sensor operating conditions and image processing settings. Groups of settings can be associated with specific sensor applications. In the development of our methods, we used the idea that different sensor applications will have different requirements for quantization (compression) amounts, acceptable SNR, image processing applied, sensor gain settings, sensor exposure times, and other operating conditions. We also used the concept of acceptable degradation to determine sensor operation based PRNU thresholds. Sensor signal-dependent noise models were used in the process of

determining these thresholds. Using our proposed PRNU testing methodologies, we have shown the potential to increase the yield rate of sensors. A single PRNU measurement per sensor can be used for multiple sensor applications, which increases testing efficiency and reduces overhead cost.

A novel, low complexity pixel cross-talk correction algorithm that can provide restoration performance better than heuristic methods currently implemented in low cost camera systems, was developed in Chapter 3. The use of separate color channel component (CCC) restoration based on local pixel SNR information was primarily responsible for the excellent performance of our CCC separated constrained least squares (SCLS) with local SNR optimization constraint regularization method (SCLS SNR). The optimal value of each CCC regularization parameter was determined to be a function of the CCC blurring filters and the local pixel CCC SNR value. Since there is a wide range in the different CCC blurring filter stability (ill-condition-ness) and in the spatial color channels SNR, the use of this optimization of the local CCC regularization parameter is both appropriate and beneficial. It was shown that the regularization parameter values for each CCC, as a function of local pixel SNR, can be calculated and stored in a LUT. Additionally, the corresponding coefficients for the SCLS SNR convolution filters can be calculated off-line and stored for real-time use in a camera system. This approach minimizes the required number of calculations that must be performed in a camera system during image processing. Cross-talk and signal-dependent noise models, determined from sensor characterization, were utilized in the development of our SCLS SNR method.

4.2 Future Work

4.2.1 PRNU

In order to acquire a better understanding of the applicability of our PRNU testing method, error thresholds and error rates need to be determined for a larger set of sensor applications. A greater set of application requirements, such as data rates (which determine amount of compression), need to be determined and used in the PRNU analysis. Allowable error rates for the greater set of sensor applications should also be found and used in the PRNU distortion analysis. We need more data on the acceptable PRNU block failure rates per sensor. One problem with this is that much of the information is company proprietary. Most importantly, we need to determine quantitatively the yield rate improvement that one could achieve by using our PRNU testing approach.

We may also want to look at the failure rates for particular PRNU block patterns. The spatial distribution of pixel gain factors within a block will determine the spatial frequency PRNU characteristics. This will in turn have an affect on the perceptual distortion of the block image data. Thus, instead of simply measuring a standard deviation or maximum/minimum difference of PRNU, we could also consider the spatial locations of pixel gain variation. During testing, pixel blocks could be grouped into PRNU distribution 'classes', with the allowable distortion based upon the block PRNU class.

4.2.2 Bayer Cross-Talk Correction

The weakened optimization used in our SCLS SNR algorithm requires further analysis. The error resulting from neglecting the correlation between different

CCC components is image dependent, and should be quantified for a representative set of input images to a camera system.

The SCLS SNR algorithm could be combined with the color correction frequency domain method that was developed in [61]. We could extend the SCLS SNR method to be applied within the frequency domain. The algorithm could be applied to individual subbands obtained from a discrete wavelet transform (DWT), or to frequency coefficients from the discrete cosine transform (DCT). This correction method could then be embedded in the compression operations of JPEG or JPEG 2000.

The DCT domain can be used to segment the image frequency components for each sensor color plane. At the same time, we can implement the cross-talk and color correction into the JPEG compression process, similar to the method of Chapter 3. As shown in Figure 4.1, the white balanced (scaled) raw Bayer data for the four-color planes would have the DCT applied to them. For each color plane (R, Ge, Go, B) and each DCT coefficient, in the absence of noise, there exists a set of inverse blurring coefficients that can be applied to best recover the corresponding component of color plane coefficients. The DCT coefficient correction is shown in Figure 4.2. The C_{ijk} coefficients are the optimal inverse blurring coefficients for coefficient *i* spatial frequency and CCC *j* to *k* correction. A method to derive these coefficients from the ideal spatial domain filters would have to be developed. In the presence of noise, we would have to adjust the blurring and color corrections. We could accomplish this by using the scalar terms $K_{ijk\ SNR}$ shown in Figure 4.2. The JPEG compression process can then continue from this point in the standard manner.

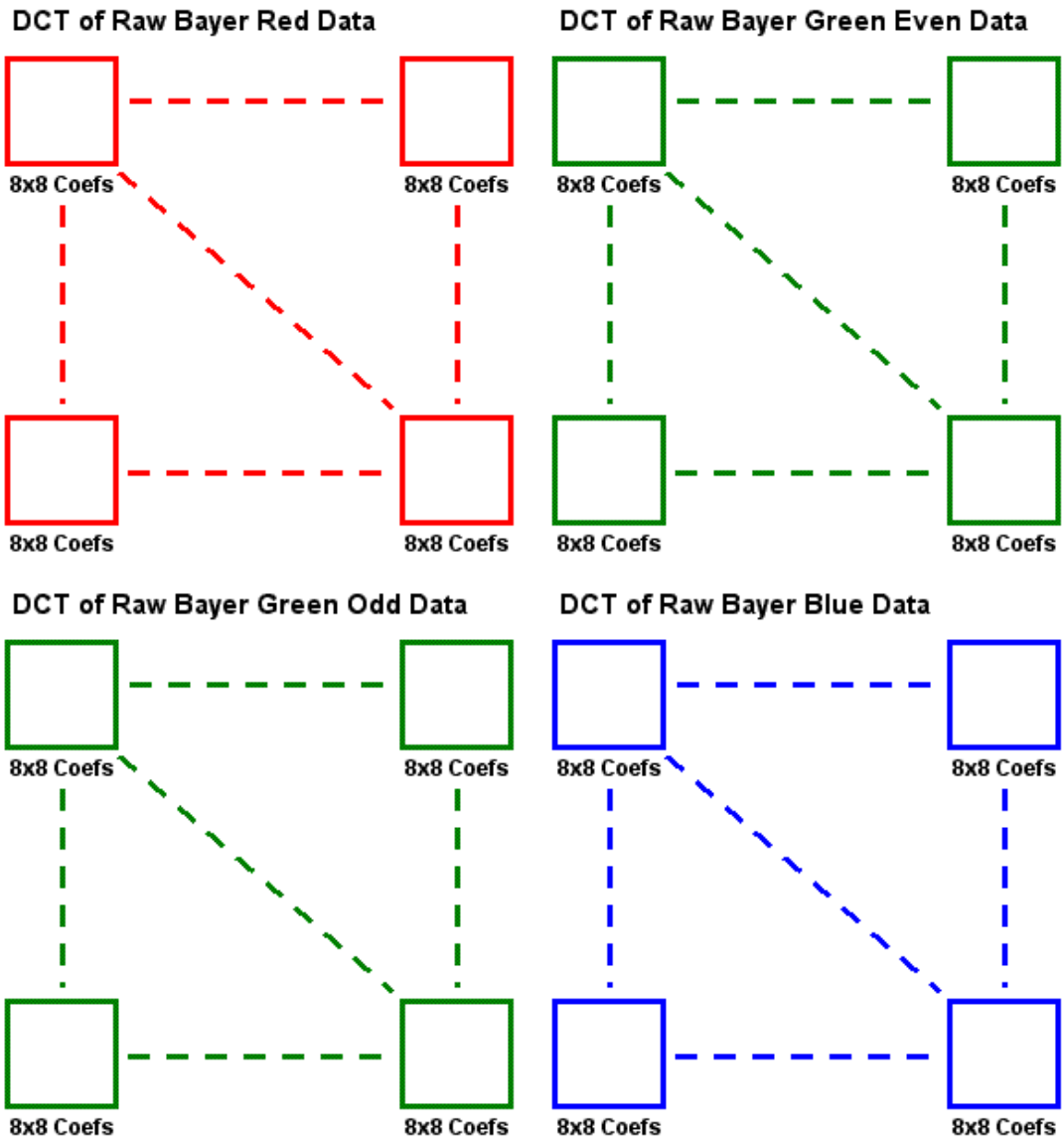

Figure 4.1: DCT coefficients of non-interpolated raw Bayer pixel data.

For each coefficient ik :

$$\square_{ik} = \square \times (C_{irk})(K_{irk\ SNR}) + \square \times (C_{igek})(K_{igek\ SNR}) +$$
$$\square \times (C_{igok})(K_{igok\ SNR}) + \square \times (C_{ibk})(K_{ibk\ SNR})$$

Figure 4.2: Correction of Bayer data in the DCT domain, correction applied to each coefficient *i* within the 8x8 DCT block of color plane *k*.

Bibliography

[1] S. Agwani, S. Domer, et al, “High Performance VGA Resolution Digital Color CMOS Imager”, Proc. SPIE Vol. 3649, pp. 154-164, Sensors, Cameras, and Systems for Scientific/Industrial Applications, Apr. 1999.

[2] J.M.M. Anderson, B.A. Mair, M. Rao, C.-H. Wu, “Weighted Least-Squares Reconstruction Methods for Positron Emission Tomography”, IEEE Trans. Med. Imaging 16(2): 159-165, 1997.

[3] H. Andrews and B. Hunt, Digital Image Restoration, Englewood Cliffs, NJ: Prentice Hall, 1977.

[4] M. Antonini, M. Barlaud, P. Mathieu, L. Daubechies, “Image Coding Using Wavelet Transform”, IEEE Transactions on Image Processing, vol: 1 Issue: 2, pgs. 205 –220, Apr. 1992.

[5] M.R. Banham and A.K. Katsaggelos, “Digital Image Restoration”, IEEE Signal Processing Magazine, pgs 24-41, March 1997.

[6] Y. Bao, and Y. Noyes, “Dorado2 Image Processing Algorithms and System Specifications”, I.C. Processor Spec., Pictos Technologies, Inc, 2003.

[7] P.G.J. Barten, “Contrast Sensitivity of the Human Eye and Its Effects on Image Quality”, SPIE Publications, Vol. PM72, Dec 1999.

[8] B. Benwell, N. O., G. Allen, et Al., “12k 5-mm linescan CCD sensor with 320 MHz data rate”, 2005 IEEE Workshop. on Charge-Coupled Devices and Advanced. Image Sensors, June 10-12, 2005.

[9] A.J. Blanksby and M.J. Loinaz, “Performance Analysis of a Color CMOS Photogate Image Sensor”, IEEE Trans on Electron Devices, Vol 47, Issue 1, pp. 55-64, Jan 2000.

[10] J.T. Buey, “First Results on the Corot CCD Test Bench”, The Third MONS Workshop: Science Preparation and Target Selection, January 24-26, 2000.

[11] Y. Chen, S.M. Guertin, et Al., “A Chip and Pixel Qualification Methodology on Imaging Sensors”, IEEE Reliability Physics Symposium Proc., 42nd Annual, pp435- 439, April 2004.

[12] I.S. Chong, and A. Ortega, “Hardware Testing for Error Tolerant Multimedia compression base on Linear Transforms”, DFT 2005, IEEE, pp. 523 - 531, 3-5 Oct. 2005.

[13] I.S. Chong, H.Y. Cheong, and A. Ortega, “New Quality Metrics for Multimedia Compression Using Faulty Hardware”, Proc. Video Processing and Quality Metrics for Consumer Electronics (VPQM'06), Jan. 2006.

[14] J. Chou, M. Crouse, and M. K. Ramchandran, “A Simple Algorithm for Removing Blocking Artifacts in Block-Transform Coded Images”, IEEE Signal Processing Letters, vol: 5 Issue: 2, pgs. 33–35, Feb. 1998.

[15] Conexant CX1024 Sensor Design and Manufacturing document, A. Dumas, B.C. Hseih, J. Luo, R. Mann.

[16] Conexant CX20450 (SXGA) Sensor Electra-Optical Specification document, S. Bencuya, F. Gunawan, B.C. Hseih, R. Mann, B. McCleary.

[17] Conexant DVGA 20490 Rev A, Sensor Characterization Test Report, R. Kannegundla, R. Mann, B. McCleary.

[18] Conexant DVGA 20490 Sensor Electra-Optical Specification document, S. Bencuya, R. Kannegundla, R. Mann, B. McCleary, E. Stauber.

[19] W.J. Crozier, “On the variability of critical illumination for flicker fusion and intensity discrimination”, Journal of General Physiology, Vol. 19, pp. 503-522, 1935.

[20] A. El Gamal and H. Eltoukhy, “CMOS image sensors”, IEEE, Circuits and Devices Magazine, Vol 21, Issue 3, pp. 6-20, May-June 2005.

[21] Fairchild Imaging, CMOS 1421 Specification Sheet, Rev C, Table 9, 2005.

[22] J.A. Fessler, “Mean and Variance of Implicitly Defined Biased Estimators (such as Penalized Maximum Likelihood): Applications to Tomography”, IEEE Conf. Acoustic Speech Sig. Proc., vol. 4, pp. 2291-2294, 1995.

[23] J.A. Fessler, “Penalized weighted least-squares image reconstruction for positron emission tomography”, IEEE Trans. Med. Imag., 13(2):290-300, Jun. 1994.

[24] J.A. Fessler, W.L. Rogers, “Spatial Resolution Properties of Penalized-Likelihood Image Reconstruction: Space-Invariant Tomographs”, IEEE Transactions on Image Processing , Vol. 5, Issue 9, pp. 1346-1358, 1996.

[25] N.P. Galatsanos and R.T. Chin, “Restoration of Color Images by Multichannel Kalman Filtering”, IEEE Transactions on Signal Processing, Vol. 39, No. 10, Oct 1991.

[26] N.P. Galatsanos, A.K. Katsaggelos, “Methods for Choosing the Regularization Parameter and Estimating the Noise Variance in Image Restoration and Their Relation”, IEEE Transactions on Image Processing, Vol. 1, No. 3, pp. 322-336, July 1992.

[27] N.P. Galatsanos, A.K. Katsaggelos, R.T. Chin, A. Hillery, "Least Squares Restoration of Multi-Channel Images," IEEE Trans. Signal Processing, vol. 39, no. 10, pp. 2222-2236, Oct. 1991.

[28] N.P. Galatsanos, R.T. Chin, “Digital restoration of multichannel images”, IEEE Trans. on Acoustic, Speech and Signal Proc., Vol. 37, No. 3, pp. 415-421, March 1989.

[29] N.P. Galatsanos, R.T. Chin, A.K. Katsaggelos, A. Hillery "Two Methods for Least Squares Multi-Channel Image Restoration," IEEE International Conference on Acoustics, Speech, and Signal Processing, ICASSP-91, Vol.4, pp. 2509-2512, Apr 1991.

[30] D. Gardner, “Taking a Closer Look at Camera Specifications”, Phontoics Spectra, May 2003.

[31] R.C. Gonzales and R.E. Woods, Digital Image Processing, chapter 5, Addison-Wesley Publishing Co., Reading, MA, Sept 1993.

[32] W. Hardin, "CMOS Sensors Offer Vision Designers New Capabilities", Machine Vision Online, April 2004.

[33] B. Hochfelder, “Looking at the Expanding Sensor Market”, Advanced Imaging, May 2008.

[34] A.E. Hoerl and R.W. Kennard, “Ridge regression: Biased estimation for nonorthogonal problems,” Technometrics, vol. 12, no. 1, pp.55-67, 1970.

[35] G.C. Holst “CCD Arrays Cameras and Displays”, SPIE Optical Engineering Press, Bellingham, WA, 2nd edition, 1998.

[36] M.C. Hong, T. Stathakiet, A.K. Katsaggelos, “A Regularized Mixed Norm Multichannel Image Restoration Approach,” Statistical Signal and Array Processing, Ninth IEEE SP Workshop, Sept 1998.

[37] B. Hunt, H. Trussell, “Sectioning techniques for processing signals with signal-dependent noise”, Acoustics, Speech, and Signal Processing, IEEE International Conference on ICASSP, Vol 2, 704- 707May 1977.

[38] H.T. Hytti, “Characterization of digital image noise properties based on RAW data”, Proc. of SPIE and IS&T, vol. 6059, Jan. 2005.

[39] B. Jahne, and H. Haussecker, “Computer Vision and Applications: A Guide for Students and Practitioners ”, Academic Press; May 15, 2000.

[40] J. Janesick, “Dueling Detectors”, SPIE’s oemagazine, Feb. 2002.

[41] J. Janesick, “Lux transfer: Complementary metal oxide semiconductors versus charge-coupled devices,” SPIE, Opt. Eng. 41, pp. 1203-1215, June 2002.

[42] J. Janesick, Scientific Charge-Coupled Devices, chapter 2, SPIE Press, Bellingham, Washington, vol. PM83, 2001.

[43] H.R. Kang, “Color Technology for Electronic Imaging Devices”, chapters 2 & 3, SPIE Optical Engineering Press, Bellingham, Washington, Jan. 1997.

[44] M.G. Kang , “Generalized multichannel image deconvolution approach and its applications”, Optical Engineering, Vol. 37, No. 11, pgs 2953-2964, Nov 1998.

[45] M.G. Kang and A. K. Katsaggelos, "General Choice of the Regularization Functional in Regularized Image Restoration," IEEE Trans. Image Processing, Vol. 4, No. 5, pp. 594-602, May 1995.

[46] N.B. Karayiannis, A. N. Venetsanopoulos, “Regularization theory in image restoration--the stabilizing functional approach”, IEEE Transactions on Acoustics, Speech, and Signal Processing, Vol. 38, No. 7, pp.1155-1179, July 1990.

[47] A.K. Katsaggelos, “A General Formulation of Adaptive Iterative Image Restoration Algorithms,” Proc. 1986 Conf. Inf. Sciences and Systems, pp. 42-47, March 1986.

[48] A.K. Katsaggelos, J. Biemond, R.W. Schafer, R.M. Mersereau, “A Regularized Iterative Image Restoration Algorithm”, IEEE Transactions on Signal Processing, Vol. 39, No. 4, pgs 914-929, April 1991.

[49] D.T. Kuan, A.A. Sawchuk, T.C. Strand, P. Chavel, “Adaptive noise smoothing filter for images with signal-dependent noise”, IEEE Trans. Pattern Anal. Machine Intell., vol. PAMI-7, no. 2, pgs. 165–177, March 1985.

[50] D.T. Kuan, A.A. Sawchuk, T.C. Strand, P. Chavel, “Nonstationary 2-D Recursive Restoration of Images with Signal-Dependent Noise”, IEEE International Conf on Acoustics, Speech and Signal Processing ICASSP, Vol. 9, pp. 84- 87, Mar 1984.

[51] M.L. La Haye, C. Jung, et al., “Fault Tolerant Active Pixel Sensors in 0.18 and 0.35 Micron Technologies”, IEEE, Defect and Fault-Tolerance in VLSI Systems, 2006.

[52] F.M. Li, and Arokia Nathan, “CCD Image Sensors in Deep-ultraviolet”, Springer Berlin Heidelberg, 2005.

[53] Q. Li, E. Asma, J. Qi, J.R. Bading, RM. Leahy, “Accurate estimation of the Fisher information matrix for the PET image reconstruction problem”, IEEE Trans Med Imaging, Vol. 23, No. 9, pp.1057-1064, Sept 2004.

[54] W. Li, P. Ogunbona, Y. Su, I. Kharitonenko, “Modelling of Color Cross-Talk in CMOS Image Sensors”, IEEE International Conference on Acoustics, Speech, and Signal Processing, Vol 4, pgs 3576-3579, May 2002.

[55] C.M. Lo, A.A Sawchuk, “Nonlinear restoration of filtered images with Poisson noise”, Society of Photo-Optical Instrumentation Engineers, p. 84-91, August 1979.

[56] L.N.D. Loo, K. Doi, C.E. Metz, “A comparison of physical image quality indices and observer performance in the radiographic detection of nylon beads”, Physics in Medicine and Biology, Vol. 29, No. 7, pp. 837-856, July 1984.

[57] B. McCleary, “A scalar quantization method for noisy CMOS imager data”, Proc. of the SPIE, Vol. 5208, pp. 153-164, 2004.

[58] B. McCleary, “Color Correction Methods to Reduce Pixel Random Noise for CX20450", Conexant internal memo, Aug. 2000.

[59] B. McCleary, “Cross-talk adjustment in electronic imaging devices”, United States Patent 7170555, Issued Jan. 2007.

[60] B. McCleary, “Cross-talk correction methodology for color CMOS imagers,” Proc. IS&T/SPIE International Symposium on Electronic Imaging, SPIE Vol. 5678, pp. 117-128, Jan. 2005.

[61] B. McCleary, “Methods to Reduce the Amplification of Random Noise in the Color Processing of Imager Data”, IS&T's 2003 PICS Proceedings, pp. 50-57, Jan. 2003.

[62] R. Molina, J. Mateos, A.K. Katsaggelos, M. Vega, “A General Multichannel Image Restoration Method Using Compound Models” IEEE Computer Society, Proceedings of the 16th International Conference on Pattern Recognition, ICPR, Vol. 3, pp. 30835, 2002.

[63] R. Molina, J. Mateos, A.K. Katsaggelos, M. Vega, “Bayesian Multichannel Image Restoration Using Compound Gauss-Markov Random Fields”, IEEE Transactions on Image Processing, Vol. 12, No. 12, Dec 2003.

[64] K. Mullen, “The contrast sensitivity of human color vision to red-green and blue-yellow chromatic gratings,” Journal of Physiology, vol. 359, pp. 381-400, 1985.

[65] B. Natarajan, “Filtering Random Noise from Deterministic Signals via Data Compression”, IEEE Transactions on Signal Proc., 43(11), Nov. 1995.

[66] S. Oraintara, W. C. Karl, D. A. Castañon, T. Q. Nguyen, “A Method for Choosing the Regularization Parameter in Generalized Tikhonov Regularized Linear Inverse Problems”, ICIP 2000.

[67] M.K. Özkan, A.T. Erdem, M.I. Sezan, A.M. Tekalp, "Efficient Multiframe Wiener Restoration of Blurred and Noisy Images Sequencyes," IEEE Transactions on Image Processing, Vol. 1, No. 4, pp. 453-476, Oct 1992.

[68] B. Pain, B. Hancock, “Accurate Estimation of Conversion Gain and Quantum Efficiency in CMOS Imagers,” Proceedings of SPIE-IS&T Electronic Imaging, SPIE vol. 5017, pp. 94-103, 2003.

[69] B. Pain, G. Yang, B. Olson, et al., “A low-power digital camera-on-a-chip implemented in CMOS active pixel approach,” Proceedings of VLSI Design, pp. 26-31, Jan. 1999.

[70] W.B. Pennebaker, and J.L. Mitchell, “JPEG Still Image Data Compression Standard,” Chapman & Hall, New York, 1993.

[71] J. Qi, R.M. Leahy, “A Theoretical Study of the Contrast Recovery and Variance of MAP Reconstructions from PET Data”, IEEE Trans. on Medical Imaging, vol. 189, no. 4, pp. 293-305, April 1999.

[72] M.A. Robertson, and R.L. Stevenson, “DCT Quantization Noise in Compressed Images”, IEEE Trans, Vol. 15, Issue 1, pp 27-38, Jan. 2005.

[73] A. Rose, “The sensitivity performance of the human eye on an absolute scale”, Journal of the Optical Society of America, Vol. 38, pp. 196-208, 1948.

[74] K. Sauer and C. Bouman, “A Local Update Strategy for Iterative Reconstruction from Projections”, IEEE Trans. on Sig. Proc., vol. 41, no. 2, pp. 534-548, Feb. 1993.

[75] O.H. Schade, “On the quality of color-television images and the perception of colour detail,” Journal of the Society of Motion Pictures and Television Engineers, vol. 67, no. 12, pp. 801–819, 1958.

[76] O.H. Schade, “Optical and photoelectric analog of the eye,” Journal of the Optical Society of America, vol. 46, no. 9, pp. 721–739, 1956.

[77] M. Sezan, A. Tekalp, C-T. Chen, “Regularized signal restoration using the theory of convex projections”, Acoustics, Speech, and Signal Processing, IEEE International Conference on ICASSP, Vol. 12, pp. 1565-1568, Apr 1987.

[78] J.H. Shin, J.K Paik, M.G. Kang, "Comparison between Wiener and CLS Image Restoration Techniques for Multichannel Images," Proceedings of IEEE Asia Pacific Conf on Circuits and Systems, pp. 532-535, Nov 1996.

[79] J.W. Stayman., J.A. Fessler, “Regularization for uniform spatial resolution properties in penalized-likelihood image reconstruction”, IEEE Trans Med Imaging.;19(6):601-15., June 2000.

[80] Y.P. Tan and T. Acharya, “A Method for Color Correction with Noise Consideration”, IS&T/SPIE, vol. 3963, pgs. 329-337, Jan. 2000.

[81] A.A. Tanbakuchi, A. van der Sijde, B. Dillen, A. Theuwissen, and W. de Haan, “Adaptive pixel defect correction”, Proc. of SPIE-IS&T, SPIE vol. 5017, 2003

[82] A.N. Tikhonov and V.Y. Arsenin, Solutions of Ill-Posed Problems, chapters 1 & 2, V.H. Winston & Sons, Washington D.C., 1977.

[83] F. Truchetet, B. Joanne, F. Perot, and O. Laligant, “High-Quality Still Color Image Compression”, Optical Engineering/SPIE, Vol. 39(02), pgs.409-414, Feb. 2000.

[84] H.J. Trussel and R.E. Hartwig , “Mathematics for Demosaicking”, IEEE Transactions on Image Processing, Vol 11, No. 4, pgs 485-492, April 2002.

[85] B.A. Wandel and X.M. Zhang, “A spatial extension to CIELAB for digital color image reproduction,” Society for Information Display Symposium Technical Digest, vol. 27, pp. 731-734, 1996.

[86] X.W. Wang, C. Wang, "Regularized Image Restoration Based on Adaptively Selecting Parameter and Operator," Processings of the 17th International Conference on Pattern Recogniton, IEEE, Vol 3, Issue 23-26, pp. 662-665, Aug. 2004.

[87] A.B. Watson, “Visual detection of spatial contrast patterns: Evaluation of five simple models”, Optics Express, Vol. 6, Issue 1, pp. 12-33, Jan. 2000.

[88] A.B. Watson, and A.J.J. Ahumada, “An improved detection model for DCT coefficient quantization”, SPIE Proc. 1913, pp 191-201, 1993.

[89] A.B. Watson, and R. Rosenholtz, “Perceptual adaptive jpeg coding”, Vol. 1, pp. 901-904, 16-19 Sep 1996.

[90] A.B. Watson, J. Hu, and J.F. McGowan, “Digital video quality metric based on human vision”, SPIE, Journal of Electronic Imaging, vol. 10, pp 20-29, Jan 2001.

[91] S. Welstead, “Fractal and Wavelet Image Compression Techniques”, SPIE Press, vol. TT40, pgs. 131-153, Nov. 1999.

[92] T. Zarnowski, T. Vogelsong, and J. Zarnowski, “Inexpensive Image Sensors Challenge CCD Supremacy”, Photonics Spectra, pgs. 188-190, May 2000.

[93] W. Zhu, N. P. Galatsanos and A. K. Katsaggelos, "Regularized Multi-Channel Image Restoration Using Cross-Validation", Proc. SPIE Conf. on Visual Communications and Image Processing, SPIE Vol. 1818, pp. 345-356, Nov. 1992.

Appendix A

CMOS Imager Noise

CMOS image sensors experience noise from numerous noise sources. The resulting aggregate noise has both time-invariant (fixed-pattern) and time-variant (temporal) behavior. The use of the term fixed-pattern noise refers to any spatial pattern that does not change significantly from frame to frame, whereas, the temporal noise changes from frame to frame [42]. A noise transfer diagram is shown in Figure A.1 for a typical CMOS imager [35]. The temporal (time variant) noise that CMOS sensors encounter includes [92]: photon shot noise, capacitive reset (kTC) noise, dark current time-varying noise, Johnson (thermal or white) noise, and 1/f noise (frequency-dependent). Additionally, CMOS imagers can suffer significant temporal noise from electrical ground-bounce and coupling noise problems generated by on-chip logic and ADC circuitry. Fixed pattern noise (FPN) is generated in CMOS imagers by pixel variations in dark current and sensitivity, as well as pixel fixed offset. It is common practice to express the values of the noise sources in root mean square (RMS) electron values.

Photon shot noise is created by the uncertainty due to the quantum nature of light [42]. The measurement process can be considered a Poisson counting process, since the

sensor is in effect counting the arrival of photons. The probability that *n* photons will arrive at a pixel during a time interval T with a photon flux (photon event rate) of *r* is given by the probability mass function:

$$p(n \mid r) = \frac{(r\mathrm{T})^n}{n!}\mathrm{e}^{-r\mathrm{T}} \tag{A.1}$$

If the number of photons detected by the device is large, then the noise can be well modeled by a signal-dependent Gaussian distribution [42]. Since the underlying process is Poisson, the variance of the Gaussian approximation is equal to the mean. This relationship is very useful in the characterization of image sensors. Each pixel can be treated as independent from the others. When photon shot noise is much greater than other sources of noise, then we say that the sensor is shot noise limited [42]. The signal-to-noise ratio (SNR) can be then determined using only photon shot noise. The maximum number of electrons that a pixel can hold is called the full well of the pixel [42]. Sensors that have larger full well will have a larger maximum signal to noise ratio when they are shot noise limited. Smaller pixels have a smaller maximum signal to shot noise ratio [41]. These effects reduce the sensor's dynamic range and SNR for small pixels.

Dark current is signal that is generated by the sensor independent of incoming light signal [42]. Dark current has three main sources of generation. The first is thermal generation in the depletion region of the photodiode. The second is thermal generation and diffusion in the bulk material of the sensor. Lastly, dark current is created by surface states. Dark current can result in both temporal and fixed pattern noise [42]. The temporal dark current is dark current shot noise. If the number of electrons generated by dark current is large, then the dark current temporal noise can be modeled as a dark

current signal-dependent Gaussian distribution. Variation from pixel to pixel in the amount of dark current generation results in pixel-to-pixel fixed pattern noise. The dark current is a function of temperature, roughly doubling for every 8°C increase [42]. It is also directly proportional to the integration time. At higher temperatures and longer exposure times, the dark current fixed pattern noise can become a dominant noise source, limiting the SNR of an image. The fixed pattern dark current, or pixel-to-pixel mean dark current, can be subtracted out from an image frame. However, the temporal component, dark current shot noise, cannot be removed in this simple manner. Scientific imagers can be cooled to significantly reduce dark current. However, commercial consumer imagers usually do not have this option, especially embedded imaging sensors. Thus, due to dark current concerns as well as motion blur, the maximum exposure or integration time for an embedded application sensor is limited, typically to no more than 30 to 60 ms.

One of the dominant sources of temporal noise in CMOS imagers is *pixel reset noise* [92], which occurs when the sense node capacitor of the pixel is reset using the reset transistor. Refer to Figure A.2 for a typical 3T transistor, which has reset, source follower, and row select transistors. This noise is generally uncorrelated from pixel to pixel [40], [42]. The reset field-effect transistor switch generates the *kTC noise*, where k is Boltzmann's constant, T is the temperature, and C is the capacitance of the attached load. The kTC reset noise is due to the thermal noise generated by the resistance within the reset transistor [42]. After the photodiode is reset, the capacitance of the floating diffusion is recharged through the noisy reset transistor. As the size of the pixel photodiode is reduced due to the demands of embedded applications, the capacitance also decreases. This increases the kTC noise, as well as decreasing the full-well signal

level. A passive pixel sensor (PPS) uses a MOS transistor acting as a switch to connect to the column circuitry. This pixel architecture is limited in performance due to the small capacitance of the photodiode connected to the large column circuitry readout capacitance. Adding a small amplifier (source follower) to every pixel results in the active pixel sensor (APS) architecture. Compared to the PPS, the APS reduces the pixel reset noise, as well as fixed pattern noise. The imagers used in this document are all APS CMOS sensors. Reset noise for CMOS imagers usually falls in the range of 20 to 70 noise electrons, depending on the pixel architecture and the sense node sensitivity (V/e-) [40]. The value of the reset noise can be determined from the Johnson noise current variance:

$$\sigma_i^2 = (4kT/R)\,\Delta f\,, \tag{A.2}$$

where Δf is the noise equivalent bandwidth and is given by Δf = RC/4, with C the sense noise capacitance. Then we have:

$$\sigma_i^2 = kTC \tag{A.3}$$

The root mean squared (rms) noise in electrons is then:

$$\sigma_e = \frac{\sqrt{\mathrm{kTC}}}{\mathrm{q}}\,, \tag{A.4}$$

where q is the electronic charge, and Equation (A.4) gives the uncertainty in the amount of charge in the capacitor after it has been reset. When uncorrelated double sampling is used, as with a 3T pixel design, then two uncorrelated pixel resets occur. When these resets are completely independent, which is a good assumption, then the noise variance

will double and the rms noise (standard deviation) will increase by the square root of two (about a 41.4% increase).

There are various definitions of the read noise of a CMOS imager that are used in literature, that have subtle differences. In this thesis, we will take the read noise to be the noise obtained from the reading of the pixel itself. It does not include any of the noise sources down stream of the pixel. It also is completely temporal, not including the fixed pattern noise sources described in this appendix. It also does not include photon shot noise. The read noise is independent of the signal. The pixel read noise will include the pixel reset noise and the temporal noise generated by the pixel's source follower transistor. The pixel's source follower transistor is an amplifier, and will thus have *1/f noise* and the *white noise* [35], [42]. The read noise can be obtained by reading a pixel at very short exposure time in the dark. If possible, the analog data is read which removes the noise associated with the on-chip amplifier, which is discussed next. The read noise is often taken as the noise floor for the image sensor. The dynamic range is then calculated as the ratio of the full well signal divided by the read noise. Some references include the dark current noise and down stream temporal noise in the calculation of dynamic range.

An on-chip amplifier is typically used to gain the signal prior to digitization through the analog-to-digital converter (ADC). It will usually have variable gain that is used to adjust the signal to go from rail-to-rail on the ADC. As the light of an image decreases, the signal data is gained up. The *amplifier noise* consists of two components, the 1/f noise and the white noise [42]. When the on-chip amplifier is designed well, the noise from these sources will be much smaller than the dominant sources, and thus can usually be neglected.

Pixel to pixel sensitivity or *photo response non-uniformity* results in fixed pattern noise [30]. The pixel sensitivity non-uniformity is caused by small variations in the pixels [42]. The photo response non-uniformity is directly proportional to the input signal strength. Thus, this form of noise is multiplicative. This fixed pattern noise is typically expressed as a fraction of the total number of electrons that the pixel contains. Thus, this noise is characterized as a percentage of the signal. Flat fielding correction methods can be used to remove this noise [42]. However, this requires a pixel-by-pixel multiplicative correction that is computationally expensive. Additionally, each pixel can have a fixed offset that will vary across the pixel array. This fixed voltage offset can exist even when correlated double sampling (CDS) is performed. The fixed offset is due to difference between pixels as well as difference between parallel signal processing channels. Specifically, the column buffers or sample and hold capacitors used for each column of the pixel array will have some variation. This can result in column fixed pattern noise (CFPN). The fixed offset can be measured in the dark at close to zero integration time, and then be removed through subtraction. Through careful pixel design and process control these noise sources can be minimized.

The process of converting the pixel signal from the analog domain (voltage or electrons) to a digital number through the analog-to-digital converter (ADC) creates *quantization noise* [35], [42]. An uncertainty is created due to a range of analog inputs being mapped to the same digital output. The mean squared quantization error is the variance (σ_q^2) due to quantizer round-off, and is given by:

$$Q_{MSE} = \sigma_q^2 = E[(v - v')^2] , \qquad \text{(A.5)}$$

where *v* is the image data and *v'* is the quantized image data. The expected error is a function of the probability distribution function (pdf) of the image. The usual assumption is made that the input image probability distribution is uniform, which results in the rms quantization noise in electrons given by:

$$\sigma_q = \frac{k(e^-/DN)}{\sqrt{12}}, \qquad \text{(A.6)}$$

where *k*(e-/DN) is the image conversion gain from electrons to digital output. As the number of bits the ADC uses is increased, the values of *k*(e-/DN) and σ_q decrease. Typically, embedded image sensors use 10-bit ADCs. Usually, the value of σ_q will be less than the noise floor.

System noise is temporal noise that is created by sources related to the operation of the sensor [42],. The on-chip and off-chip electrical circuits can create this noise. The on-chip circuits include the timing logic and analog to digital converters (ADC). These circuits can cause clock coupling and ground bounce noise problems. With the size of the imager dies being reduced, the routing of digital and analog signal lines is very critical. It can be challenging to keep the analog signal process circuitry clean with all of the digital signal process circuitry on the same chip. This contributes to CMOS imagers having difficulty in achieving low-noise performance. Additionally, noise can feed-through into the image sensor from the system that the sensor is integrated. The power supply to the sensor can be corrupted with noise that affects the overall noise performance. Most often, due to the timing constants of the system, the system noise will manifest itself as row temporal noise (RTN). Fortunately, through careful design, the system noise of an imager system can be kept small.

When viewed as an image system, all of the noise sources discussed can be considered uncorrelated from pixel-to-pixel. The noise sources are functions of the input and output signal levels, exposure time, and temperature. A signal/noise model for a CMOS image sensor can be developed using characterization and sensor performance theory. The model will be a function of the sensor operating conditions, namely temperature, exposure time, and input signal level. Signal/noise models are used in Chapters 2 and 3.

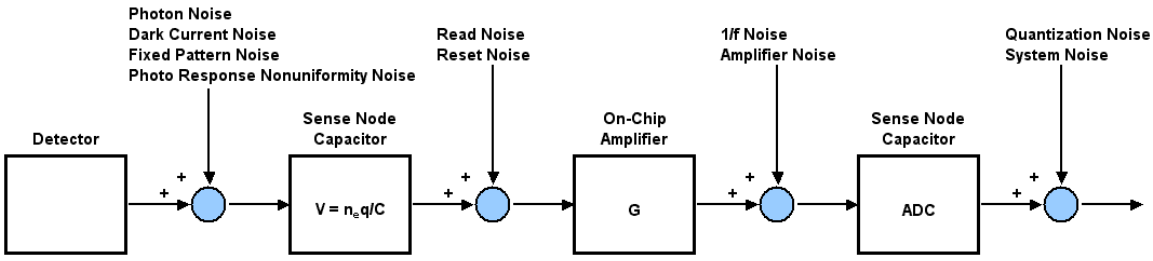

Figure A.1: CMOS imager noise transfer diagram.

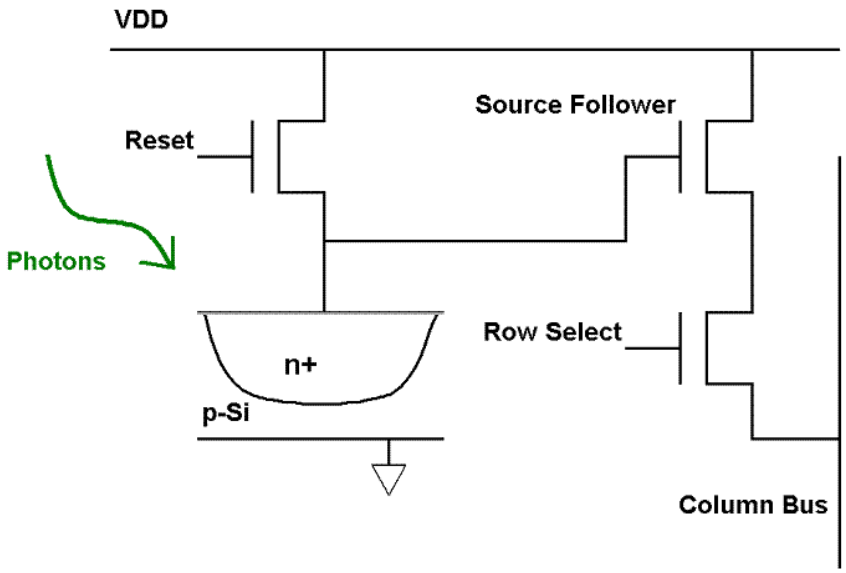

Figure A.2: Three transistor active pixel based on a photodiode element.

Appendix B

Photon Transfer Curve

The conversion gain of an imager is defined as the amount of output generated per unit charge created in the pixel [42]. The number of electrons in the pixel is usually not known. Thus, the conversion gain must be estimated from measurements or indirectly calculated. One method that is used to estimate the conversion gain is the photon transfer method or mean-variance method [68]. The transfer function relating the number of electrons *n* stored in the diode a pixel to the pixel's output in volts *v* can be written as:

$$v = f(n) \tag{B.1}$$

where f() is an unknown and possibly non-linear function that maps input electrons to output voltage. Letting *p* represent the number of photons incident on a pixel, the quantum efficiency (QE) and conversion gain c_g are given by:

$$\eta = n/p \quad \text{(QE)} \tag{B.2}$$

$$c_g(p) = df(n)/dn = f'(n)_{\,n = \eta\, p} \tag{B.3}$$

When an image sensor is linear, the conversion gain is independent of input signal, which can be written as:

$$c_g = f'(n)_{n = \eta p} = f' \tag{B.4}$$

The sensor output signal mean μ_v and variance σ_v^2 can be written as:

$$\mu_v = f' \mu_n + \mu_{Voff} , \tag{B.5}$$

$$\sigma_v^2 = (f')^2 \sigma_n^2 + \sigma_{dwn}^2 , \tag{B.6}$$

where μ_n is the mean number of electrons in the pixel diode, μ_{Voff} is the mean offset voltage of the output (voltage black level), σ_v^2 is the variance of the output voltage, and σ_{dwn}^2 is the variance of the output voltage that is downstream of the diode. Thus, we place all forms of noise besides the photon-arrival noise into the term σ_{dwn}^2. The photon-arrival process is a Poisson process. If the number of photons detected by the device is large, then the signal can be well modeled by a signal-dependent Gaussian distribution. The variance of the electrons in the diode is then equal to the mean:

$$\sigma_n^2 = \mu_n \tag{B.7}$$

Using Equations (B.5) and (B.7), we can write Equation (B.6) as:

$$\sigma_v^2 = f'(f'\mu_n) + \sigma_{dwn}^2 ,$$

$$\sigma_v^2 = f'(\mu_v - \mu_{Voff}) + \sigma_{dwn}^2 \tag{B.8}$$

Then from Equation (B.8) we can write:

$$c_g = f' = d(\sigma_v^2)/d(\mu_v) \tag{B.9}$$

The conversion gain given by Equation (B.9) can be obtained from measured data. We can generate a similar conversion gain from electrons to digital counts output, c_{gDN}, or *k*(e-/DN), using the same logic with the sensor output specified in digital counts. This can be much more convenient since most CMOS imagers have on chip ADCs. The digital conversion gain can be determined for all of the operational internal gain settings of the sensor. The digital conversion gain is usually written as mapping from output DN to input electrons [68]:

$$k(e\text{-}/DN) = d(\mu_{DN})/d(\sigma_{DN}^2) \qquad \text{(B.10)}$$

A problem with Equation (B.10) is that it assumes the transfer function to be linear. However, for a CMOS imager, there can be non-linearity. The capacitance of a p-n junction diode is dependent on the reverse-bias applied to it. The non-linearity effect of the photo diode capacitance increasing as the signal level increases causes the noise sensitivity (V/e-) to decrease and the digital conversion gain (e-/DN) to increase. For example, there can be a 15% to 20% change for a 1v change in reverse-bias. The source-follower transistor can also behave non-linearly. However, methods have been developed to correct for this error [41], [68]. In [68], the slope of the photon transfer function is modeled as being linearly related to the conversion gain. In [41], the photodiode gain variation is corrected by assuming that the node capacitance change is linear with signal. These two corrections are essentially the same, and produce accurate results.

A complete noise performance of an imaging sensor can then be determined using the photon transfer technique [41]. The read noise in DN can be converted to electrons by using the low signal conversion gain, k_{RN}(e-/DN). The full well in DN can be converted to

electrons using the high signal conversion gain k_{FW}(e-/DN). Linearity, signal to noise ratio, dynamic range, and sensitivity can also be determined using the photon transfer technique. The full well signal is determined from the photon transfer plot by noting the signal at which the noise suddenly decreases, which signifies a loss of modulation of the signal. At full well, signal is lost to adjacent pixels. It is convenient to plot the photon transfer data on a log-log scale, since due to the Poisson probability distribution of arriving photons, the signal (mean) versus shot noise (standard deviation) will yield a slope of one-half. A photon transfer curve of an imager that was used to generate SNR models is shown in Figure B.1 [17]. We use the photon transfer method to help develop the pixel noise models used in Chapters 2 and 3. A sensor's photon transfer curve is used in Section 2.3.2 to show the separate pixel response noise regions.

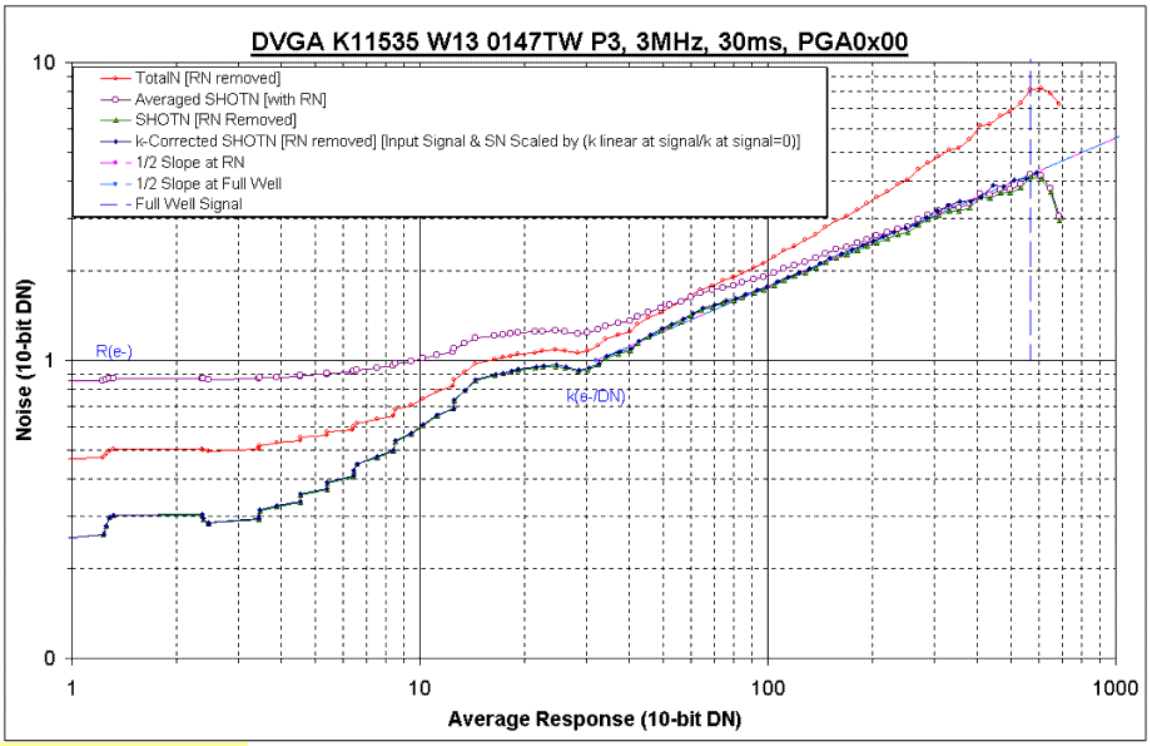

Figure B.1: Photon transfer curve for CMOS sensor. K(e-/DN) is 31 at dark level and 36 at saturation level. Read noise is 25 e-, total noise in dark is 28 e-, full well is 21,000 e- [17].

Appendix C

Examination of Existing Bayer Cross-Talk Correction Methods

Cross-talk is the loss of electrons or photons from a pixel to neighboring pixels. Pixel cross-talk degrades both image sharpness (modulation transfer function, MTF) and colorimetric accuracy (highly de-saturated, color-muted images). There exist many restoration methods that can be applied to the Bayer cross-talk problem. However, due to their complexity, many of these methods cannot be implemented into simple low cost camera systems. We present in this appendix some of the more important and useful restoration methods.

C.1 Multi-Channel Methods that Optimize Color Channel Regularization

The more complex multi-color channel restoration methods allow for the optimization of the regularization parameter for each color channel separately. These restoration methods typically employ an iterative solution. In [27], two methods for determining the regularization parameter are developed, which serve as the foundation for many other methods: a set theoretic (ST) approach and a constrained least squares (CLS) optimization. Both of these methods solve the multiple channel regularization equation:

$$[\, \boldsymbol{H}^T \boldsymbol{\Lambda} \boldsymbol{H} + \boldsymbol{Q}^T \boldsymbol{Q} \,]\, \hat{\boldsymbol{f}} = \boldsymbol{\Lambda} \boldsymbol{H}^T \boldsymbol{y} \,, \tag{C.1}$$

where $\boldsymbol{\Lambda}$ is a matrix of N color channel regularization parameters (λ_i), and is written in the form:

$$\boldsymbol{\Lambda} = \begin{bmatrix} \lambda_1 [I] & 0 & 0 & 0 \\ 0 & \lambda_2 [I] & 0 & 0 \\ 0 & 0 & \lambda_3 [I] & 0 \\ 0 & 0 & 0 & \lambda_4 [I] \end{bmatrix}, \tag{C.2}$$

and where [I] is an identity matrix of size $M^2 \times M^2$. The regularization operator, **Q**, used in [27] has both 2-D Laplacian (within channel smoothing) and 3-D Laplacian (across channel smoothing) components. Using a Laplacian smoothing prior simplifies the problem since it results in a quadratic regularization operator (system of linear equations) [48]. The objective is to determine the optimal regularization parameters (λ_i) of the diagonal matrix $\boldsymbol{\Lambda}$. The ST approach restricts the solution of **f** to lie within a set S_f. The noise of each color channel, $\mathbf{n}_i$, also lies within the sets S_{ni}. The observation of a color channel $\mathbf{y}_i$ specifies a set $S_{f/yi}$, which contains **f**. Since each of the sets S_f, $S_{f/y1}$, … $S_{f/yN}$, contain **f**, **f** must lie in the intersection of these sets. The solution $\hat{\mathbf{f}}$ is then taken to be within the intersection of sets defined for each channel's solution:

$$\boldsymbol{f} \in S_{F/Yi} = [\, \boldsymbol{f}: (\boldsymbol{H}_i \boldsymbol{f} - \boldsymbol{y}_i) \in S_{ni} \,] \tag{C.3}$$

When ellipsoids are used for the sets S_f and S_{ni}, we have:

$$\| \boldsymbol{n}_i \|^2 = \| \boldsymbol{H}_i \boldsymbol{f} - \boldsymbol{y}_i \|^2 \le e_i^2 \text{ and } \| \boldsymbol{Q}_i \boldsymbol{f} \|^2 \le E_i^2 \text{ for } i=1,2, \ldots, N \,, \tag{C.4}$$

Where, e_i^2 is proportional to the noise variance in color channel *i*, and E_i^2 is a smoothness constraint for color channel *i*, where $\mathbf{H}_i$ and $\mathbf{Q}_i$ are the *i*th channel M^2xNM^2 matrices $\mathbf{H}_i=[\mathbf{H}_{1i}, \mathbf{H}_{2i}, \ldots \mathbf{H}_{Ni}]$ and $\mathbf{Q}_i=[\mathbf{Q}_{1i}, \mathbf{Q}_{2i}, \ldots \mathbf{Q}_{Ni}]$ for color channel *i*. Thus, $\mathbf{H}_i$ and $\mathbf{Q}_i$ are composed of block circulant sub-matrices. The smoothness constraint imposes a requirement that the high-frequency energy of the de-convolved image is bounded by the values E_i for each channel. The assumption of equal smoothness of channels is used, giving $E = E_i$ for i=1 to N. A solution that is at the center of the ellipsoid that bounds the intersection of the ellipsoids gives us the values of the regularization parameters as:

$$\lambda_i = (E/e_i)^2 \qquad \text{(C.5)}$$

This method requires an estimate of each color channel's additive noise, e_i, as well as an estimate of the full original image, **f**. An accurate estimate of **f** is required to determine the smoothness constraint or high-energy bounds of the de-convolved image, E_i, for the channels of **f**. The requirement for an accurate estimate of E_i can be overly restrictive [44]. Iterative methods can be used to determine accurate estimates for the regularization parameters of Equation (C.5) [48]. It is seen from the solution of this method that the within color channel smoothing, $\mathbf{Q}_{ii}$, and the across color channel smoothing, $\mathbf{Q}_{ji}$, $j \neq i$, is controlled by the same smoothness bounding limit E_i. This restriction can result in a sub-optimal result, since the correlation between the color channels will vary spatially within an image. Additionally, it is noted that this solution does not consider the interaction of the channels in determining the optimal regularization values λ_i for each channel. Each λ_i term is optimized using only its channel noise and maximum energy estimations, but each corrected channel will be a

function of all the observed channels and all of the regularization parameters ($\hat{\mathbf{f}}_i$=Func{$\mathbf{y}$, $\mathbf{H}$, $\mathbf{Q}$, $\lambda_{i=1,4}$}). Similarly, in [44], multi-channel restoration is performed using a convex smoothing functional. It has the obstacle that its iterative solution has high computational cost.

A Constrained Least Squares (CLS) optimization approach is used in [27] when the smoothness constraint value E is not known *a priori* or a satisfactory estimate is not available. For this method, we seek a solution $\hat{\mathbf{f}}$ which:

$$\text{minimizes:} \quad \| \boldsymbol{Qf} \|^2$$

$$\text{subject to:} \quad \| \boldsymbol{H_i f} - \boldsymbol{y}_i \|^2 = \| \boldsymbol{n}_i \|^2 = e_i^2 \text{ , for } i=1,2, \ldots, N \text{ ,} \qquad \text{(C.6)}$$

where $\mathbf{H}_i$ is the i^{th} channel $M^2 \times NM^2$ matrix $\mathbf{H}_i=[\mathbf{H}_{1i}, \mathbf{H}_{2i}, \ldots \mathbf{H}_{Ni}]$ and $\mathbf{n}_i$ is the noise of color channel i. The solution of the regularization Equation (C.1) subject to these constraints, Equation (C.6), requires that we must simultaneously find the values of λ_i, which can be written as:

$$Z_i(\lambda_1, \lambda_2, \ldots \lambda_N) = (\| \boldsymbol{H}_i \hat{\boldsymbol{f}} - \boldsymbol{y}_i \|^2 = \| \boldsymbol{n}_i \|^2) \text{ for } i=1,2, \ldots, N \qquad \text{(C.7)}$$

This leads to a nonlinear problem, which has a very high computational cost, since the roots of the nonlinear functions $Z_i(\lambda_1, \lambda_2, \ldots \lambda_N)$ must be found simultaneously to give the desired λ_i values. Typically, it is solved using an iterative method, such as Newton iterations, to find the matrix of λ_i values (matrix $\boldsymbol{\Lambda}$). Newton's method involves calculating the Jacobian of the system (Z_i), which has the ij^{th} element found from [27]:

$$\boldsymbol{J}_{ij} = \partial(\| \boldsymbol{H}_i \hat{\boldsymbol{f}} - \boldsymbol{y}_i \|^2)/\partial(\lambda_j)^{-2} = -2(\boldsymbol{H}_i \hat{\boldsymbol{f}} - \boldsymbol{y}_i)^T \boldsymbol{H}_i \boldsymbol{A}^{-1} \boldsymbol{I}_{ji} \boldsymbol{Q}^T \boldsymbol{Q} \hat{\boldsymbol{f}} \text{ , where} \qquad \text{(C.8)}$$

$$\boldsymbol{A} = [\boldsymbol{H}^T\boldsymbol{H} + \boldsymbol{\Lambda}^{-1}\boldsymbol{Q}^T\boldsymbol{Q}] \quad \text{(C.9)}$$

As with the ST method, the amount of within color channel smoothing, $\mathbf{Q}_{ii}$, and across color channel smoothing, $\mathbf{Q}_{ji}$, $j \neq i$, applied are controlled by the same regularization parameter, λ_i. The color channel smoothing matrices, $\mathbf{Q}_{ji}$, have their coefficients scaled by the relative signal strengths, $\| \mathbf{f}_i \|$. But, this does not take into account the local or global difference of values of the noise terms (e_i) of the within and cross color channel components (CCC). See Section 3.2.2.1 for a definition of CCCs. Thus, the correction of color channel *i* will be performed using λ_i which is applied to data from all of the color channels, which will have different ratios of signal and noise strengths. Both of the methods in [27] use global fixed noise variance values.

For both the ST and the CLS methods, the magnitude of the coefficients of the **Q** matrix must be determined. As has been stated, the $\| \mathbf{Qf} \|$ operator is a regularizing functional. The matrix **Q** must leave large singular values of matrix **H** unchanged, while moving small singular values away from zero and not creating any new small singular values in the solution of Equation (C.1) [27]. The matrix **Q** also integrates *a priori* knowledge of the smoothness of **f** in the restoration process. Thus, another constraint of the ST and the CLS methods is the *a priori* knowledge of the smoothness of **f** in determining the $\mathbf{Q}_{ji}$ matrices for the multi-channel problem. As has been mentioned earlier, we will use Laplacian forms of the $\mathbf{Q}_{ji}$ matrices. It has been shown that the Laplacian is a good regularization operator for images that are highly correlated and have low-pass characteristics [26]. In most cases, the Laplacian will be a good choice for the regularization operator. The optimal relative magnitudes of the coefficients of the

$\mathbf{Q}_{ji}$ matrices require additional estimations and calculations, increasing the complexities of these solutions.

Other multi-channel methods include [62], which is a multi-channel MAP method that is iterative and uses a compound Gauss Markov random field, where the noise is Gaussian with fixed variance per channel. In [44], a multi-channel restoration iterative method using convex smoothing functional solution is developed which does not assume *a priori* values of the image smoothness or noise bounds. This method is based upon the work of [27]. The iterative solution has a very computationally expensive cost. An iterative, multi-channel method that works for different noise types but does not use noise model information, and uses least mean squares and least mean fourth order combined smoothing functional is developed in [36]. A high complexity multi-channel Kalman filtering method that uses cross-channel correlations is developed in [25], which can work with stationary and non-stationary (spatial variations) models. An iterative Bayesian approach using Compound Gauss-Markov random fields is used in [63], which performs well at a high computational cost.

The multi-color channel methods shown in this section use a noise model, but it does not vary with the signal magnitude. Also, these methods usually employ an iterative solution, which limits it ability to be implemented in a system. Another key factor that these existing multi-channel methods do not address is the different degrees of ill-conditioning of the individual blurring filters corrupting each color channel. These methods allow for the optimization of the regularization parameter for each color channel separately, but not for each individual color channel components (CCC) of each color. Thus, these methods use one regularization value per color channel, without considering

the individual within and cross CCCs that comprise each color channel. Therefore, these multi-color channel methods are considered too complex for our target application and do not possess all of the features (e.g., individual CCC correction) that we require.

C.2 Signal Dependent Noise Model, Non-Direct Methods

There are restoration methods that account for signal dependent (non-uniform) noise, but these methods are typically complex and non-direct. These methods are thus too complex to use in our targeted low-cost camera system. The methods referenced here are for a single channel, but could be extended to the multi-channel case. Iterative methods that are used to correct a blurred image include the MAP method of [47], which accommodates signal-dependent noise, is spatially adaptive, but is too complex for our application since it is an iterative solution. The iterative MAP filter [55] considers signal-dependent Poisson noise, uses a nonstationary mean and stationary variance model along with local image statistics. A signal-dependent noise MAP method is presented in [37] which is solved using an iterative solution. In [50], a signal-dependent noise method using nonstationary local mean and variance estimations is developed that utilizes recursive Kalman prediction and filtering. A signal-dependent noise, LLMSE, direct method is developed in [49] that uses nonstationary estimates from local data and is adaptive to local data, but is applicable to non-blurring cases only. Gauss-Seidel iterations are used in the ML and MAP methods of [74], which use a signal-dependent Poisson model with local updates. In [24], an iterative P-LH (penalized likelihood) uniform resolution (modified penalty) method using a Poisson model, LIR (local impulse response), local blurring, and local data is developed. A PWLS (penalized weighted least squares) method that uses a variance matrix based on Gaussian estimations (1/y being approximately Poisson) is created [23], where an iterative solution must be used to

determine the estimations. An iterative P-LH method for uniform spatial resolution using a Poisson model and locally applied is constructed in [79]. The method of [2] uses a PWLS approach with a Poisson model (1/y ~ Poisson approximation), that is iterative due to the use of noise estimations. An iterative, P-ML technique using a Poisson model, optimal FIM (Fischer Information Matrix) estimation and uniform resolution is derived in [53].

Some methods use simplified noise models or local estimates, but still require iterative solutions. A regularized, iterative method that adapts locally using estimates of local (locally fixed) noise variances (does not use an *a prior* noise model) is present in [86]. The method uses adaptive regularization parameter and operator to control the amount of noise smoothing within the image. The method, which is too complex for use in our targeted camera model, has an operator based on edge or no edge local data. A bounded noise variance (fixed) method using convex projections is developed in the iterative solution of [77]. The regularization MAP method of [46] uses fixed Gaussian noise variance and the image spectrum. A cross-validation estimation of a fixed i.i.d. noise variance is used in [93]. An iterative regularization with a noise fixed variance is utilized in [66]. In [48], a regularized, iterative method that uses projection onto convex sets is developed what uses signal and noise covariances. Spatially adaptive methods can be used to incorporate non-uniform noise characteristics, however these methods are iterative. The iterative method of [48] is spatially adaptive using a set theoretic restoration algorithm.

C.3 Stochastic Methods

Stochastic regularization methods usually require prior knowledge of the statistics of the image data, which is then used to regularize the restoration problem. A linear estimation of the problem can lead to the classical Wiener filter [3]. In general, it is easier to implement a CLS filter than a Wiener filter, since the CLS filter only requires a simple constraint instead of power spectrum estimations. It is also easier to extend a CLS filter to a spatially adaptive form due to its deterministic approach [78]. Additionally, the performance of stochastic restoration methods is very sensitive to accuracy of estimations or calculation of the image and noise statistics [93]. A multi-channel Wiener filtering algorithm that uses within and cross-channel power spectra is presented in [67], which is too complex for our camera system.

Stochastic methods often require that the covariance of the original image and noise data be estimated over the entire image, which can be expensive for large images. Methods also have been developed where these statistics are calculated over a local area [49]. Stochastic methods do not use deterministic a priori information, such as the common smoothing or high-frequency constraint. We will be using a smoothness constraint that allows for the smoothing (reduction) of noise as a function of local pixel SNR. Taking advantage of the HVS's sensitivity to low frequency color error [64], [75], [76], [85], we can use estimates of the local mean values of SNR to determine our optimal regularization parameters.

Stochastic methods are sensitive to the cross-channel signal correlations, which will vary for each image and for different areas within an image. This information is expensive to calculate, and errors in the values used can lead to poor performance. A Stochastic

method using LMMSE filters (multi-channel Wiener) is developed in [28], where within and cross-channel correlations are used. The solution is very sensitive to these channel correlation statistics [93], and requires $N^2M^2\log_2 M$ operations, which is too complex for our situation. Many stochastic methods use static values of signal and noise variances in order to simplify the solution. A regularization method based on fixed noise and signal variances is developed in [45].

C.4 Methods Using MSE to Determine the Regularization Parameters

For the deterministic regularization approach, the regularization parameter determines the trade-off between fidelity to the data and smoothness of the solution. In [26], the optimal MSE regularization parameter (λ_{mse}) is determined from the value that produces the lowest total objective MSE. This MSE is defined as the sum of the variance of the noise (which is scaled by the restoration method) and the bias error of the estimate. As λ_{mse} increases, the bias error increases, but the noise variance error (due to the ill-conditioned blurring filer) decreases. Our method also uses this approach, however we take it further by looking at the local pixel SNR value. This SNR value is defined as the corrected pixel value divided by the pixel estimate MSE.

As stated in this thesis, the use of the local SNR is justified by the HVS's sensitivity to local signal to noise contrast (SNR) [7], [19] , [56], [73] and to low frequency color errors [64], [75], [76], [85]. Thus, we use the constraint of a maximum local corrected SNR value to determine our regularization parameters (for each CCC). Many other methods exist for determining the value of the regularization parameter to use, such as constrained least squares (CLS) methods using noise bounds [3], [26], set theoretic (ST) methods using image high-frequency and noise bounding ellipsoids [26], [48], predicted

mean square error [26], and maximum likelihood (ML). However, these methods do not satisfy our stated HVS criteria, and often are not direct methods. Additionally, they require that the high-frequency energy bound for the de-convolved image is known *a priori* or that it be calculated through an iterative process. Using local pixel SNR estimation does not impose these requirements.

C.5 Simple Direct Solutions

There are several simple and direct solutions to the Bayer cross-talk blurring problem, but they use assumptions that limit their performance. These methods can be implemented in low-cost camera systems, but will not produce the color quality, noise suppression performance, or image sharpness of more complex methods. A simple computational method with a direction solution is presented in [84] which assumes equal and independent channel blur. Thus cross-channel blurring, typically the greatest contributor to color de-saturation (dulling of colors), is not corrected. The method also assumes fixed noise variance. The multi-channel least squares method of [29] also does not correct cross-channel blurring. In [54], a simple direct prediction filtering method is presented which does not use a noise model (assumes stationary, fixed, known noise variance) or correct the cross-channel blurring. The method's main purpose is to remove the mismatch in green odd/even pixels, which results from the commonly occurring asymmetrical Bayer cross-talk. This mismatch appears as an annoying and highly visible fixed-pattern in images. It can be removed by using the ideal inverse cross-talk filtering (at the cost of noise amplification). A LLMSE (local linear mean square error) method that considers signal-dependent noise and uses non-stationary estimates from local data (adaptive to local data) is presented in [49]. This method does not handle the situation of blurring however, and would not correct cross-

talk. We have previously developed a simple, direct, heuristic method [59], but it is non-adaptive both locally and globally.

A typical simple approach used in industry to correct the signal error due to cross-talk uses a 3-by-3 color matrix correction. This correction essentially performs a LMMSE color correction. The loss of image sharpness is normally corrected in a separate step, which typically is concerned with edge sharpness and not inverse filtering. An optimal 3x3 color correction matrix can be determined using linear regression [43] or calculated from sensor and lighting parameters. The 3x3 color correction matrix $\mathbf{T_{CC}}$ can be broken down into a 3x3 saturation matrix $\mathbf{T_{Sat}}$ and a 3x3 white balance matrix $\mathbf{T_{WB}}$ that only has terms on its main diagonal, as shown below:

$$\boldsymbol{T_{Sat}}\ \boldsymbol{T_{WB}} = \boldsymbol{T_{CC}},$$

$$\begin{vmatrix} T_{Sat11} & T_{Sat12} & T_{Sat13} \\ T_{Sat21} & T_{Sat22} & T_{Sat23} \\ T_{Sat31} & T_{Sat32} & T_{Sat33} \end{vmatrix} \begin{vmatrix} T_{WB1} & 0 & 0 \\ 0 & T_{WB2} & 0 \\ 0 & 0 & T_{WB3} \end{vmatrix} = \begin{vmatrix} T_{CC11} & T_{CC12} & T_{CC13} \\ T_{CC21} & T_{CC22} & T_{CC23} \\ T_{CC31} & T_{CC32} & T_{CC33} \end{vmatrix} \qquad \text{(C.10)}$$

Using this approach, the white balance matrix corrects for the ambient lighting conditions (dynamic, scene dependent), and the $\mathbf{T_{Sat}}$ matrix coefficients correct for the sensor dependent responses. These sensor dependent responses include cross-talk, as well as the responsivity of silicon and the transmissivity of the color filter array (CFA) used. These corrections allow for the mapping from the device dependent color space to the CIE color space. This is shown in Figure C.1, which illustrates the processing path of the camera system.

In order to maintain the white balance of an image, the $\mathbf{T_{Sat}}$ matrix must have the coefficients of each of its rows sum to one. Thus, as the magnitude of the off-diagonal

saturation terms increase, the on-diagonal terms of $\mathbf{T}_{Sat}$ must also increase. This means that for sensors that have more cross-talk, the $\mathbf{T}_{Sat}$ coefficients will have larger values, and the SNR of the processed images will decrease, due to amplification of the noise.

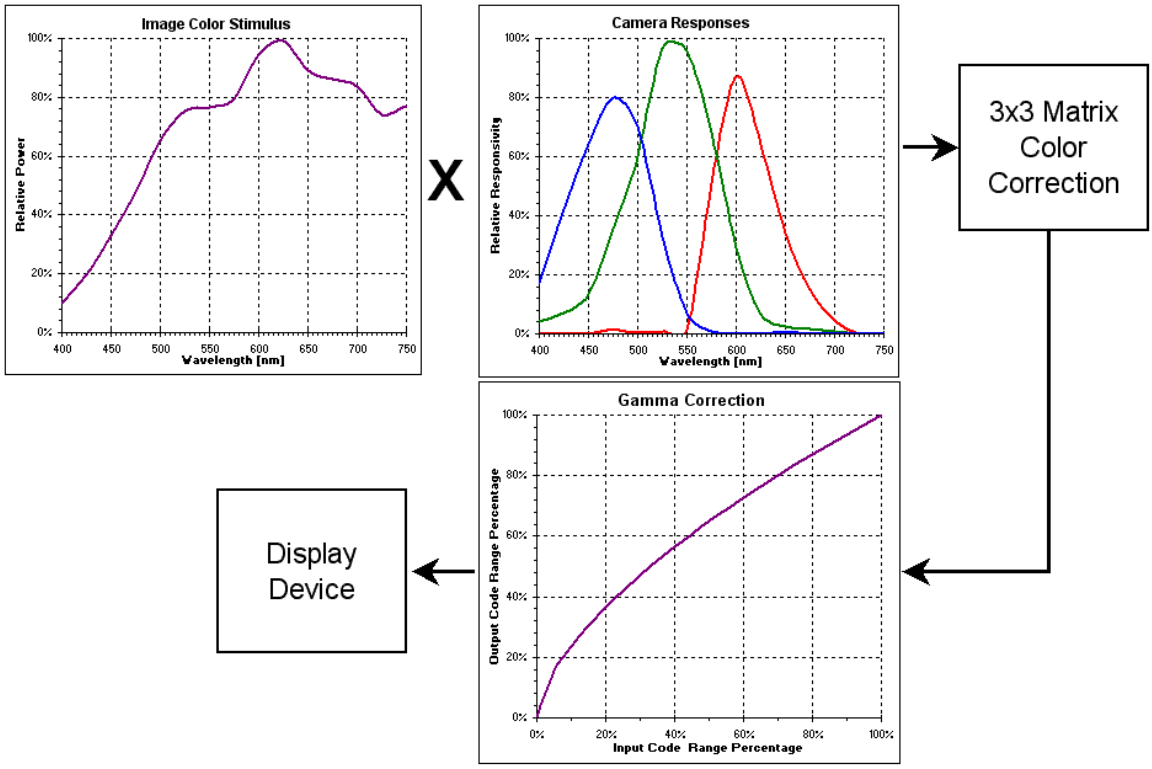

Figure C.1: Typical low-cost camera color correction processing path.

The calculations of the ideal correction coefficients for a 3x3 $\mathbf{T}_{Sat}$ matrix are shown in Figure C.2. The cross-talk coefficients for a DVGA CMOS sensor are used, where the pixel area applied has been restricted to 3x3 pixels (as is done for simple 3x3 color corrections). In the signal diffusion table of the figure, the amount of charge that enters a target pixel (center pixel) and ends up at the specified pixel location is shown. This is the characterized cross-talk behavior.

DVGA CMOS sensor Cross-talk coefs, 3x3 area used, amount of charge that entered target pixel (center pixel) that ends up at the specified pixel location

Blue	Green Even
Green Odd	Red

Amount of Signal Diffused to Neighbor Pixels

Wave Length								
Blue Pixel			Green Pixel			Red Pixel		
0.025	0.023	0.015	0.030	0.032	0.022	0.045	0.055	0.036
0.046	0.810	0.020	0.054	0.743	0.031	0.073	0.607	0.046
0.024	0.022	0.015	0.031	0.034	0.023	0.046	0.056	0.036

Mean Transfer from Pixel to Pixel

To \ From	Blue	Green Odd	Green Even	Red
Blue	0.810	0.066	0.085	0.163
Green Odd	0.045	0.743	0.106	0.119
Green Even	0.066	0.106	0.743	0.111
Red	0.079	0.085	0.066	0.607

Inverse Matrix

Inverse of Mean Transfer from Pixel to Pixel

In \ Out	Blue	Green Odd	Green Even	Red
Blue	1.277	-0.062	-0.110	-0.311
Green Odd	-0.041	1.401	-0.175	-0.232
Green Even	-0.085	-0.169	1.397	-0.200
Red	-0.151	-0.170	-0.113	1.742

Reduce to 3x3

In \ Out	Blue	Green	Red
Blue	1.277	-0.086	-0.311
Green	-0.063	1.227	-0.216
Red	-0.151	-0.141	1.742

Mean blurred transfer of signal from one pixel type to neighboring pixel type.

Inverse matrix operation corrects mean blurring

Reduction from 4x4 to 3x3 correction causes further blurring (averaging), thus ideal correction is not possible.

Figure C.2: Calculations of the color correction matrix for a typical low-cost camera sensor.

There are several sources of error from using this approach. The mean blurred transfer of signal from one pixel type to neighboring pixel type is used in constructing a 4x4 cross-talk transfer matrix. This forces the averaging of cross-talk that occurs in different directions. For example, a blue pixel has four neighboring red pixels, each of which has a particular cross-talk value. But the sample cross-talk value will end up being used for all of its red pixel neighbors. The inverse matrix operation will create a mean blurring correction matrix. Another error is that in order to simplify the camera correction process, the difference in green even and green odd pixel responsivity is not taken into account. The correction matrix is reduced from a 4x4 matrix to a 3x3 matrix, which

introduces a bias error. The 3x3 correction matrix allows the correction to be applied to a Bayer interpolated pixel triplet (RGB values at pixel location). Thus, an ideal correction is not possible with this method. By treating the green even and odd pixels the same, a bias error is created since neither pixel type is corrected using the proper coefficients. This error increases as the asymmetrical behavior of cross-talk increases. Often, simple smoothing or median filtering is used to correct this fixed pattern error [54]. But these methods do not correctly restore the non-blurred image values.

It is also noted that this method has no regularization in place, and cannot account for different noise levels. A common industry approach is to adjust the ideal 3x3 $\mathbf{T_{CC}}$ matrix to approach the $\mathbf{T_{WB}}$ matrix as the overall camera system noise increases (or the SNR decreases). Thus, the coefficients of the saturation matrix are reduced in magnitude when higher camera system gains are used (indicative of lower lighting levels and lower SNR). The adjustment is very rough and global (no local effects considered). By using this adaptive 3x3 matrix approach, the performance at the low quality operating conditions (low light, low SNR) is improved. As mentioned, the control for this adjustment is usually tied to camera exposure time, sensor analog gain, and required digital gain. This idea is shown in Figure C.3 for the same camera system as defined in Figure C.2.

3x3 Correction Matrix, $\mathbf{T_{CC}}$

	Blue	Green	Red
Blue	1.277	-0.086	-0.311
Green	-0.063	1.227	-0.216
Red	-0.151	-0.141	1.742

Decreasing SNR, Increasing Camera Gain →

3x3 White Balance Matrix, $\mathbf{T_{WB}}$

	Blue	Green	Red
Blue	0.970	0.000	0.000
Green	0.000	1.002	0.000
Red	0.000	0.000	1.343

Figure C.3: Typical low-cost camera color correction matrix adjustment.